Time Reversal Invariance -
a Test in Free Neutron Decay

by

Laura Jean Lising

B.S. (University of Virginia) 1992
M.A. (University of California, Berkeley) 1994

A dissertation submitted in partial satisfaction of the
requirements for the degree of
Doctor of Philosophy

in

Physics

in the

GRADUATE DIVISION
of the
UNIVERSITY of CALIFORNIA at BERKELEY

Committee in charge:

Professor Stuart J. Freedman, Chair
Professor Eugene D. Commins
Professor Stanley G. Prussin

1999

Time Reversal Invariance -
a Test in Free Neutron Decay

Laura Jean Lising

Abstract

Time Reversal Invariance -
a Test in Free Neutron Decay

by

Laura Jean Lising
Doctor of Philosophy in Physics

University of California at Berkeley

Professor Stuart J. Freedman, Chair

Time reversal invariance violation plays only a small role in the Standard Model, and the existence of a T-violating effect above the predicted level would be an indication of new physics. A sensitive probe of this symmetry in the weak interaction is the measurement of the T-violating "D"-correlation in the decay of free neutrons. The triple-correlation $D\hat{\sigma}_n \cdot \mathbf{p}_e \times \mathbf{p}_\nu$ involves three kinematic variables, the neutron spin, electron momentum, and neutrino (or proton) momentum, and changes sign under time reversal. This experiment detects the decay products of a polarized cold neutron beam with an octagonal array of scintillation and solid-state detectors. Data from first run at NIST's Cold Neutron Research Facility give a D-coefficient of $-0.1 \pm 1.3(\text{stat.}) \pm 0.7(\text{syst}) \times 10^{-3}$. This measurement has the greatest bearing on extensions to the Standard model that incorprate leptoquarks, although exotic fermion and left-right symmetric models also allow a D as large as the present limit.

Professor Stuart J. Freedman
Dissertation Committee Chair

To my parents, who taught me to believe that all possibilities were open to me.

Contents

List of Figures

List of Tables

Acknowledgements

I am grateful to a large and varied group of people for their help with this experiment and my career in general. I cannot thank them all individually in a length less than the work to follow (although I will make an attempt), so I offer a huge thank you to everyone. This thank you should supplement the gratitude I hope I have expressed to you along the way.

Firstly, I would like to thank everyone involved in this experiment. To the NIST crowd, Jeff Nico, Alan Thompson, Fred Wietfeldt, Gordon Jones, Jim Adams, Scott Dewey, and David Gilliam, thanks for being such a great team to work with - a team built on humor, patience, mutual respect, and friendship. And our team could also play football (or some approximation thereof), take turns at the controls of the crane, and fight without tiring in the battle of the sparks. To Jeff, the guardian of emiT sanity, I thank you for countless things, including my swiss army knife. I know that, now that I have that, this dissertation is just a formality. However, I do wish you would become a vegetarian and just make friends with the possums. They are your fellow earth inhabitants. Alan, thank you for going through DAQ torture with me (you were the ideal partner in that endeavor), and for exercising restraint with the hex rod. Gordon, thanks for the tomatoes and pesto, and for the many hours we spent mentally disentangeling systematics. And thanks, Fred, for keeping our operation ship-shape.

Thanks go to the UW group: John Wilkerson, Hamish Robertson, Tom Steiger, Steve Elliot, Pieter Mumm, Allen Myers, and Mike Browne. Thank you for leading us, John - it was a privilege to work with you. And thanks, Tom, for being our group scapegoat and for never letting us down when the situation called for your unique commentary. To Pieter, my successor, I wish you luck and patience. I am glad you are going to do this and I trust you with the beta detectors - how's that for a compliment? (Stay away from them, Tom.) Thanks also to the Ann Arbor group: Tim Chupp, Kevin Coulter, and Shenq-Rong Hwang. Thanks for your hospitality, Tim. And, Kevin, I am so glad we shared the same emiT language. That helped a lot. I must also send my gratitude to Alejandro García at Notre Dame, and to Geoff Greene, Tom Bowles, Bill Teasdale, and Mel Anaya at Los Alamos. Bill, your design expertise was absolutely key to the success (as well as the beauty) of this experiment. And, finally, I would like to thank the Berkeley team: Brian Fujikawa, Eric Wasserman, and, of course, Stuart Freedman. Thank you, Stuart, for giving me the opportunity to work with you and be part of this experiment. And thank you so much for

helping me to make this work reasonably readable. Have fun in Hawaii in 2001.

I would also like to thank my qualifying committee members, Eugene Commins, John David Jackson, and Stanley Prussin for their help and guidance. Thank you, Dr. Commins, for your patience in so many helpful discussions, and for being the kind of professor who with each lecture renews his students' joy and gratitude for the opportunity to be physicists. Dr. Prussin, I thank you most for your warmth. It both calms and inspires me.

To Lou Bloomfield at the University of Virginia, my continuing gratitude for being such a wonderful role model for me. You inspired me as a teacher, allowed my to do my first real physics research in your laboratory, and continue to help me navigate this path I have chosen to follow. I treasure your friendship. I also want to thank Mel Gomez of the University of Maryland for a fun summer in the magnetic remanance lab and for your continued encouragement. I am also extremely grateful for the friendship and support of Anne Takizawa and Donna Sakima, whose warm smiles and generous assistance ease the stress and lighten the days of those around them.

To the very special people in my life, Dad and Rene, Mom, Janet, Kara, and Jeremy, thank you for believing in me, getting me through tough spots, listening to me complain or burst of enthusiasm, and just being part of my life. I love you all.

This research was supported in part by the Department of Energy. I would like to acknowledge the generous fellowship support from the National Physical Science Consortium and the National Security Agency.

Chapter 1

Introduction

1.1 Symmetries - Valuable but Violate

In the pursuit of a physical theory to describe our observed universe, physicists have long used symmetry as a guide. Symmetries, as well as possessing substantial aesthetic appeal, serve to limit the vast possibilities for viable theories, and often come hand-in-hand with rules for those quantities that must be conserved in any process. For example, a theory that does not distinguish between positions in space (space-translation symmetry), predicts the observed conservation of momentum. Of particular interest to modern theorists are the discrete symmetries; space-inversion or parity (P), particle-antiparticle exchange, or charge conjugation (C), and time reversal (T). Until the middle of this century, invariance under each of these symmetry operations was commonly taken for granted, and observations were consistent with these assumptions. For instance, a particle with a given intrinsic parity would only be observed to decay into a state of the same parity. In fact, this was how intrinsic parity was defined, and in this context arose what became known as the "tau-theta puzzle." The tau and theta particles appeared to be identical except for their intrinsic parities, and thus differing available decay modes, two and three pions, respectively. This led to the famous 1956 paper by Lee and Yang [1], wherein they examined previous experiments for specific evidence requiring universal parity symmetry and found none, prompting the suggestion that the tau and theta were actually the same particle acting under some parity-nonconserving influence. Within months, experimental evidence confirmed the existence of parity violation, commencing with the observation by C.S. Wu of ^{60}Co beta decay electrons being preferentially emitted antiparallel to the nuclear polarization (figure 1.1) [2].

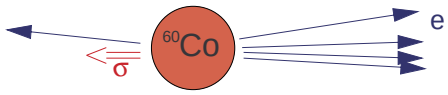

Figure 1.1: The first observation of parity violation showed the electrons of ^{60}Co were more likely to emitted in the direction opposite the nuclear spin.

Ironically, the weak interaction was soon shown to be maximally parity-violating, as further evidenced by the observation of neutrinos (which are solely weakly-interacting) with only a single possible helicity. It was also observed that charge conjugation was always violated in equal measure with parity. Antineutrinos, for instance, also have only a single helicity, yet it is the opposite as their matter partners. The symmetry product CP was actually conserved here since the C- and P-violations were equal and opposite. In fact, it was shown that the product of all three symmetries, CPT, must always be inviolate in any field theory, provided the theory is invariant under the proper Lorentz transformations, and constructed with field operators and derivatives to finite orders, with the normal boson/fermion spin statistics [3]. Among the consequences of this requirement are the equality of masses, lifetimes, and gyromagnetic ratios for particles and antiparticles, and all measurements so far are consistent with this requirement. Thus T-violation was not implied by the parity experiments since CP was still good.

While many scientists were just as comfortable with the assumption of perfect CP and time reversal symmetry as they had once been with P and C individually, this tranquility was short-lived. In 1964 a tiny violation of the product CP was seen in the decay of neutral kaons. The two CP-eigenstates of the K_0 pair should have very different lifetimes due to the difference in phase space of the available decay modes. The longer lived kaon, the K_{long}, decays into three pions while K_{short} decays into two. However, it was seen that approximately two in 1000 K_{long} decays was to two pions, signifying that the mass and CP-eigenstates are not identical [4]. This observation of CP-violation, which implies T-violation via CPT invariance, is particularly remarkable in that: (1) it is so small, and (2) it has yet to be seen in any other system since. The lack of further observations is consistent with the simplest explanation of this effect, which incorporates CP-violation into the Standard Model as a natural consequence of three generations of quarks. If the strong eigenstates mix in the weak interaction, the mixing matrix (called the Cabbibo-Kobayashi-Maskawa or CKM matrix) is specified by three angles and one imaginary phase [5]. This

phase gives rise to CP-violating effects, but is suppressed in most processes by the large mass of the heavy quarks on which it has the greatest effect. Coming experiments with B-mesons should also be sensitive to T-violation of this type. This theory is also further tested by looking at a wide variety of reactions to obtain the individual elements of the matrix and verify its unitarity.

1.2 Time Reversal Symmetry

In our everyday world, described by the theories of classical mechanics, the concept of time reversal invariance is one complicated by the notion of the "arrow of time." The distinction between backward and forward is provided by entropy, which always will increase in our forward moving world. But T-invariance only requires that nothing in the reversed movie violates a physical law. For instance, the time reversal of a object shattering is spontaneous reconstruction. The fact that we do not observe this process does not violate time reversal: it is not impossible, only extremely unlikely. To understand this we must consider the distinction between physical theory and statistical results. For a system as complicated as any macroscopic object, the large number of states available as the final result of a process means that motion reversal achieving the initial state can only occur if we can recreate the process with the precise initial conditions.

Classically, time reversal is equivalent to motion reversal, although one can easily make mistakes by not considering all motions involved. An example is the motion of a particle in a magnetic field, which would seem to violate time reversal if we fail to consider the microscopic currents creating the field and reverse those as well. In general, classical systems do not provide much opportunity to test time reversal.

Quantum systems provide a less complicated laboratory for investigating time reversal. Here the limited number of particles frees us from the confusion of statistical effects, yet it is here that a new subtlety emerges. The effect of the time reversal operator on a state is a replacement of $-t$ for t, but also includes a complex conjugation, which has the effect of interchanging initial and final states, as well as reversing momenta and spins in a process. This type of transformation was referred to by Wigner as antiunitary, being the product of a unitary transformation and the complex conjugation. The operation of T on a stationary state does not necessarily return the same state. $|\Psi'_E >= T|\Psi_E >$, and for systems with odd numbers of fermions, these two states are orthogonal. Yet, as long as T

commutes with the Hamiltonian, the energies of the two states are equal. For atoms in the absence of external fields, this is manifested in the degeneracy of pairs of states (Kramer's degeneracy.) Application of external electric fields preserves this degeneracy, but external magnetic fields, which change sign under T, split the levels.

1.3 Investigations

While the 1964 kaon experiment does *imply* T-violation, it is only this year that direct observations of any T-odd quantity have been made. In the decay $K_L \to \pi^+\pi^-\gamma^* \to \pi^+\pi^- e^+ e^-$ the decay products are emitted in two planes with a relative angle ϕ. This angle between the pion and electron planes must have an average value of zero if T is a good symmetry. However, it has been shown that the CKM theory predicts a rather large asymmetry in ϕ, given by [7]

$$dN/d\phi = A + B\sin^2\phi + C\sin 2\phi \tag{1.1}$$

where

$$\sin 2\phi = (\hat{n}_\pi \times \hat{n}_e)\cdot\hat{p}_\pi(\hat{n}_\pi \cdot \hat{n}_e). \tag{1.2}$$

This quantity is odd under time reversal since it involves an odd number of kinematic variables. It is simultaneously CP-odd, and arises by the same mechanism that induces the CP-violating K_0 mixing, yet its effect is amplified by two orders of magnitude. The KTeV group at Fermilab recently measured this asymmetry to be $13.5\% \pm 2.5\%(\text{stat.}) \pm 3\%(\text{syst.})$.

Another direct observation of T-violation has been seen at CERN by the CPLEAR group. They have studied the oscillation rates between the particle and antiparticle states of the neutral kaon, looking for a difference in the forward and backward reactions. Time reversal noninvariance allows an asymmetry

$$A_T = \frac{R(\bar{K}^0 \to K^0) - R(K^0 \to \bar{K}^0)}{R(\bar{K}^0 \to K^0) + R(K^0 \to \bar{K}^0)} \tag{1.3}$$

which is measured to be $(6.6 \pm 1.3(\text{stat.}) \pm 1.3(\text{syst.})) \times 10^{-3}$ [8]. This value is also predicted by CKM theory.

While these results are exciting and serve as further confirmation of the standard model, we still have yet to see CP or T-violation in systems other than kaons due to

the heavy quark loop suppression. Since the CKM contributions to most processes are practically unmeasurable, searches for T-violation serve as rigorous tests of the standard model and possible indicators of new physics.

Searches for T-violation outside the standard model have taken many forms. Tests of the strong force include nuclear scattering experiments where the reverse process is compared with the forward process. An experiment measuring the differential cross section for $Mg + \alpha$ scattering into $Al + p$, showed agreement between the two to 0.1% [9]. Similarly, a comparison of polarization produced by scattering protons on an unpolarized target was shown to be identical within 2.5% to the analyzing power for scattering of polarized protons on the target. These results were consistent with the expectation that time reversal is as good a symmetry in strong and electromagnetic interactions as are parity and charge-conjugation [10].

Tests of the weak force have been the focus of more careful study in an effort to pinpoint the true origin of the effect observed in the kaons. A large portion of the investigations that have been and are being pursued are measurements of T-violating quantities that would not arise (at a measurable level), from the CKM theory. A positive observation of such an effect would be a signal of new physics, something that cannot be accommodated in the existing Standard Model.

One type of search in this category is the attempt to measure a permanent electric dipole moment of a single fermion. Like a particle's magnetic moment, an intrinsic dipole moment must be either always aligned or always antialigned with the particle's spin. Any angle between the two would be a degree of freedom which would require an extra quantum number and be in disagreement with the fermi statistics observed. Under a time reversal transformation, the spin changes direction and the dipole moment with it. However, electric fields should be invariant under time reversal, thus the existence of a nonzero dipole moment violates this symmetry. The standard model predicts a neutron electric dipole moment of about 10^{-31}e·cm, and the present experimental limit is 10^{-25}e·cm [11, 12].

Another type of observable is a correlation in a decay process. Any quantity (such as a term in the differential decay probability) that depends on an odd number of kinematic parameters will violate time reversal, since all kinematic vectors (spins and momenta) change sign under T. The experiment described in this work is of this type, a search for the "D-coefficient" in neutron beta decay. This coefficient parametrizes the contribution to the decay probability of a particular "triple-correlation," the term depending

on the neutron spin and the momenta of the outgoing electron and neutrino [13]. The next chapter will discuss in detail this correlation and the experiments that have given a limit on the magnitude of D of 2×10^{-3}.

1.4 Non-Standard Models

There are many extensions to the standard model that permit extra time reversal invariance violation. There are a large number of theories that fall into the category of "supersymmetry" whereby every observed particle has a complementary supersymmetric partner. If there is a phase between the mass eigenstates and the eigenstates for a given interaction, a T-violating effect could arise [14]. Quantum chromodynamics leads to another possible T-violation due to its degenerate vacuum state. The true vacuum state can be expressed as a linear combination of all possible vacuum states,

$$|\theta\rangle = \sum_n e^{in\theta}|n\rangle \tag{1.4}$$

with the introduction of a phase angle, called "θ-QCD." A non-zero θ implies T-violation. A stringent test of this theory is the neutron electric dipole moment measurement.

A theory with wide appeal is the left-right symmetric theory of the weak interaction, which contains a right-handed W boson as well as the observed left-handed W. In this theory, beta decay can occur with either of these two bosons, as shown in figure 1.2. This

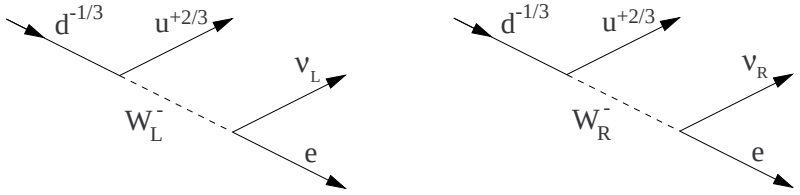

Figure 1.2: In a left-right symmetric model, there is an analogous beta decay scheme mediated by the right-handed boson W_R. This process is suppressed by the large mass of the W_R, but a mixing between the two bosons shows up as a T-violating phase.

W_R is much heavier than the W_L, thus its effects are suppressed, but the broken symmetries of P and C are restored at high energies. If the W_R and W_L are actually mixtures of two W mass eigenstates,

$$W_L = (W_1 \cos\zeta + W_2 \sin\zeta), \quad W_R = e^{-i\omega}(W_2 \cos\zeta - W_1 \sin\zeta), \tag{1.5}$$

where masses of the two eigenstates differ greatly in magnitude with a ratio (δ) of

$$\frac{m_{W_2}}{m_{W_1}} \equiv \delta \gg 1. \tag{1.6}$$

In this case there could arise a T-violation dependent on the phase ω, which survives as the W_R process interferes with the W_L process.

Presently there are experimental limits on these parameters from many processes, including muon decay, combining to give lower bounds of 485 GeV for m_{WR} ($\delta \leq 0.027$) and 0.033 for ζ [15]. Lack of observation of W_R by direct production at accelerators puts a lower limit on its mass somewhat higher at 650 GeV.

A different theory with new, "exotic" fermions exists, providing new avenues for fermion mass mixing and introduction of phases. The available parameter space for these theories to contribute to light-quark T-violation has been largely ruled out as the experimental limit on the electric dipole moment of the neutron has improved [16].

Recently, significant attention has been given to theories that contain particles called "leptoquarks," which allow transitions from quarks to leptons. Leptoquarks would have fractional charge of $\pm 1/3$ and $\pm 2/3$, and would be scalar or vector (spin 0 or 1), depending on the type of fermions making a vertex with the boson. Recent data on direct production experiments at HERA and ZEUS, detectors at the CERN accelerator facility in Switzerland, have produced evidence of something that could be a leptoquark. Analysis of the proton-positron scattering data has indicated the possibility of a leptoquark mass of order 200-400 GeV [17]. Investigations to clarify the observations are continuing.

To illustrate the contribution of a leptoquark to beta decay, consider the boson capable of making a u quark to ν transition and the one that takes d to e. If these mix in the mass eigenstate,

$$X_1 \to d + e, \quad X_2 \to u + \nu, \quad X_a = e^{-i\omega}(X_1 \cos\zeta + X_2 \sin\zeta) \tag{1.7}$$

they could mediate beta decay at "tree" level, as shown in figure 1.3.

This process could interfere with the usual beta decay diagram and the phase in the leptoquark state would survive, violating time-symmetry. Presently the measurements of the D-coefficient provide the best limit on leptoquark mixing. Electric dipole moments are not sensitive to this effect, because the initial and final fermionic states are the same (see figure 1.4). Thus, only a single leptoquark type mediates the process and does not contribute a phase.

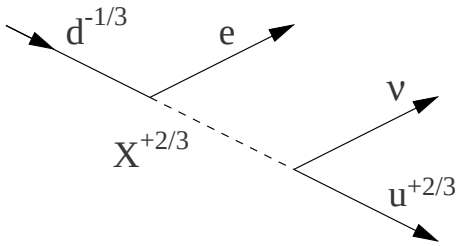

Figure 1.3: Diagram of a beta decay mediated by a leptoquark. The intermediate boson is the mixture of the two types that interact with d and e, and u and ν, respectively, and thus there is a relative phase between the two vertices.

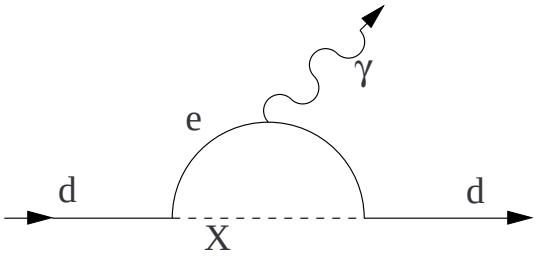

Figure 1.4: Diagram of an electric dipole interaction mediated by a leptoquark. The amplitude disappears due to T-invariance since the phases at the two identical vertices cancel.

1.5 Implications

Aside from the ever-present need to challenge our assumptions, there are other motivations for studying time reversal. The most dramatic of these is the need for T-violation to account for the observed matter-antimatter symmetry in the universe. The widely successful big bang theory posits the introduction of all matter into the universe in perfect balance with the antimatter via pair production in the early, energetic stages of development. Yet we have reason to believe that the objects that have survived to this day (after cooling and reannihilation of pairs) are primarily matter, representing a pre-annihilation quark asymmetry of three parts in 100 billion. The evidence for the present baryonic asymmetry can be scrutinized at different spatial scales. (1) Our solar system is primarily matter, or contact between bodies, such as planets, asteroids, and exploratory probes, would have proved catastrophic. (2) The cosmic rays which reach earth originate

throughout the galaxy, and are observed to be mostly matter. The small fraction of antimatter observed is explained by pair production in processes such as proton showers in the upper atmosphere. (3) On a larger scale the evidence is less straightforward. However, if there were regions of antimatter in the universe, we would see large numbers of gamma-rays due to annihilations at the interface with the matter regions. To explain the absence of this observation, one would have to propose a separation of these regions larger than is possible in present theories of the evolution of the universe [18].

A theory which would allow for the presently observed baryon asymmetry was formulated by Andrei Sakharov [19]. In this theory, processes must occur that convert baryons to antibaryons at different rates than the analogous antibaryon to baryon processes. Also, this must occur during a time in the universal evolution in which there was not a good thermal equilibrium, favoring certain reactions over their reverse processes. Thus we must have baryon number violation (present in all unified models, for example) as well as a non-equilibrium condition such as are present in many "inflationary" models of the universe. In addition, one can show that in order to achieve the rate difference, both C and T must be violated. The amount of T-violation present in the CKM explanation of the kaon data is not sufficient to produce the baryon asymmetry observed, adding fuel to the quest to measure a T-violating effect not predicted by standard model with CKM.

Chapter 2

History and Theory

2.1 Beta Decay Theory and Significance of Lifetime and Correlation Observables

All the observations of weak interactions can be described with an interaction Hamiltonian of the vector minus axial vector (V-A) type. For beta decay of a d to a u quark this has the form

$$H_{int} = \frac{1}{\sqrt{2}} G_F V_{ud} (\bar{\Psi}_u (1-\gamma_5)\gamma^\mu \Psi_d)(\bar{\Psi}_e (1-\gamma_5)\gamma_\mu \Psi_\nu), \tag{2.1}$$

G_F is the Fermi constant,$1.1664 \times 10^{-5} GeV^2$, and V_{ud} is the relevant element of the CKM matrix. V_{ud} is the same as the cosine of the Cabbibo angle, θ_C, which is approximately 13^o. The V-A nature leads to the observed $-v/c$ polarization of the electron in beta decay and to a right-handed antineutrino. This interaction violates P and C asymmetry completely. When we look at the interaction with nucleons instead of isolated quarks, we find that the V and A terms now have different strengths and that extra terms have arisen in the nucleonic current due to the effect of the strong force.

$$\begin{aligned} H_{int} = (\bar{\Psi}_p (g_V \gamma_\mu + g_A \gamma_5 \gamma^\mu + g_M \sigma^{\mu\nu} q_\nu + g_S q^\mu + g_T \gamma_5 \sigma^{\mu\nu} q_\nu \\ + g_P \gamma_5 q^\mu) \Psi_n)(\bar{\Psi}_e (1-\gamma_5)\gamma_\mu \Psi_\nu) + h.c. \end{aligned} \tag{2.2}$$

The constants g_V and g_A express the renormalization of the weak current by the strong force. The additional terms are known as "induced" terms and, being proportional to momentum transfer, are generally much smaller than the first order V and A portion of the interaction.

Neutron decay, shown in figure 2.1, is a "mirror" decay, one for which the initial and final states are isospin analog states. The decay probability can be found in the "allowed

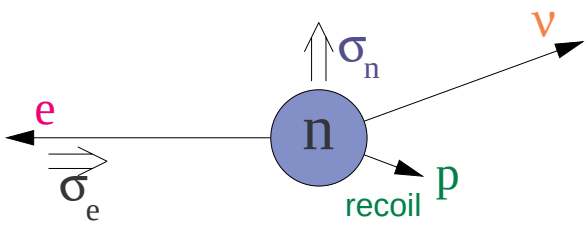

Figure 2.1: Neutron beta decay.

approximation", neglecting the terms of first order in momentum transfer. With the neutron spin (σ_n) and the energy and momentum of the electron and neutrino as observables one has a differential decay rate of

$$dW = G^2 F(Z, E_e) \left(1 + a\frac{\mathbf{p_e}\cdot\mathbf{p}_\nu}{E_e E_\nu} + A\frac{\hat{\sigma}_n\cdot\mathbf{p_e}}{E_e} + B\frac{\hat{\sigma}_n\cdot\mathbf{p}_\nu}{E_\nu} + D\frac{\hat{\sigma}_n\cdot\mathbf{p_e}\times\mathbf{p}_\nu}{E_e E_\nu}\right) dE_e d\Omega_e d\Omega_\nu, \tag{2.3}$$

where $G = G_F V_{ud}$. $F(Z, E_e)$ is the Fermi function, expressing the effect of the electromagnetic attraction between the outgoing electron and the recoil nucleus. The Fermi function has no simple analytic expression, but in the nonrelativistic limit it is given by

$$F(Z, E_e) = \frac{2\pi\eta}{e^{2\pi\eta} - 1}, \quad \eta = \frac{Z\alpha E_e}{p_e}, \tag{2.4}$$

neglecting also the finite size of the nucleus [20]. For free neutrons this approximation is good to 0.02% [21]. If we define λ as the complex ratio of axial vector to vector coupling strengths g_A/g_V, we see that the correlation coefficients depend only on this ratio.

$$a = \frac{1-|\lambda|^2}{1+3|\lambda|^2}, \quad A = -2\frac{Re\lambda + |\lambda|^2}{1+3|\lambda|^2}, \quad B = -2\frac{Re\lambda - |\lambda|^2}{1+3|\lambda|^2}, \quad D = 2\frac{Im\lambda}{1+3|\lambda|^2}, \tag{2.5}$$

If λ is real, it can be measured with any one of a, A, and B. Presently the measured values are [22, 23]

$$\begin{aligned} a &= -0.102 \pm 0.003, \quad & \lambda_a &= -1.260 \pm 0.007, \\ A &= -0.1127 \pm 0.0006, \quad & \lambda_A &= -1.2576 \pm 0.0016, \\ B &= 0.990 \pm 0.008, \quad & \lambda_B &= -1.234 \pm 0.210, \end{aligned}$$

The lifetime of the neutron has explicit dependence on the coupling constants.

$$1/\tau_n \propto {g_V}^2(1+3|\lambda|^2) \tag{2.6}$$

Thus, we can extract g_A and g_V separately by combining this result from the λ values found above [22].

$$\begin{aligned}\tau_n &= 886.7 \pm 1.9s,\\ g_A &= (1.7930 \pm 0.0038) \times 10^{-62} Jm^3,\\ g_V &= (1.4263 \pm 0.0030) \times 10^{-62} Jm^3.\end{aligned}$$

A complement to the neutron data is data from decays whose initial and final states are both zero spin, such as ^{14}C and ^{14}O. These "superallowed" decays are pure Fermi interactions, and their lifetimes reflect directly on g_V [22].

$$g_V = (1.4173 \pm 0.0011) \times 10^{-62} Jm^3.$$

The discrepancy in these two g_V values has yet to be resolved. There is a discrepancy between the most recent measurement of A and the previous world average that has an effect on the neutron g_V, and there is some uncertainty about the nuclear physics theory that must be applied to extract g_V from the superallowed decays.

If g_A and g_V are both real, there will be no time reversal violation in beta decay. The D-coefficient is the only quantity described above which requires T-violation, arising via a phase between the two couplings. If we express λ as $|\lambda|e^{-i\phi}$, then D becomes

$$D = 2\frac{|\lambda|\sin\phi}{1+3|\lambda|^2}. \tag{2.7}$$

Figure 2.2 illustrates how the observation of a finite triple correlation violates motion reversal and thus time reversal.

The present limits on D and $\sin\phi$ from neutron measurements are [22]

$$D = -0.5 \pm 1.4 \times 10^{-3}, \quad -0.0044 < \sin\phi < 0.0019.$$

The A and B coefficients depend on the cosine of ϕ, but when we extract $\sin\phi$ from these measurements and the measurement of a, the limits are not as strict (see figure 2.3).

$$|\sin\phi| < 0.07$$

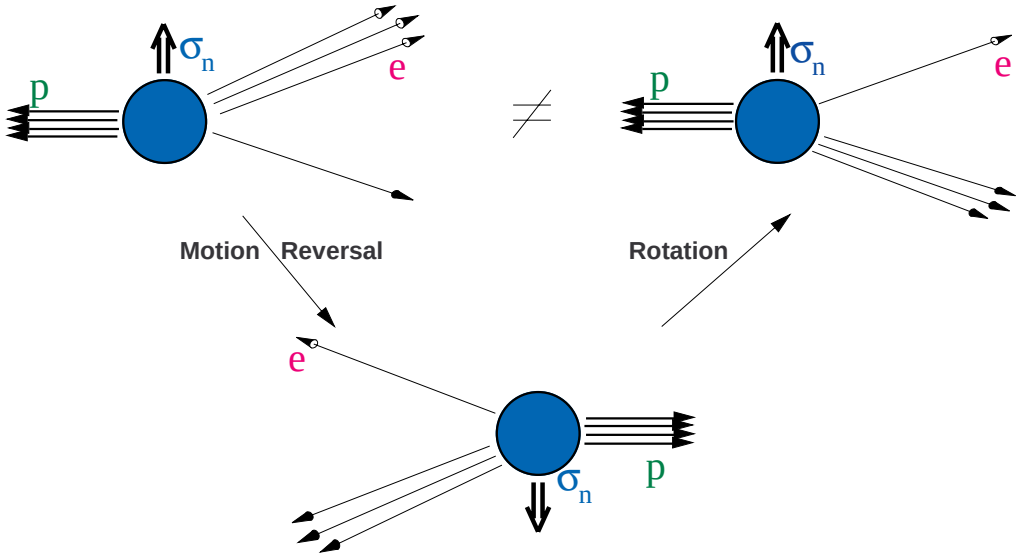

Figure 2.2: Illustration of motion reversal violation in beta decay. Under motion reversal, all momemta change directions. In upper left we see that, for a given proton momentum, there are fewer electrons emitted at 135° to the proton than are emitted at 225°. This gives a positive value for the triple correlation $\hat{\sigma}_n \cdot \mathbf{p}_p \times \mathbf{p}_e$. The same process, motion-reversed and then rotated, has a negative triple correlation. If motion reversal, which implies time reversal, were a good symmetry, this correlation would be zero.

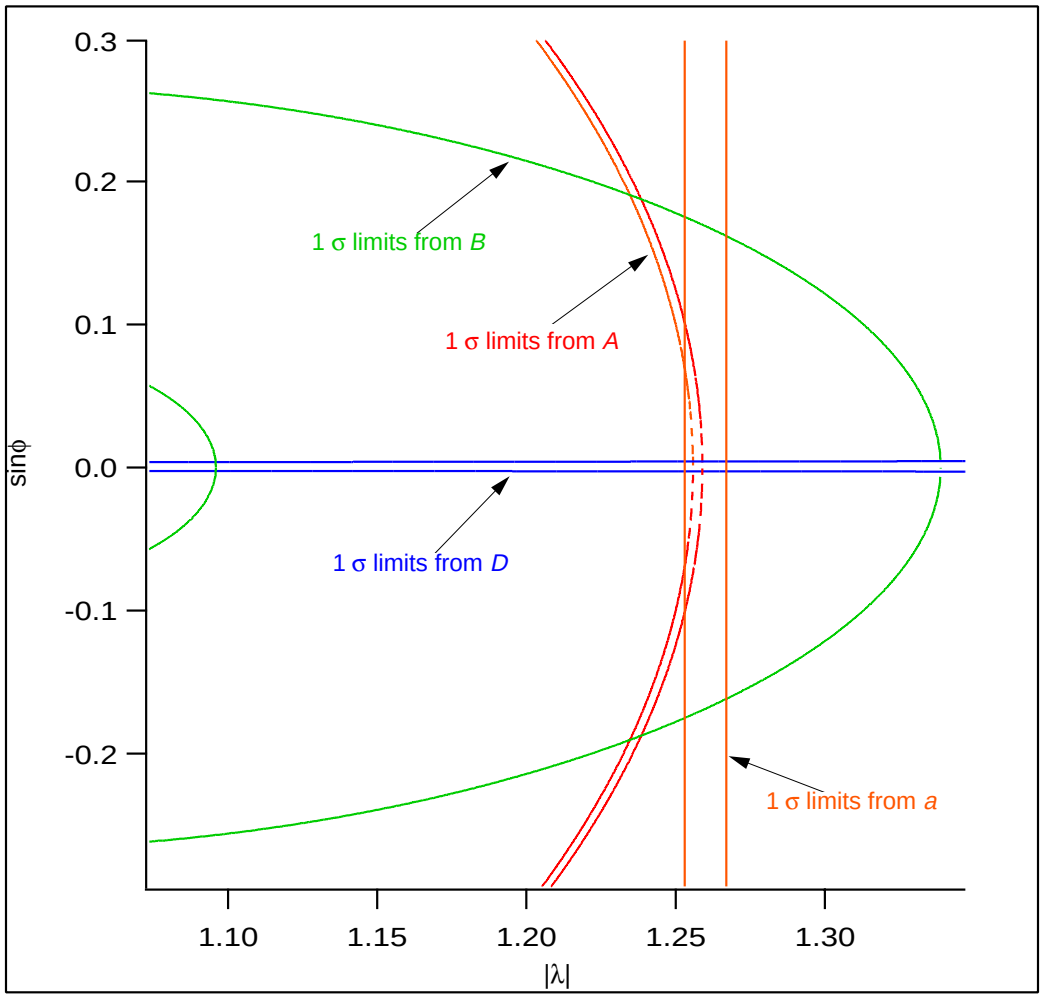

Figure 2.3: The correlation coefficients a, A, B, and D all depend on the ratio $\lambda = g_A/g_V = |\lambda|e^{i\phi}$. However, all but D have poor sensitivity to $\sin\phi$. Shown are the one standard deviation experimental limits.

The decay of neon-19 is also a mirror transition, although its matrix elements are different due to the nuclear structure. The present limit on D for neon is $D_{Ne} = 4 \pm 8 \times 10^{-4}$ [24].

2.1.1 General Weak Interaction

If we do not assume that the weak interaction is pure V-A, we write a more general form of the interaction including all possible operators.

$$H_{int} = \sum_{i=S,T,P,V,A} (\bar{\Psi}_p O_i \Psi_n) \bar{\Psi}_e (C_i + C_i^{'} \gamma_5) O_i \Psi_\nu) + h.c. \tag{2.8}$$

$O_S = 1, O_T = \frac{1}{2}\sigma_{\lambda\mu}, O_P = \gamma_5, O_V = \gamma_\mu, O_A = \gamma_\mu\gamma_5$. Then we can quantify the effect of these other operators on the observable parameters and test how the contributions of the scalar, tensor and psuedoscalar terms are limited by present observations. As mentioned earlier, the observed electron polarization requires that $C_{V,A} = -C_{V,A}^{'}$ and leads to right-handed antineutrinos. The same observation would imply $C_{S,T,P} = C_{S,T,P}^{'}$ if these exist, and would lead to a left-handed antineutrino.

In this notation, the D-coefficient is given by [13]

$$D\xi = 2Im\Big\{\delta_{J,J'}|M_F||M_{GT}|\sqrt{\frac{J}{J+1}}(C_S C_T^* - C_V C_A^* + C_S^{'} C_T^{'*} - C_V^{'} C_A^{'*})\Big\} \tag{2.9}$$

$$\xi = |M_F|^2(|C_S|^2 + |C_V|^2 + |C_S^{'}|^2 + |C_V^{'}|^2) + |M_{GT}|^2(|C_T|^2 + |C_A|^2 + |C_T^{'}|^2 + |C_A^{'}|^2) \tag{2.10}$$

$|M_F|$ and $|M_{GT}|$ are the matrix elements between the initial and final nuclear states for Fermi ($\Delta J = 0$) and Gamow-Teller ($\Delta J = \pm 1$ or 0, except $0 \rightarrow 0$) transitions. These matrix elements are 1 and $\sqrt{3}$ for free neutrons. Note that the psuedoscalar couplings do not contribute significantly to this or any decay parameter. This is because the psuedoscalar mixes the large and small parts of the nuclear wave function and the latter vanishes in the nonrelativistic limit, which is valid here. We also see on inspection that only nuclear decays which are mixed transitions can have a D coefficient. D is proportional to the sine of the phase between the vector and axial vector couplings. If there are scalar and tensor couplings, their contribution to D will be scaled by their magnitude and whatever phase exists between them.

Measurements of the Fierz interference coefficients in beta decay place limits on

the contributions of scalar and tensor interactions.

$$b_F = \frac{C_S^* C_V + C_S'^* C_V' + C_S C_V^* + C_S' C_V'^*}{|C_V|^2 + |C_V'|^2 + |C_S|^2 + |C_S'|^2}, \tag{2.11}$$

$$b_{GT} = \frac{C_T^* C_A + C_T'^* C_A' + C_T C_A^* + C_T' C_A'^*}{|C_A|^2 + |C_A'|^2 + |C_T|^2 + |C_T'|^2} \tag{2.12}$$

If we let $C_{A,V} = -C'_{A,V}$ and use the fact that we know $|C_{S,T}|^2 \ll |C_{A,V}|^2$, we see that

$$b_F \approx \frac{Re(C_S - C_S')}{C_V} \quad \text{and} \quad b_{GT} \approx \frac{Re(C_T - C_T')}{C_A} \tag{2.13}$$

The 90% CL limits on these two quantities from nuclear beta decay are [25, 26]

$$|b_F| < 0.006 \text{ and } |b_{GT}| < 0.016 \tag{2.14}$$

Reference [27] combines all of the measurements in neutron decay to set limits on these and other parameters which are not contained in the Standard Model.

2.2 Time Reversal Versus Motion Reversal and Final State Effects.

A complete treatment of this time-reversal violating parameter must take into account the fact that the symmetry's restriction on decay is not exactly equivalent to motion reversal invariance. Motion reversal invariance follows strictly from time reversal only to the extent that the transition operator is small enough that higher orders can be neglected as outlined below.

The S-matrix, which describes the probability for evolution from one state to another, is related to the transition operator by $S = I - iO$. We denote the transition operator O rather than the usual T to avoid confusion with the time reversal operator T. Since S is unitary,

$$SS^\dagger = (I + iO^\dagger)(I - iO) = 1 \tag{2.15}$$

$$\text{giving} \quad O = O^\dagger - iOO^\dagger \tag{2.16}$$

If O is small then to first order it is hermitian. For the transition $\langle f|O|i\rangle$, the time reversal operation reverses the initial and final states, and makes the complex conjugate of the matrix element.

$$\langle f|O|i\rangle \rightarrow \langle i'|O'|f'\rangle^* \tag{2.17}$$

$O^{'} = T^{\dagger}OT$ is the time-reversed transition operator and $f^{'}$ and $i^{'}$ have reversed spins and momenta. Thus

$$\langle f|O|i\rangle \rightarrow \langle f^{'}|O^{'}|i^{'}\rangle \tag{2.18}$$

only if $O^{'}$ is hermitian. If we compare an interaction to the same interaction with reversed spins and momenta rather than with reversed initial and final states, time reversal invariance requires that the two scenarios be identical only to lowest order in O. Even without time reversal violation, higher order terms of T-invariant interactions may create effects that are odd under motion reversal.

The lowest order transition operator neglects everything proportional to the recoil momentum of the daughter nucleus (< 750 eV for the proton) and electromagnetic interactions between the two charged particles in the final state. These correction terms are often collectively referred to as "final state effects" (FSE's.) Jackson, Treiman, and Wyld calculated the electromagnetic FSE in the general formalism, showing that the triple correlation coefficient acquires an additional term from pure Coulomb scattering of the electron and recoil nucleus [28]:

$$D^{EM}\xi = 2\Big\{\delta_{J,J'}|M_F||M_{GT}|\sqrt{\frac{J}{J+1}}\left(\mp\frac{\alpha Z m_e}{p_e}\right)Re(C_S C_A^* - C_V C_T^* + C_S^{'} C_A^{'*} - C_V^{'} C_T^{'*})\Big\} \tag{2.19}$$

The $\mp$ is for $\beta^{\mp}$ decay. This vanishes identically if the interaction is purely V and A. To estimate the contribution due to possible scalar and tensor couplings, we use the measured limits (90% CL) of the Fierz interference coefficients as presented in section 2.1.1.

$$D^{EM} \approx \frac{\alpha m_e}{p_e}\frac{Re(C_A C_V)}{|C_V|^2 + 3|C_A|^2}(b_F - b_{GT}) \tag{2.20}$$

$$|D^{EM}| < (2.8 \times 10^{-5})\frac{m_e}{p_e} \tag{2.21}$$

for the neutron.

In the absence of scalar and tensor couplings there is still a final state interaction that gives a significant non-zero FSE due to the electromagnetic scattering of the electron from the magnetic field of the proton. The weak scattering amplitude has a dependence on the nuclear magnetic moments from the "weak magnetism" induced term if strength g_M in equation 2.2. The final state effect comes in at recoil order $\alpha p_e/m_N$ [29].

$$D^{WM} = \pm\frac{Z}{A}\frac{\alpha}{4(1+3g^2)}\left(\frac{{E_e}^2}{p_e m_N}\right)\Big\{(1\pm 3g)[(f_1 \mp g) - 3G_1(1\mp g)] + \frac{{m_e}^2}{{E_e}^2}[(3\pm g)(f_1\mp g) + 3G_1(1\pm 3g)(1\mp g)]\Big\} \tag{2.22}$$

where

$$g = -\lambda \frac{M_F M_{GT}}{\sqrt{3}|M_F|^2} \tag{2.23}$$

$$f_1 = A(\mu_1 - \mu_2) \tag{2.24}$$

$$G_1 = 1 + \frac{A}{Z}\mu_f \tag{2.25}$$

μ_f is the magnetic moment of the recoil nucleus in units of nuclear magnetons, and μ_1 and μ_2 are the moments of the isospin $+1/2$ and $-1/2$ states, respectively. It is the conserved vector current hypothesis (CVC) that gives us the relation between f_1 and G_1 and the nuclear magnetic moments. For neutrons [29]

$$D_n^{WM} = \frac{{E_e}^2}{p_e m_N}(-0.032 + 0.040\frac{{m_e}^2}{{E_e}^2}) \tag{2.26}$$

which gives

$$D_n^{WM} = -5.7 \times 10^{-5} \tag{2.27}$$

at the maximum p_e value. This effect is almost an order of magnitude larger for neon, but could be experimentally distinguished from T-violating D signals by the energy dependence.

2.3 Measuring D.

To measure the triple correlation for free neutrons, the neutron spin is prepared by polarizing the beam, and the electron is easily detected using a variety of techniques. The neutrino cannot be detected. However, conservation of momentum allows the neutrino momentum to be inferred by detecting the recoil proton. For cold neutrons, the small momentum of the neutron can be neglected and the sum of all of the final state momenta vanishes. We then can make the substitution

$$\mathbf{p_e} \times \mathbf{p}_\nu = -\mathbf{p_e} \times \mathbf{p_p} \tag{2.28}$$

and measure

$$-D\frac{\hat{\sigma}_n \cdot \mathbf{p_e} \times \mathbf{p_p}}{E_e E_\nu}. \tag{2.29}$$

The experiment described in this work utilizes four each electron and proton detectors centered around a polarized neutron beam as shown in figure 2.4. The recoil protons have a maximum energy of 750 eV and must be accelerated through high voltage before they can be detected.

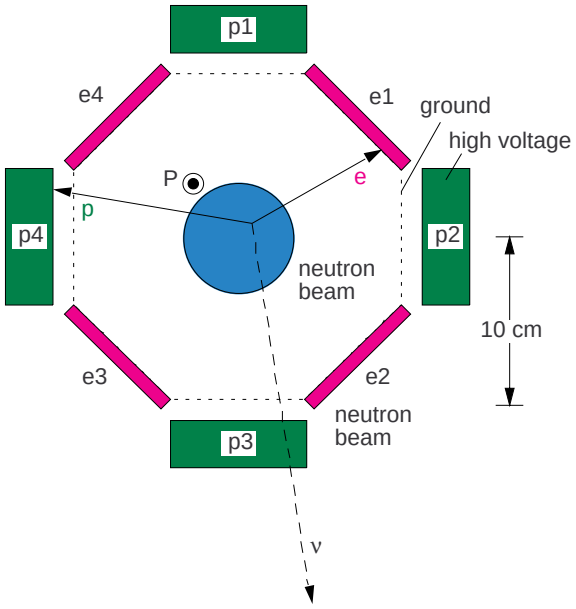

Figure 2.4: This schematic of the emiT experiment represents a cross section of the detector. The polarization of the beam is known, and a coincidence is detected if the proton and electron hit detectors of the correct type. The neutrino simply passes through the apparatus.

2.3.1 Previous Neutron D Measurements.

The most recent measurements of the neutron D were made in the 1970's by groups in France at the Institute Laue-Langevin (ILL) and at the Kurchatov Institute near Moscow. The most precise measurement used the geometry shown in figure 2.5, and yielded the result $D = -1.1 \pm 1.7 \times 10^{-3}$ [30].

The ILL experiment had proton detectors of thin NaI film and plastic scintillators for detecting electrons. These were arranged at right angles into two banks of detectors around a rectangular beam. A polarization of 70% was achieved using a curved magnetized neutron guide tube. The stated error on the result is statistical.

The Kurchatov group detected protons with CsI films inside large spherical focusing electrodes as shown in figure 2.6. The narrow beam of neutrons was polarized to 85% using a cobalt mirror. The result of $D = 2.2 \pm 3.0 \times 10^{-3}$ was that obtained after extensive reanalysis of systematic effects [31, 32].

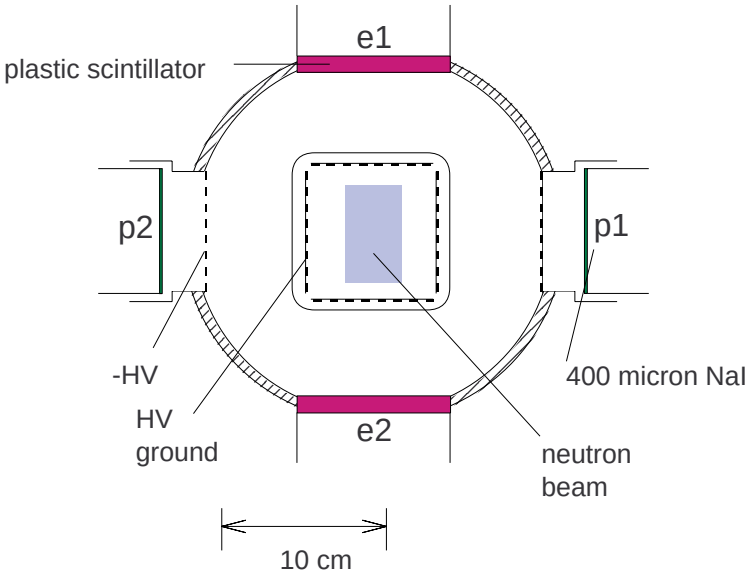

Figure 2.5: The apparatus of Steinberg et al.

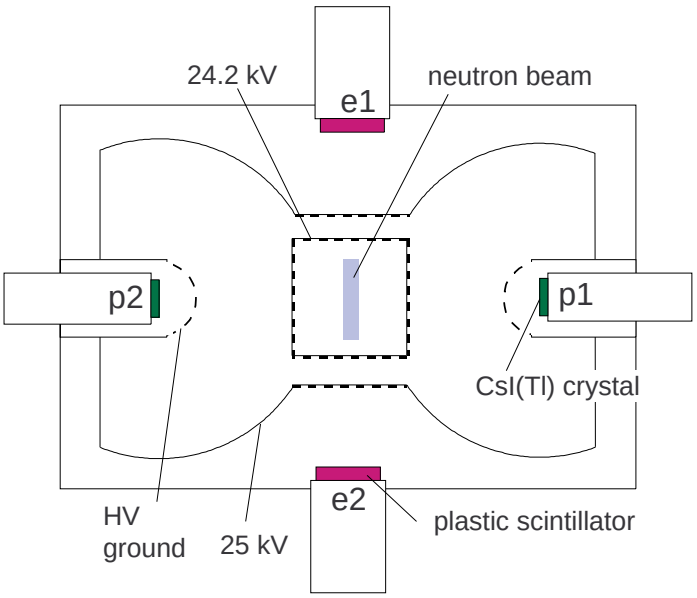

Figure 2.6: The apparatus of Erozolimskii et al.

2.3.2 Previous Neon D Measurements.

The most recent neon measurement was made by a group at Princeton with the apparatus illustrated in figure 2.7. The ^{19}Ne, made at the Princeton cyclotron, is collimated into an atomic beam and polarized using a Stern-Gerlach magnet. The beam then passes into a cylindiral cell whose walls are coated with MgO, which enhances the production of secondary electrons when the recoil fluorine ion from the decay strikes the surface. These secondary electrons are accelerated to the end of the cell, where they are detected by microchannel plates. The positron produced has endpoint energy of 2.2 MeV, and is detected by curved scintillators completely surrounding the cell. Their result is $D_{Ne} = 4 \pm 8 \times 10^{-4}$ [24]. An improvement on this measurement is currently being developed.

An earlier measurement by a group at Berkeley used secondary emission ion detectors and scintillators arranged in an octagonal geometry much like that of the emiT apparatus (see figure 2.8) [33].

2.4 Other Correlation Observables in Beta Decay

In the beta decay probability given by equation 2.3, we integrated over all final spin states because the experiment is insensitive to them. Experiments capable of detecting final spin states measure certain other correlations which are also T-violating but sensitive to other combinations of couplings. There are, for instance,

$$R\hat{\sigma}_n \cdot (\hat{\sigma}_e \times \mathbf{p_e}) \quad \text{and} \quad L\hat{\sigma}_e \cdot (\mathbf{p_e} \times \mathbf{p}_\nu). \tag{2.30}$$

The difficulty in measuring $\hat{\sigma}_e$ is comparable to that in detecting recoil momenta, and L, requiring both, has never been measured. The R-coefficient has been measured in ^{8}Li and a measurement in neutron decay is being designed [34]. On inspection of the general expression for R,

$$\begin{aligned} R\xi = 2Im\Big\{ \pm \lambda_{J,J'} |M_{GT}^2| (C_T C_A^* + C_T^{'} C_A^*) \\ +\delta_{J,J'} |M_T||M_{GT}| \sqrt{\frac{J}{J+1}} (C_S C_A^{'*} + C_S^{'} C_A^* + C_V C_T^{'*} - C_V^{'} C_T^*) \Big\} \end{aligned} \tag{2.31}$$

it is apparent that R vanishes in pure V and A theory, regardless of the existence of a V-A phase. Instead it is sensitive to interference between the S and A and/or T and V couplings. The current limit on R in ^{8}Li is $R = 0.9 \pm 2.2 \times 10^{-3}$. ^{8}Li is a purely Gamov-Teller decay,

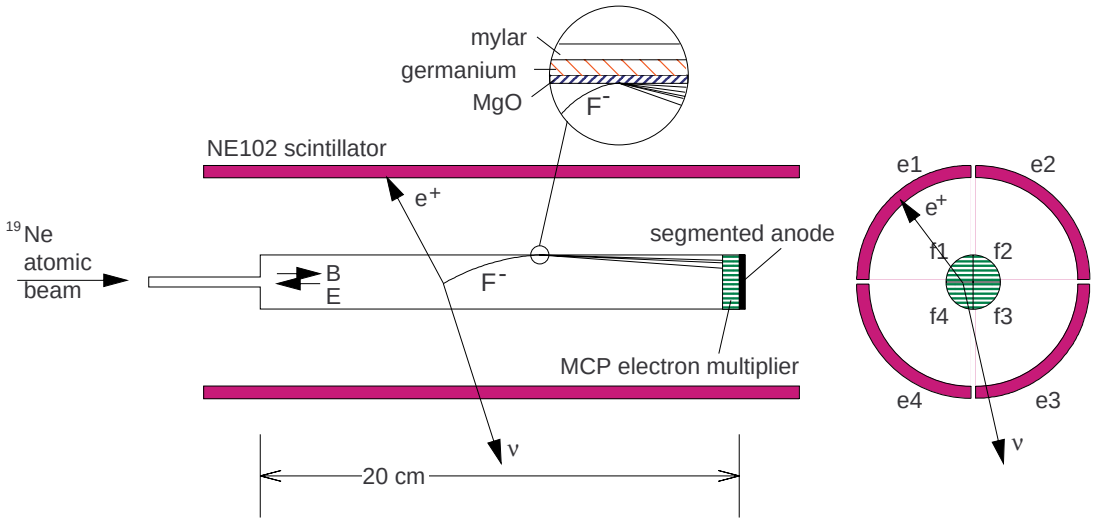

Figure 2.7: The apparatus of Hallin et al. for measuring D in Ne.

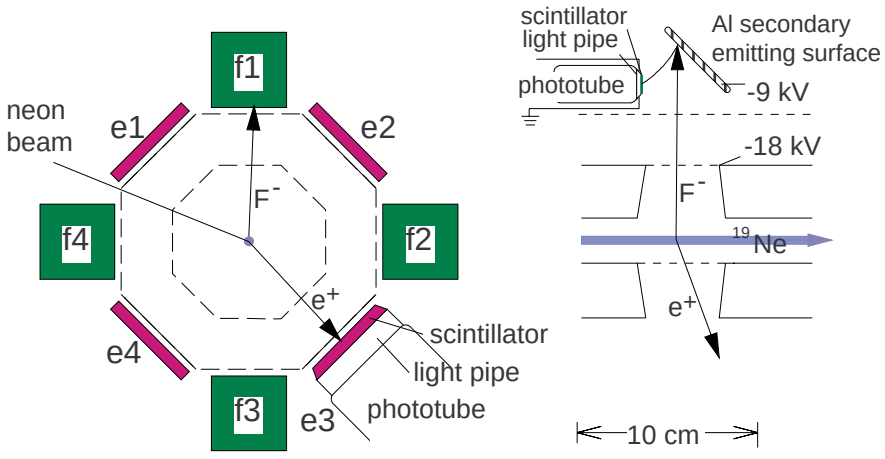

Figure 2.8: The apparatus of Calaprice et al.

and from this measurement, stringent limits can be placed on the imaginary part of the tensor couplings.

$$-0.015 < Im\left(\frac{C_T + C_T'}{C_A}\right) < 0.009 \tag{2.32}$$

Since neutron decay is a mixed decay, a neutron R measurement will give a limit on the scalar couplings as well as the tensor.

Another type of correlation can be measured with a nucleus that emits a photon (of wavevector $\hat{k}$) following the beta decay. The correlation is

$$E_1 \hat{\sigma}_n \cdot (\hat{k} \times \hat{p}_e)(\hat{k} \cdot \hat{\sigma}_n). \tag{2.33}$$

The present limit on E_1 is -0.001 ± 0.006 for ^{56}Co [35].

2.5 Predictions for D.

As discussed above, all models which are capable of inducing a measurable D are limited by the neutron dipole moment measurements, except for theories with leptoquarks. The present theoretical bounds are listed in table 2.1.

Theory	D
Standard Model	$< 10^{-12}$
Theta-QCD	$< 10^{-14}$
Supersymmetry	$\lesssim 10^{-7} - 10^{-6}$
Left-Right Symmetry	$< 10^{-4}$
Exotic Fermion	$< 10^{-4}$
Leptoquark	$\leq$present limit

Table 2.1: Theoretical limits on D.

The CKM and θ-QCD contributions are calculated by Herczeg and Kriplovich using the present stringent limits on the CKM phase δ ($|s_2 s_3 s_\delta| \lesssim 10^{-3}$ radians) and $|\theta| \lesssim 10^{-10}$ radians [36]. The result for supersymmetry depends on the mass of the supersymmetric particle, constrained by experiment, and the phase of the coupling, which is unconstrained [14]. Still, the largest possible value is below the final state effects. The Left-Right Symmetric and Exotic Fermion theories are most tightly constrained by the neutron

electric dipole moment (d_n) [37]. If one takes the result of the ^{199}Hg electric dipole moment experiment [38], limits of $D < 10^{-5}$ can be calculated for both theories. However, uncertainties in these calculations loosen the constraint by an order of magnitude. At present, only the leptoquark theory is limited by the D-coefficient experiments [39].

Chapter 3

Apparatus

The present experiment (emiT) utilizes a beam of cold neutrons from the Cold Neutron Research Facility (CNRF), located at the National Institute of Standards and Technology in Gaithersburg, MD. The neutrons are transported via a totally reflecting neutron guide to the apparatus. A schematic of the apparatus is shown in figure 3.1. The beam passes through a polarizer, beam tubes, a spin flipper, and a set of collimators into a region where decays are detected by an array of beta and proton detectors (see figure 3.2). Polarization is maintained by magnetic fields. Commercial and custom electronics was used to process signals and write the events and monitor information to compact disks.

The eight detectors surround the beam, each 10 cm from the beam axis. The octagonal geometry places beta and proton detectors at relative angle of 45 and 135 degrees. The preference for larger electron-proton angles in the decay makes 135° the coincidence angle with the greatest sensitivity to the D-coefficient, rather than the 90° coincidence angle at which the cross product is greatest (see figure 3.3). This detector and collimator geometry were chosen optimize the sensitivity to D after a comparison of geometries was made with Monte Carlo simulations [40]. A prototype run at the CNRF was completed in 1992.

3.1 Neutron Source

The NIST reactor is a 20 MW research reactor with several thermal beams and a cold source packed tightly around the core to achieve high fluxes of neutrons at the beam ports [41]. Cold neutrons are defined as those having a temperature below 60K, traveling

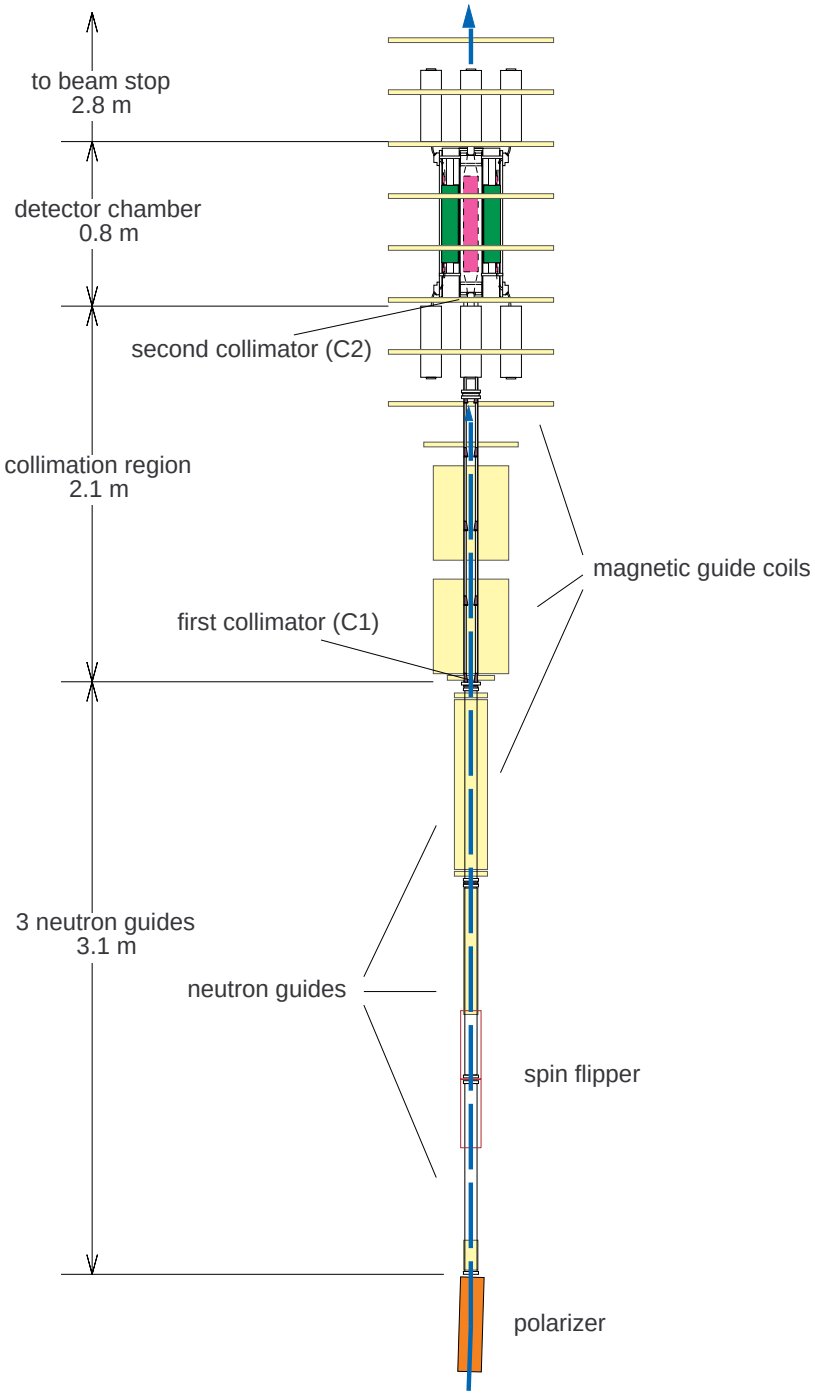

Figure 3.1: The emiT experimental apparatus beamline layout. The neutrons traveled through 8.8 meters of guides and vacuum components before reaching the beam stop.

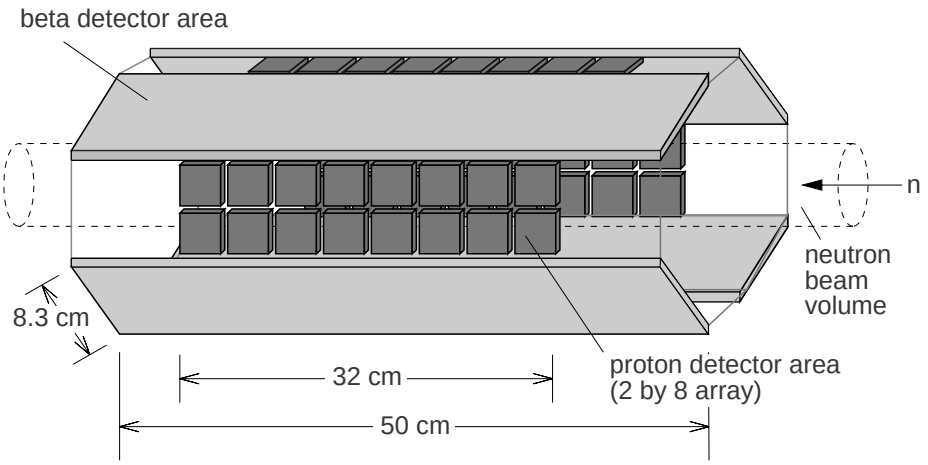

Figure 3.2: Basic detector geometry - an octagonal array of four each proton and electron detectors.

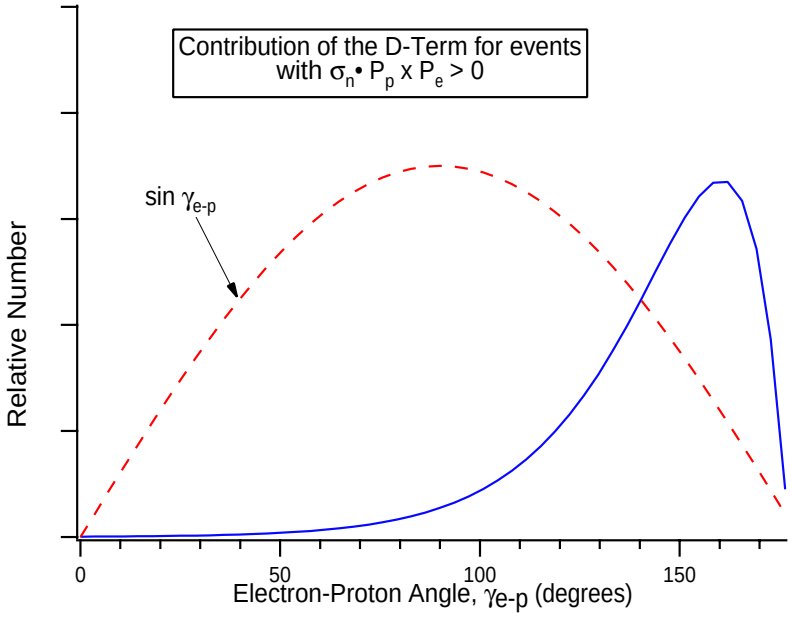

Figure 3.3: Increased sensitivity to the cross product and increased rate due to phase space are mutually maximized at coincidence angles near 135°.

at 1000 m/s or less, with energies less than 5 meV (as compared to the 1-2 MeV of the neutrons created by uranium fission.) Neutrons from the reactor first thermalize in room temperature heavy water (D_2O), and then enter the cold source shown in figure 3.4. The cold source moderator is liquid hydrogen condensed and cooled with circulating helium gas to 20 Kelvin. Neutrons with a 40K roughly Maxwellian velocity distribution are delivered to 8 neutron guides as shown in figure 3.5. The neutron guides take advantage of neutron

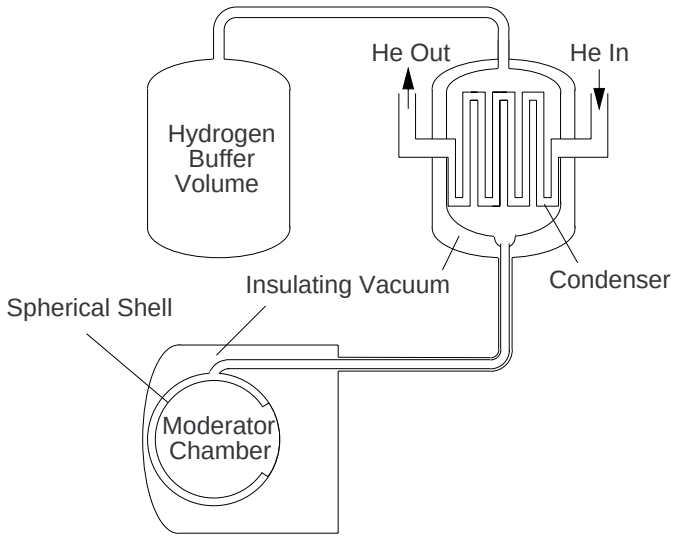

Figure 3.4: NIST cold neutron source. The moderator is a spherical shell 2 cm thick with an outer diameter of 32 cm, filled with about 5 liters of liquid hydrogen. A 20 cm diameter opening illuminates 8 neutron guides.

optics, which, like light optics, allows total internal reflection in a region whose index of refraction is greater than that at the boundaries. Neutrons traveling in vacuum can be internally reflected if the guide walls have a refractive index less than unity. The guide walls are made of glass coated inside with ^{58}Ni, whose index of refraction for neutrons is determined by

$$n^2 = 1 - \lambda^2 \left(\frac{N a_c}{\pi} \right), \tag{3.1}$$

depending on the wavelength λ, the coherent neutron scattering length a_c, and the atomic density N. The critical angle for total reflection is thus $\lambda\sqrt{Na_c/\pi}$, which for ^{58}Ni is 0.02 radians times λ in nm. For a neutron velocity v=1000 m/s, λ is 0.4 nm and the neutrons are accepted into less than one millisteradian. Once inside the guides the transmission is

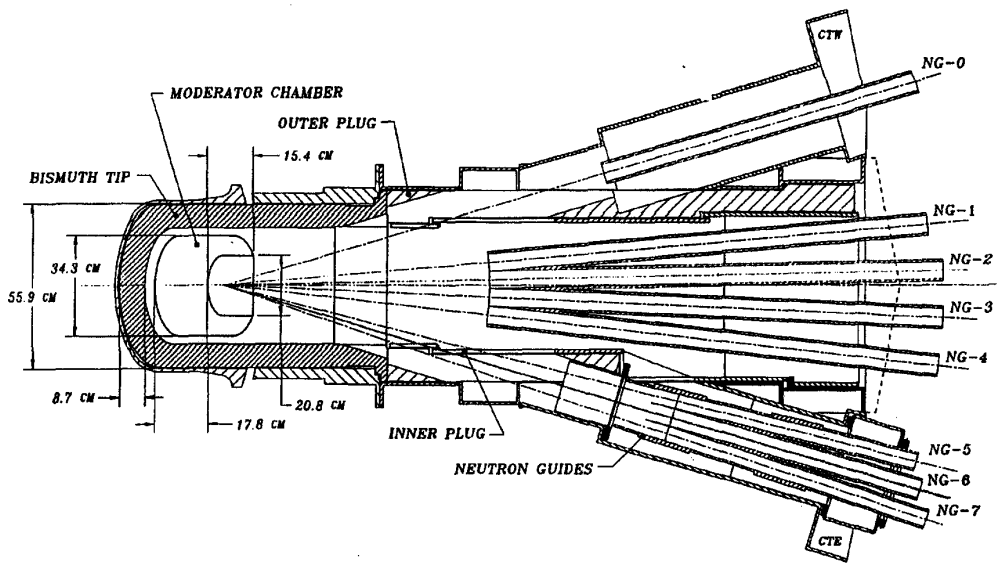

Figure 3.5: The NIST neutron guides are used to transfer the neutrons away from the cold source, which is close to the reactor core, through an 8 meter shielding wall into a low-background experimental area.

limited only by surface imperfections. A vacuum of approximately 7 mtorr is maintained in the guide to prevent reduction of the reflectivity due surface contamination. This pressure is 100 times lower than the pressure for which neutron scattering is significant. The CNRF guides were shown to have less than 1% loss per meter, and the loss over the 68 meters of neutron guide NG-6, is on the order of tens of percent. This low-divergence, low-loss transport technique brings the neutron beam through a 8 m reinforced concrete wall and further from the reactor into a region with greatly reduced gamma-ray flux. The guides are shielded with steel, paraffin, and borax.

When the NG-6 end shutter is opened, the beam passes through a cryogenically cooled beam filter ("cryofilter") of 10-15 cm of polycrystalline bismuth and beryllium. In these crystals, with lattice spacings d (3.3 Å for Bi), diffraction occurs if the condition [42]

$$2d \sin\theta = n\lambda \tag{3.2}$$

is met, with θ the angle between the incident neutrons and the crystal plane and λ the wavelength of the neutrons. No scattering will occur if $\lambda > 2d$, and thus cold neutrons

pass through the crystal while neutrons of shorter wavelengths will scatter as they meet the diffraction condition in one or more of the crystals of the polycrystalline sample. The effective cutoff wavelength for bismuth is 6.5 Å or 1.7 meV. The bismuth also absorbs gamma-rays from the reactor that would contribute to the background signal. Cooling the crystals increases their transmission of cold neutrons.

The reactor runs in 6-week cycles with 8-10 days between cycles for refueling and maintenance. For its first run, the experiment was allotted several cycles for beam development and data collection. The flux of neutrons from the NG-6 guide was measured using the gold foil activation technique. In this method, neutrons are absorbed by ^{197}Au in a foil of 76 μm thickness and 3.2 mm diameter. The gamma particle radiation from the ^{198}Au produced is subsequently measured with a germanium gamma-ray spectrometer. The cross section for neutron capture is inversely proportional to the neutron velocity.

$$\sigma(v) = \sigma_0 v_0 / v \tag{3.3}$$

A target is irradiated with a neutron beam of density distribution $n(v)$. If the target is thin enough to have negligible attenuation of the beam, the total number of captures will be

$$N_0 = N_T t_i \int n(v) v \sigma(v) dv = N_T t_i \sigma_0 v_0 n \tag{3.4}$$

where N_T is the number of target nuclei, $n = \int n(v)dv$ is the integrated density, and t_i is the irradiation time [42]. The subsequent activity A of the foil at a later time t is given by

$$A = \frac{N_0}{\tau} e^{t/\tau} \tag{3.5}$$

where τ is the lifetime of ^{198}Au, 3.89 days. From the measurement of the activity the "capture flux" $\phi_c = n v_0$ can be extracted. The capture flux is the relevant quantity for this experiment as the density of neutrons in the detector chamber, and thus the decay rate, is also proportional to $1/v$. The efficiency of the Ge detector is measured to be 0.003 at 411 keV and the number of ^{197}Au at natural abundance in the foil is determined to be approximately 2×10^{20}). Each foil spends one hour in the beam, and the capture flux at the NG-6 shutter was measured to be 1.4×10^9 n/cm^2. Further measurements of the beam were made with fission chambers. In this method the neutrons are absorbed by a ^{235}U substrate and the tracks from the fission products are detected. The uranium capture deviates from pure $1/v$ behavior by a factor of 0.976.

3.2 Polarization

The neutron polarizer utilizes the neutron optics principles discussed above, taking advantage of the refractive index's dependence on the magnitude and orientation of an applied magnetic field.

$$n^2 = 1 - \lambda^2 \left(\frac{N a_c}{\pi} \pm \frac{2 m_n \mu B}{h^2} \right) \tag{3.6}$$

where μ is the neutron magnetic moment (-6.03×10^{-14} MeV/Tesla), m_n is its mass (939.6 MeV), and the $\pm$ is indicative of the relative orientation of the neutron spin and applied field (of strength B.) If the magnitude of the second term in the parentheses is larger than the first, the value of n will be greater or less than unity depending on the spin orientation . The spin state parallel to the field will experience total internal reflection, and the antiparallel state will refract. This separates an unpolarized beam incident on such a surface into two beams.

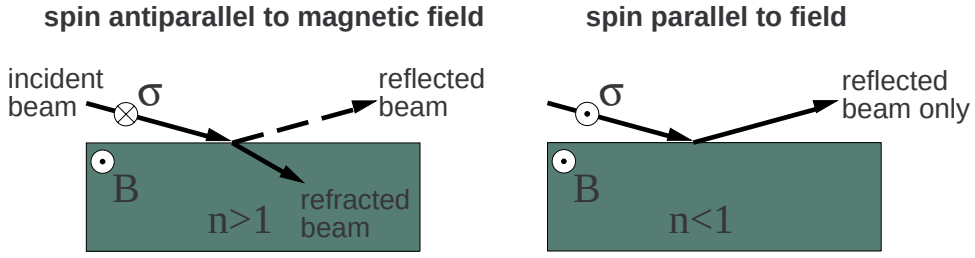

Figure 3.6: If a sufficiently large external magnetic field is applied to a reflecting material, the surface will reflect neutrons with spins parallel to the field and refract those antiparallel to it.

The neutrons are polarized with a double-sided "supermirror"-type polarizer (see figure 3.7) obtained from the Institute Laue-Langevin in Grenoble, France [43]. The supermirror (SM) consists of 40 glass plates with coatings on each side which maximize the reflection of the desired spin state while absorbing nearly all of the other. The outer surface of each plate is covered with several reflecting layers of cobalt and titanium, each layer a few angstroms thick. Beneath those are layers of gadolinium and titanium, which further refract and absorb the neutrons of the wrong spin state. These layers are evaporated onto 0.2 mm $\times$ 6 cm $\times$ 33 cm Pyrex plates which contain boron to absorb the refracted neutrons. Each plate is slightly curved to a radius of 10 m, allowing a greater portion of the incident beam to satisfy the grazing angle reflection criteria, and preventing any neutron

from traversing the length of the supermirror without encountering a reflecting surface. The plates are stacked together, separated by 1 mm spacers in a housing that incorporates the necessary applied field of 300 gauss parallel to the plates and perpendicular to the neutron travel direction. The full polarizer is capable of polarizing an unpolarized 4.5 by 5.5 cm beam with 24% transmission and greater than 95% polarization.

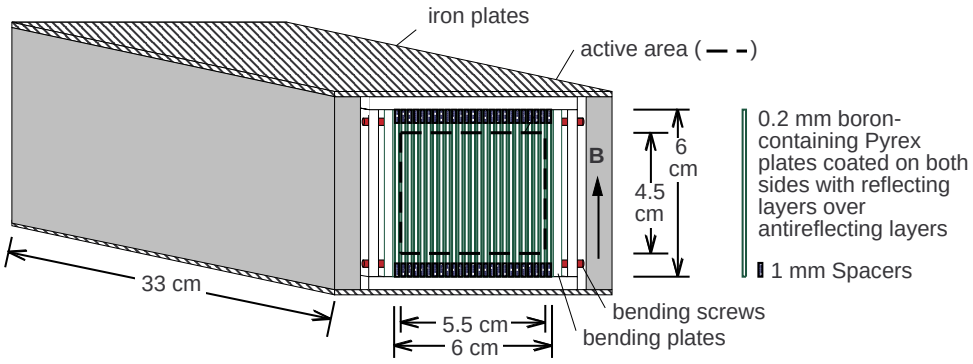

Figure 3.7: Geometry of the supermirror polarizer, constructed of 40 coated Pyrex plates separated by spacers.

The polarizer was mounted inside a housing of steel filled with 18 cm of lead, which shielded the experiment and personnel from gamma-rays produced by neutron absorption in the gadolinium.

3.3 Beamline

Figure 3.8 shows the layout of the emiT experiment as installed at the NIST CNRF. In this figure, the lead and concrete shielding walls can be seen, as well as the experimental support systems. After polarization, the neutrons travel within a series of beam tubes as they move toward the detector region. Three Pyrex glass beam tubes, 1 m in length and 6 cm in diameter with wall thicknesses of 3 mm, were lined with beryllium, a good neutron reflector. Neutrons travel through one of these beam tubes between the polarizer and spin flipper. This tube is capped with on each end with silicon windows of 0.5 mm thickness , and there is a constant stream of helium gas through the tube, reducing the neutron absorption well below the level in air. Transmission through each tube was expected to be 97%.

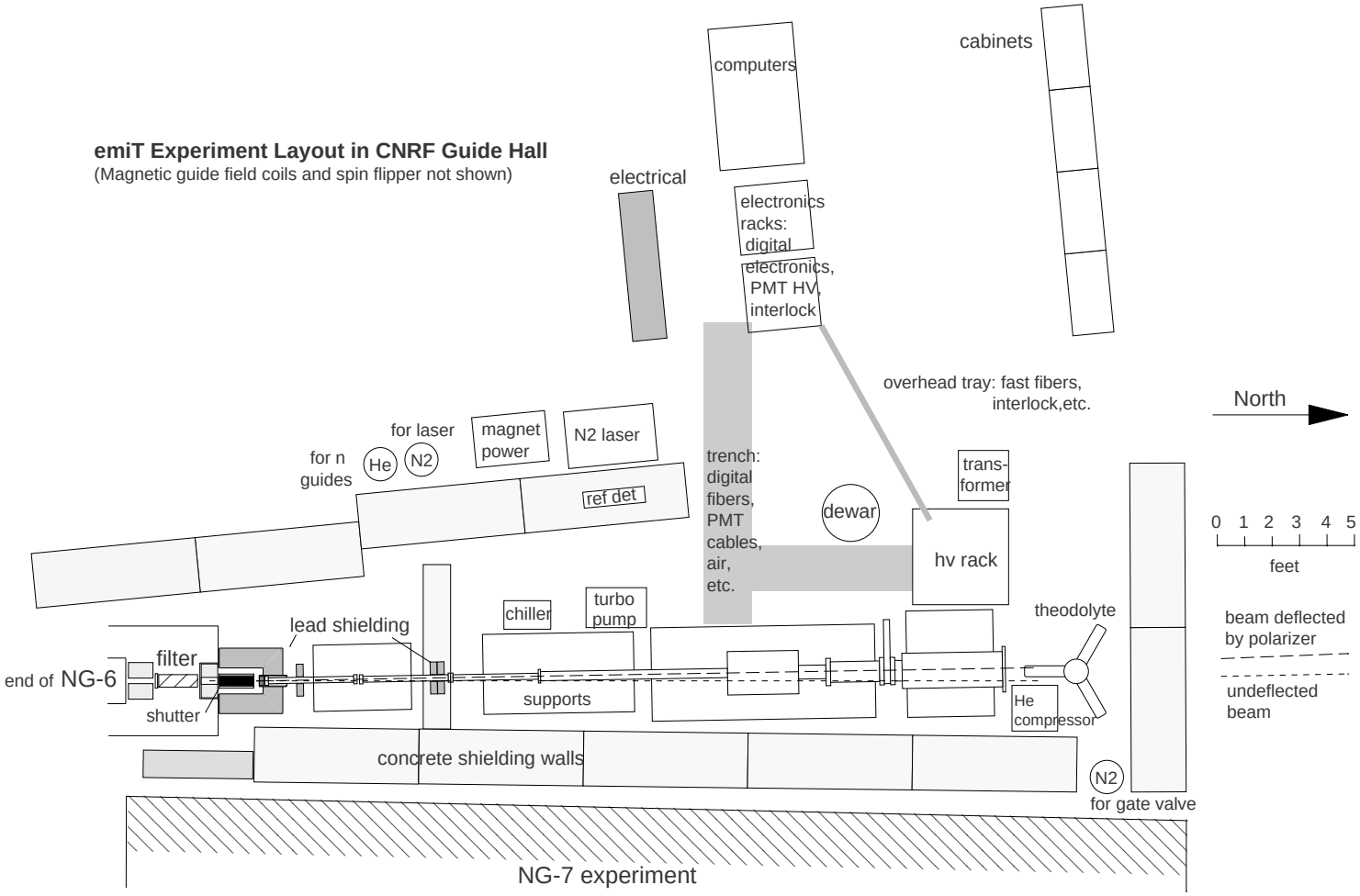

Figure 3.8: The experiment was assembled at the end of neutron guide 6 in the NIST CNRF Guide Hall.

Just past the spin flipper the neutrons pass through a silicon window into a second identical glass beam tube under vacuum, connected to a third glass tube and all of the downstream vacuum components. The collimator is constructed inside five sections of 9 cm inner diameter aluminum vacuum pipe. All of the beam tubes are mounted on Velmex Screw-Motion Unislide translation stages with non-magnetic bearings and hardware. A flexible annealed steel bellows, compressible from 2.9 cm to 0.8 cm, connects the second and third glass guide tubes. A second bellows connects the third guide tube to the first collimator pipe, and a third connects the last two pipes of the collimator assembly. These flexible connections prevent stress between the respective portions of the beamline that could destroy the alignment.

The collimator array, shown in figure 3.9, consists of seven flat (32 mm thick) "scraper" rings of lithium fluoride enriched to 93% with the neutron-absorbing ^{6}Li isotope. The scrapers are backed by thick rings of high-purity lead which absorb the gamma-rays produced by neutron captures in the scrapers. Between collimators, the walls of the tube are lined with 63 mm of ^{6}Li-loaded glass to absorb stray neutrons. The first and last collimators (C1 and C2) have openings of 6 cm and 5 cm, respectively, and are spaced 2 m apart. These define the beam shape. The other five components (S1-5) remove divergent neutrons. The characteristics of the collimator components are given in table 3.1.

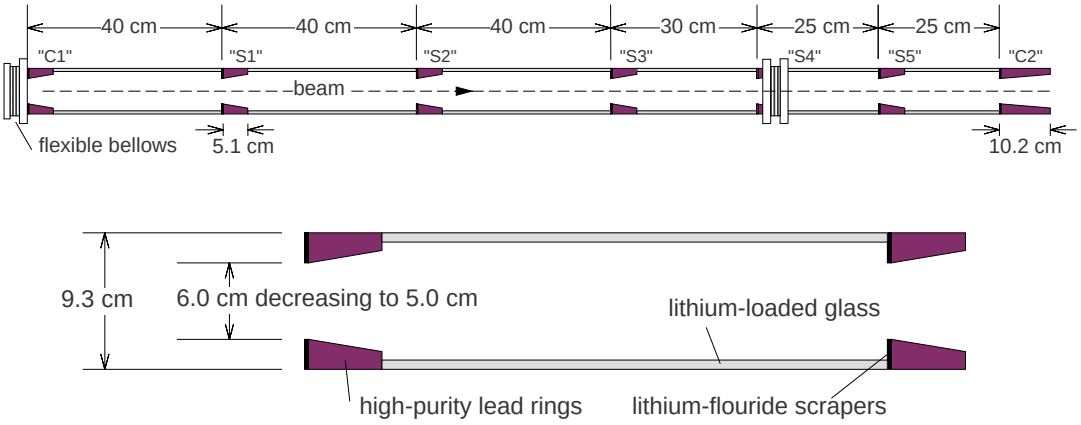

Figure 3.9: emiT collimator components.

The collimator performance was studied with a Monte Carlo simulation of neutrons in a beam being transmitted from the neutron guide through the collimator into the detector

Collimator Component	Distance from C2	Scraper Ring I.D. (cm)	Lead Backing Ring Opening Angle (°)	Lead Backing Ring Length (cm)
C1	0	6.00	15	5.1
S1	40	5.90	15	5.1
S2	80	5.70	15	5.1
S3	120	5.50	15	5.1
S4	150	5.34	15	5.1
S5	175	5.32	15	5.1
C2	200	5.00	4.9	10.2

Table 3.1: Position and inner diameters of the ^{6}LiF scraper rings in the seven collimator components. The dimensions of the thick lead rings behind the scrapers are also shown. The first six lead rings are identical.

Material	Density (g/cm^2)	Composition
lithium fluoride	2.6	93% ^{6}Li
lithium glass	2.4	Li_2O (93% ^{6}Li), 60% SiO_2, 16%PbO, and 8% $Al0_3$ by weight
lead absorber	11.4	Pb
aluminum beam pipe	2.7	Al
^{58}Ni beam guide	8.9	^{58}Ni

Table 3.2: Composition of materials used in the emiT collimators. These are the numbers used in the performance simulation.

region [44]. Results were compared for different materials under consideration for the scraper rings and the thick lead rings. Interactions of each neutron with a material were taken as a sum of probabilities of elastic scattering, radiative capture (n,γ), and capture with alpha emission (n,α) taken from reference [45]. The simulation predicted 53% transmission through the collimator, 47% radiative capture (47% (n,α) and 0.0028% (n,γ)) and 0.0004% neutron escape from the apparatus, mostly through the lead rings. The resultant beam contained 99% of all neutrons within a 6 cm diameter. Tables 3.2 and 3.3 describe the compositions of the materials used and the contributions of each material to radiative capture.

The total flux of gamma-rays at the center of the detector region was predicted to be 1.73 γ/cm^2 for each 10^{10} neutrons. The (n,α) capture on ^{6}Li produces a triton which can produce a fast neutron. The estimated fast neutron flux from this reaction was 2.84

Material	(n,γ)Contribution (%)
^{6}Li	73.82
F	18.34
Al	1.74
Si	1.91
O	0.00
^{58}Ni	1.01
Pb	3.13

Table 3.3: Contributions of various collimator materials to the radiative neutron capture.

n_{fast}/cm^2 for each 10^{10} neutrons.

The final collimator sits 12 cm from the upstream edge of the beta detectors. Past the detection region the vacuum chamber diameter increases to 40.6 cm so that the walls are further out than can be reached by the most divergent of neutrons in the beam. The radius (r_{div}) of the most divergent neutrons at a given distance from the collimators is defined by the greatest angle at which they can pass through collimators C1 and C2. This radius is

$$r_{div}(z) = \frac{r_{C1} + r_{C2}}{z_{C2} - z_{C1}}[z - (z_{C2} - z_{C1})] + r_{C2} \tag{3.7}$$

where r_{C1}, r_{C2} and z_{C1}, z_{C2} are the radii and positions of the two collimators. The vacuum chamber ends 5.7 meters from C1, indicating r_{div}=12.5 cm. The beam is stopped in a 63 mm thick plate of ^{6}Li-glass. A 1 mm diameter pinhole at the center of the beamstop allows less than 1% of the beam to pass through a silicon window into a fission chamber detector which continuously monitors the flux. Any neutrons passing completely through the fission chamber are subsequently absorbed by a piece of borated plastic.

The beam is assembled sectionally from the supermirror to the beam stop. Each section has adapter flanges for each end with wire cross-hairs that define the axis of the tube. These are aligned by sighting them with a theodolyte aligned to the axis of the deflected polarized beam. This theodolyte alignment is precise to within the 0.13 mm wire diameter.

3.4 Spin Flip and Spin Transport

The spin flipper has two sheets of current, each made by laying 25 gauge Formvar-coated aluminum wires against each other in a plane. The two planes are placed nearly

touching, both vertical with the wires running horizontally. A constant current is maintained in one of the planes, while the current in the other plane is switched between directions so that it is either parallel or antiparallel to the other current. When the currents are parallel, the magnetic fields on each side of the two sheets have the opposite orientation ($B\hat{y}$ and $-B\hat{y}$). As the neutrons pass through the two sheets of current, they are unable to follow the sudden change in the field. The condition for adiabaticity requires that the rate of change in the field direction be slow compared to the Larmour frequency $\omega_L = eB/mc$.

$$d\hat{B}/dt = v_n d\hat{B}/dx << \omega_L \tag{3.8}$$

For the spin flipper the opposite is true: $v_n d\hat{B}/dx >> \omega_L$. Downstream of the flipper, the polarization is rotated and held to the beam axis by a series of solenoids and coils whose dimensions are described in table 3.4. These create a guide field of 1 gauss that increases to 5 gauss in the detector region. In order for the neutrons to follow the guide field as it is rotated to the horizontal, condition 3.8 must be satisfied at all times. For a neutron in a 1 gauss field, the Larmour precession frequency is 10,000 rad/sec. Since the cold neutrons travel at 1000 m/s, the field changes direction at less than 3°/cm. The evolution of the neutron spin during flight is illustrated in figure 3.4

Component	Diameter (cm)	Length (cm)
solenoid S2	11	71
loop L1	14	2.5
loop L2	20	2.5
solenoid S3	20	90
loop L3	20	2.5
loop L4	30	.05
solenoids S4-5	40	50
loop L5	60	2.5
guides (loops) GF1-8	87	2.5

Table 3.4: Magnetics used in spin transport.

The eight large loops of current that surround the detector are aligned with the theodolyte. A finer alignment is done using an alternating current technique whereby the contributions to each additional coil are isolated from other magnetic fields by locking on the AC frequency. The detector region is also surrounded by a system of "sine" coils, a series of 12 line currents (parallel to beam) and arcs as shown in figure 3.12. This configuration

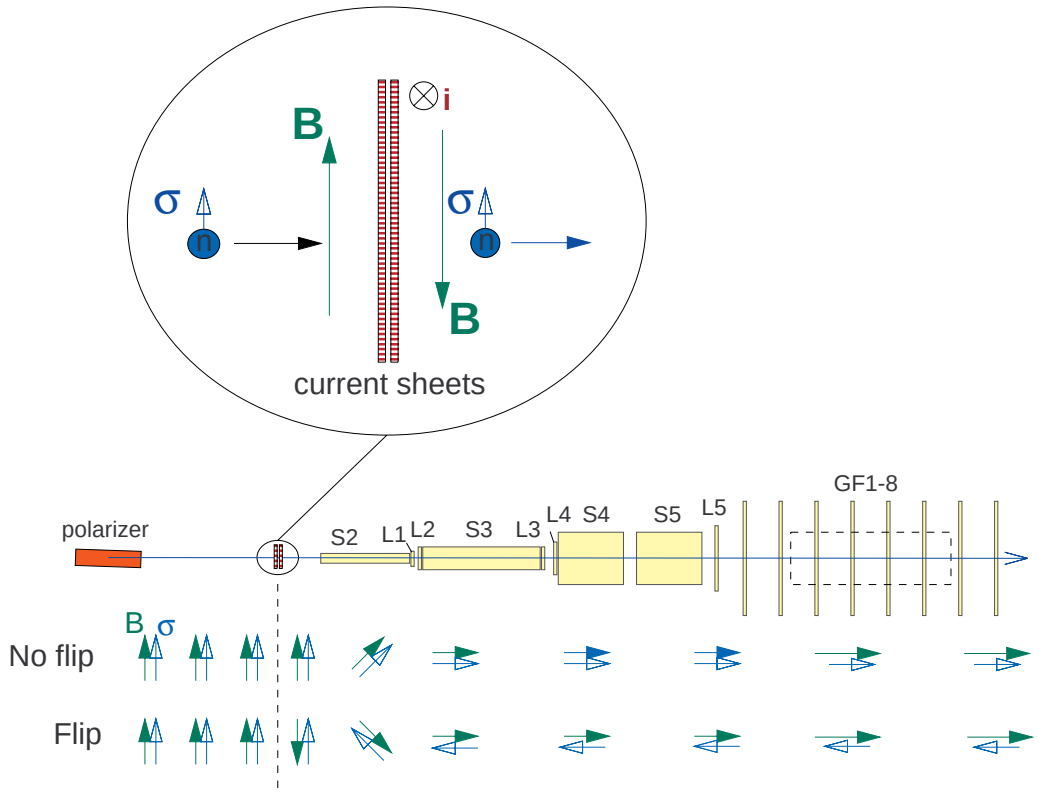

Figure 3.10: Two sheets of current-carrying wires create a magnetic field of opposite orientation on each side. The field orientation changes so rapidly that a neutron passing through the current sheets cannot follow the field flip, and thus the polarization, the relative orientation of neutron and field, is reversed. Downstream the field direction and polarization are rotated adiabatically to the beam axis.

is capable of producing any orientation of constant field if the current provided to each long segment is proportional to the sine of its relative azimuthal angle with respect to the azimuthal angle of the desired field. The current in the j-th segment is given by

$$I_j = B_0 C \sin(\phi_B + \phi_j). \tag{3.9}$$

This arrangement was used to cancel out the earth's magnetic field in the detector region. At the CNRF, the detector sat in a region where the earth's field (approximately 0.5 gauss) pointed downstream and downwards at a 40° inclination to the horizontal. The ambient field also had a large gradient, the field magnitude differing by 10% between the two ends of the detector region. A rectangular array of coils above and below the sine coils canceled this

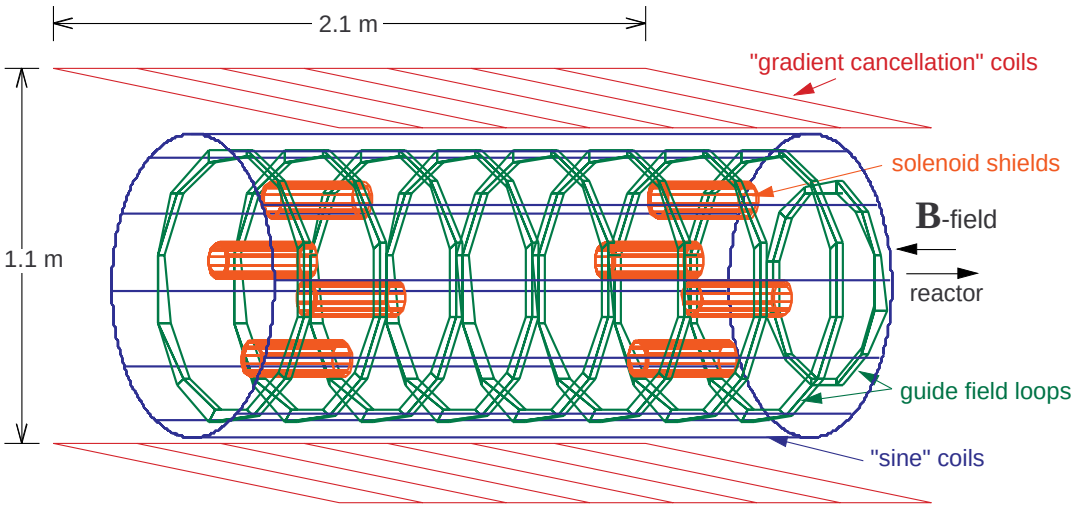

Figure 3.11: Four types of magnetic coil arrangements were used in the detector region. The sine and gradient coils cancel the slightly distorted earth's field in this region. Eight loops produce the 5 gauss field that guides the neutrons. Finally, eight pairs of coaxial solenoids cancel the guide field around the phototubes. The components are detailed in figure 3.12.

gradient. The assembly of magnetics near the detector is shown in figure 3.11. Once the gradient, sine, and guide coils were tuned, the profile of the field was mapped with a triple-axis Hall probe and a flux-gate magnetometer. The guide field loops' construction allowed them to be removed from the clamps and slid down to the extremities of the support frame, providing access to the detector for placement, removal, and maintenance. "Kinematic" mounts determine the position of the coils and maintain the integrity of the field upon removal and replacement of the coils. The coils and detector are mounted upon separate rails so each can be aligned independently. To prevent drift in the field, the currents are controlled via a feedback system which measures the current on 2 Ω resistors which are water-cooled to reduce temperature-dependent drifts in resistance. A test using the sine coils showed a stability of better than 1% over 5 hours.

The field profile is an important detail when considering certain systematic uncertainties. Examining possible effects led us to require field alignment of $< 1°$. Stricter limits were placed on local distortions of the guide field, restricting them to .5 mgauss, a local field angle of 1 mrad. Only non-permeable materials were used near the detectors.

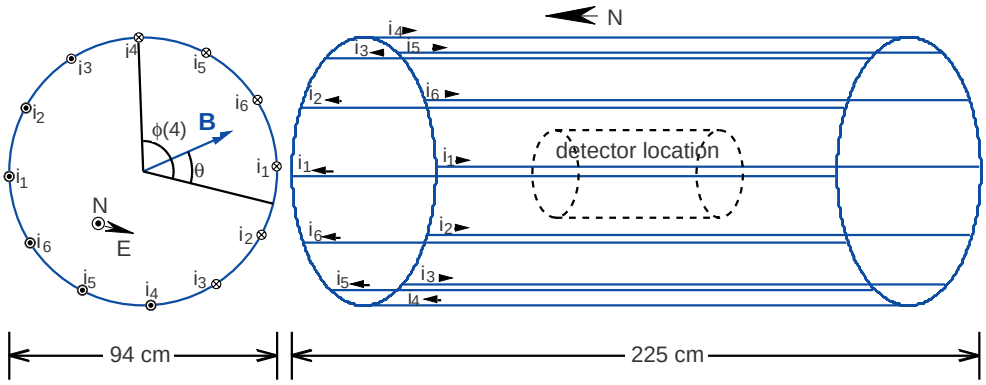

"Sine" coils cancel constant ambient field.

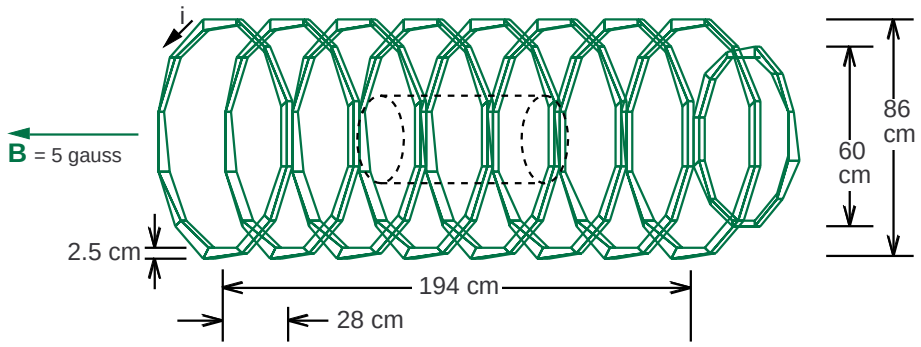

Guide field coils give longitudinal field.

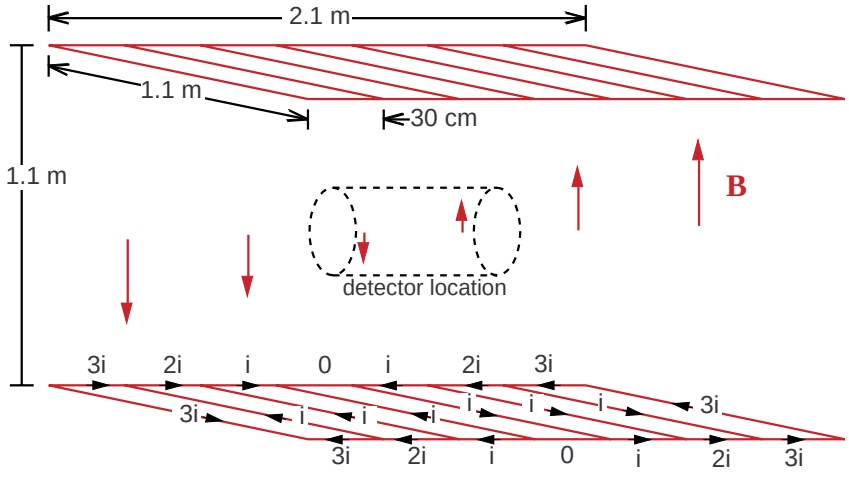

Gradient coils cancel ambient field linear gradient.

Figure 3.12: Details of the magnetic components in the detector region.

All steel components were fabricated with 304 or 316 stainless steel. A permeability meter was used to confirm the steel's permeability of less than $.01\mu_0$. The one major exception to the permeability limitations was the use of high permeability metal shields to protect the beta detectors' phototubes from the guide field. The phototubes show marked decreases in performance in magnetic fields at or above 0.5 gauss and can be effectively protected by surrounding the phototubes with cylinders of high permeability "mu-metal." These mu-metal cylinders distort the guide field by 10 mrad at the beam location. This challenge was dealt with by the use of active magnetic shielding. The effect of the mu-metal on the field was reduced by using active magnetic shielding to counter the field at the mu-metal/phototube location. Each phototube was surrounded by a set of coaxial solenoids of equal length but differing diameters, one inside the other as shown in figure 3.13. The windings of the coils are opposite and thus the fields inside are opposite in direction and differing in strength. The field produced at the center of the solenoid pair is equal and opposite to the guide field, canceling it at the position of the phototube. This renders the mu-metal largely redundant since it magnetizes only to reject what field the solenoids fail to cancel. The solenoids themselves create some transverse fields at the beam location but these are much smaller than the contribution from the mu-metal alone. For the proper current ratio, the dipole moments of the two solenoids are equal and opposite, so the field outside the pair is much smaller than that of a single solenoid (or mu-metal cylinder) with the same inner field. The necessary current ratio is equal to the ratio of the cross-sectional areas of the solenoids,

$$\frac{I_{inner}}{I_{outer}} = \frac{\pi r_{outer}^2}{\pi r_{inner}^2} = \frac{\pi(5.74cm)^2}{\pi(5.11cm)^2} = 1.26. \tag{3.10}$$

The total transverse field produced at the beam location by the active shields and mu-metal is less than 2.5 mgauss (0.5 mrad).

3.5 Beta Detectors

A diagram of an emiT beta detector is shown in figure 3.14. Plastic scintillator is used for beta detection, the rectangular scintillators connected to light guides and phototubes at each end. When an energetic particle passes through a scintillator, it produces light with a characteristic spectrum, the number of photons released depending on the energy value and the type of particle. The light is then channelled to photomultiplier tubes, which convert the photon pulse into an electrical one.

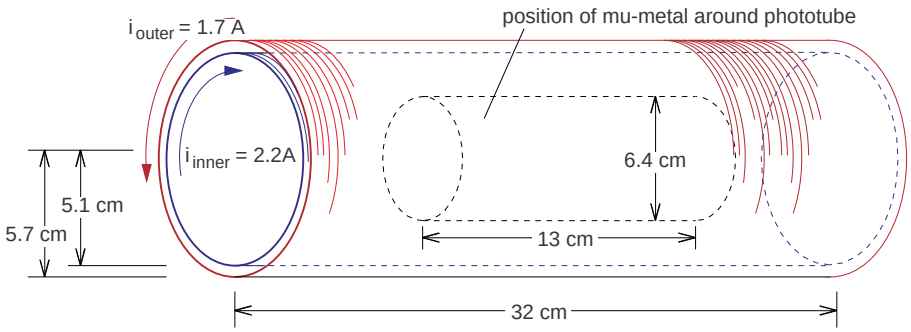

Figure 3.13: The magnetic shields for the phototubes consist of two solenoids wound on coaxial aluminum cylinders and carrying differing currents in opposite directions. The geometry allows a net field inside even when the dipole fields of the two magnets cancel outside.

The scintillators were cast commercially to 6.35 mm thickness, cut and then diamond-milled to 8.4 cm width. At Berkeley they were milled to 50 cm length and the ends were polished prior to gluing. These dimensions were chosen to give the greatest acceptance, position, and energy resolution for decay electrons with the least sensitivity to background. Higher acceptance can be achieved with a longer detector, but attenuation and light-loss decrease the resolution and the efficiency for detection of low-energy events. The 6.35 mm thickness is just enough to fully stop the most energetic of the 0-782 keV neutron decay electrons. A thicker scintillator gives less light-loss (since there are fewer bounces at the surface) and therefore better resolution and sensitivity, but has an increased response to background gamma-rays.

Light produced in the plastic scintillator emanates from the interaction region roughly isotropically, and a certain fraction is retained by the process of total internal reflection at the plastic/vacuum interface. The plastic, Bicron organic BC408 [46], has an index of refraction of 1.58, and was highly polished, leading to an initial reflection fraction of 37%. As the trapped light bounces down to either end, additional losses are incurred by imperfections in the polishing, and by reabsorption by the scintillator, and later by the light-guide. BC408 was chosen for it's fast response and for its resistance to deterioration in a low pressure environment. Figure 3.15 shows the typical spectral response of BC408 scintillator.

The light guides are made of lucite acrylic, which has an index of refraction of 1.51.

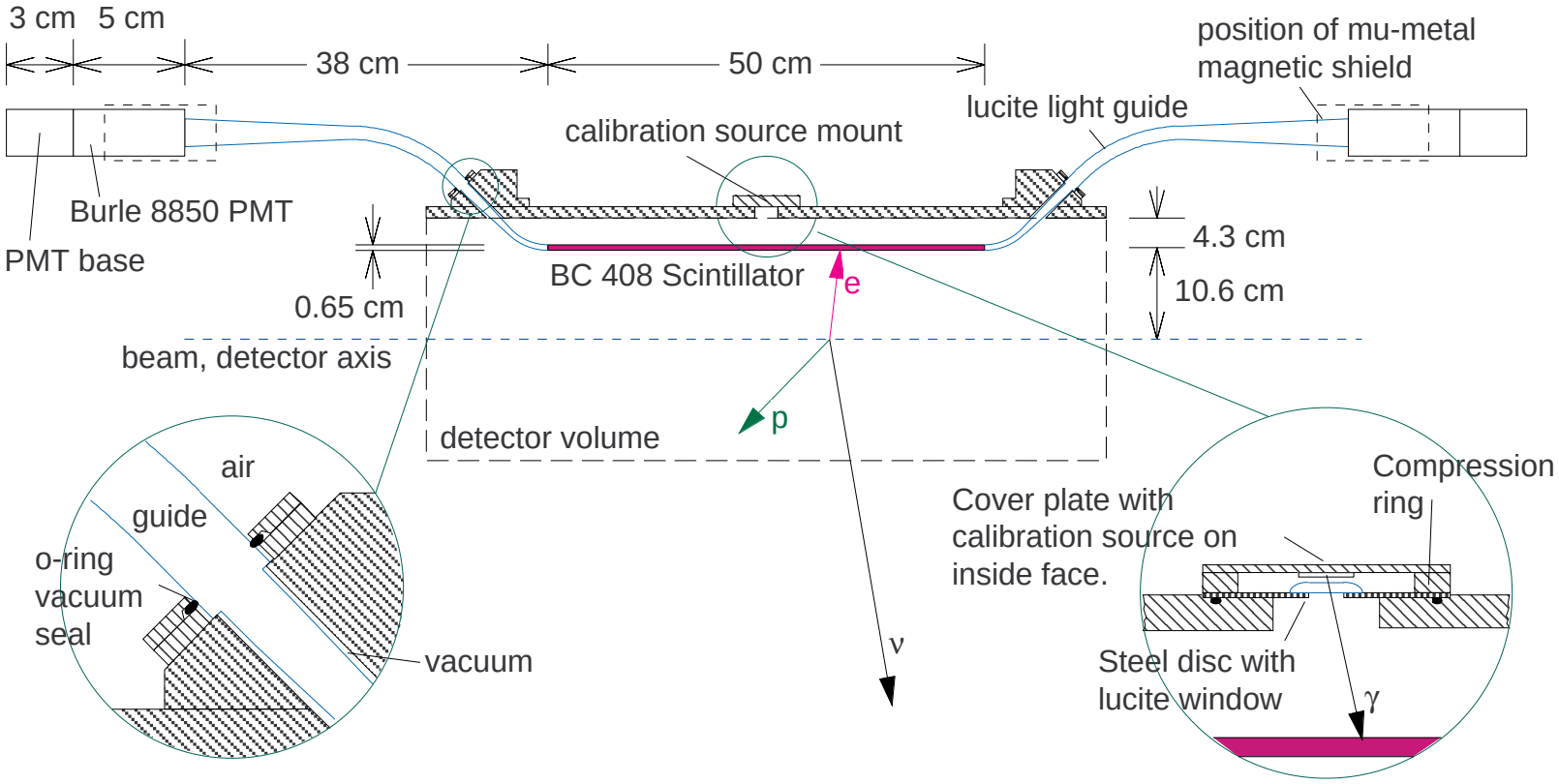

Figure 3.14: Side view of a beta detector segment.

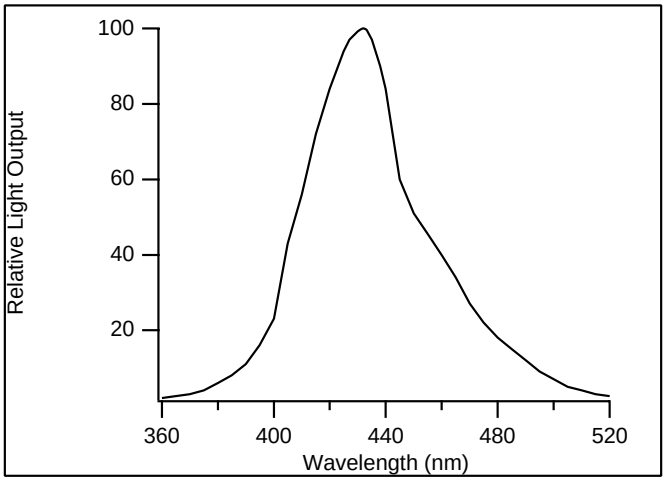

Figure 3.15: The measured response of BC408 scintillator [46].

This lucite, an ultrapure sample from the Sudbury Neutrino Observatory, has excellent transmission over the wavelength range of the scintillation light. (Most commercial lucite has additives to absorb ultraviolet.)

The guides are glued to the rectangular ends of the scintillator with NE 581 optical epoxy, which has an index of refraction of 1.6. The guides make two bends to bring the scintillation light out of the vacuum system, channeling the light onto the circular face of the phototube. The cross-sectional area of the guides does not decrease as they change shape, and the bends are gradual enough to satisfy adiabaticity conditions, minimizing the light-loss.

The phototube chosen for the beta segments was the Burle 8850, whose characteristics are listed in table 3.5. The 8850 is a twelve-stage tube with a bialkali cathode, designed to have a large voltage at the first dynode for superior single photoelectron resolution. Photocathode response and gain for each tube were tested before detector assembly by measuring the spectrum of single photoelectrons from spontaneous emission. These tests were consistent with the specified photocathode efficiency of 20-30% over the wavelength range. The effectiveness of the magnetic shielding was also tested. When an unshielded tube was placed in a 5 gauss field, the gain of the single photoelectron peak was reduced by a factor of two . The peak was observed at its original gain when a mu-metal cylinder was placed around the tube with one edge of the cylinder extending 2 cm past the cathode.

diameter	2 inches
length	5 inches
cathode material	bialkali (K-Cs-Sb)
cathode useful diameter	1.8 inches
window material	pyrex
window index of refraction	1.47
first dynode material	GaP
dynode 2-12 material	BeO
current amplification	1.5×10^7 (typ.)
10-90% pulse rise time	2.1 ns
pulse transit time	37 ns
average anode current for maximum stability	$< 1\ \mu$A
maximum anode current for pulse linearity	< 25 mA
cathode response	20-25% from 325-600 nm
peak of response	380 nm

Table 3.5: Burle 8850 phototube characteristics.

The ability of the mu-metal to shield the tube was seen to be very sensitive to positioning: If the cathode protrudes from the cylinder as little as 0.5 cm, the gain is reduced by 40%.

3.5.1 Fabrication

A single prototype beta detector was built to test the fabrication and operation of the detector. A modified procedure was used to to fabricate the 4 detectors used in the experiment. During fabrication the detector is built onto a plate that connects it to the vacuum chamber. As the light-guides bend outward and through openings in this plate, an o-ring around each guide is partly compressed between two metal plates, pushing it against the plastic to make a seal. As each was completed, the vacuum seals and glue-joint integrity were tested before continuation of the fabrication procedure. The main fabrication steps were: (1) Polishing and preparation of light guides. (2) Preparation of scintillator. (3) Cleaning and assembly of vacuum parts (hardware, o-rings, and inner light guides.) (4) Leak-checking of vacuum seal. (5) Gluing of scintillator to inner light guides. (6) Re-checking of vacuum seals. (7) Gluing of inner light guides to outer guides. (8) Gluing of phototubes to outer guides. (9) Completion of outer light seal. These procedures are

detailed in Appendix A.

3.5.2 Beta Detector Electronics

The phototubes were powered with an electronic base design (shown in figure 3.16) recommended by Burle for the 8850. The cathode was held at negative high voltage, and field was delivered to each dynode via a simple voltage divider chain. The 8850 demonstrates superior response for single photoelectrons when there is more than 500 V between the cathode and first dynode. The base delivers 25% of the applied voltage to this first stage, requiring a total voltage of greater than than 2kV. In the first set of bases built, the last 8 dynodes received the same portion of the voltage (a "linear" divider), but the phototube response was nonlinear (see section 3.5.4) at anode currents of over 25 mA (corresponding to about 50 photoelectrons). This was due to the "space-charge effect", whereby the large current of electrons between the last dynodes distorts the field between them, diminishing their gain and focusing efficiency. This was remedied by modifying all the bases to have a "tapered" divider chain. Lower voltages on the last four dynodes reduced the fractional loss of gain and focusing, improving the linearity. Capacitors over the last four stages of the divider chain provide enough transient current for large signals. Two outputs were constructed for the anode signal and impedance matched to 50 Ω cable. During the run, one output on each base was terminated with 50 Ω. The pulse produced at the anode was a negative signal with a typical 2-3 ns risetime. For a single photoelectron at the operating voltages used (average voltage: 2400 V), the pulse height was 15-30 mV with a 15 ns fall time.

Operating voltages were chosen to match the combined gain of phototubes and light guides on each side. A collimated Sr-90 source was placed at the center of the scintillator and the voltages were adjusted so that the average charge from each tube was the same for each event. The voltage for the phototubes was supplied by a LeCroy 4032A 3NIP, which is capable of supplying up to 3300 V each from 32 separate channels. The 4032A maintained the voltages to within a few volts of the settings by monitoring the voltages constantly. The supply limits the rate of voltage increases to 500V/s and each channel would trip if the current reached a limiting value of 3±0.3 mA. Each channel in the 4032A will also shut off if the readout voltage falls 64 V below the setting. The bases produced 2.5 watts each and were cooled by forced airflow between the bases and the active magnetic

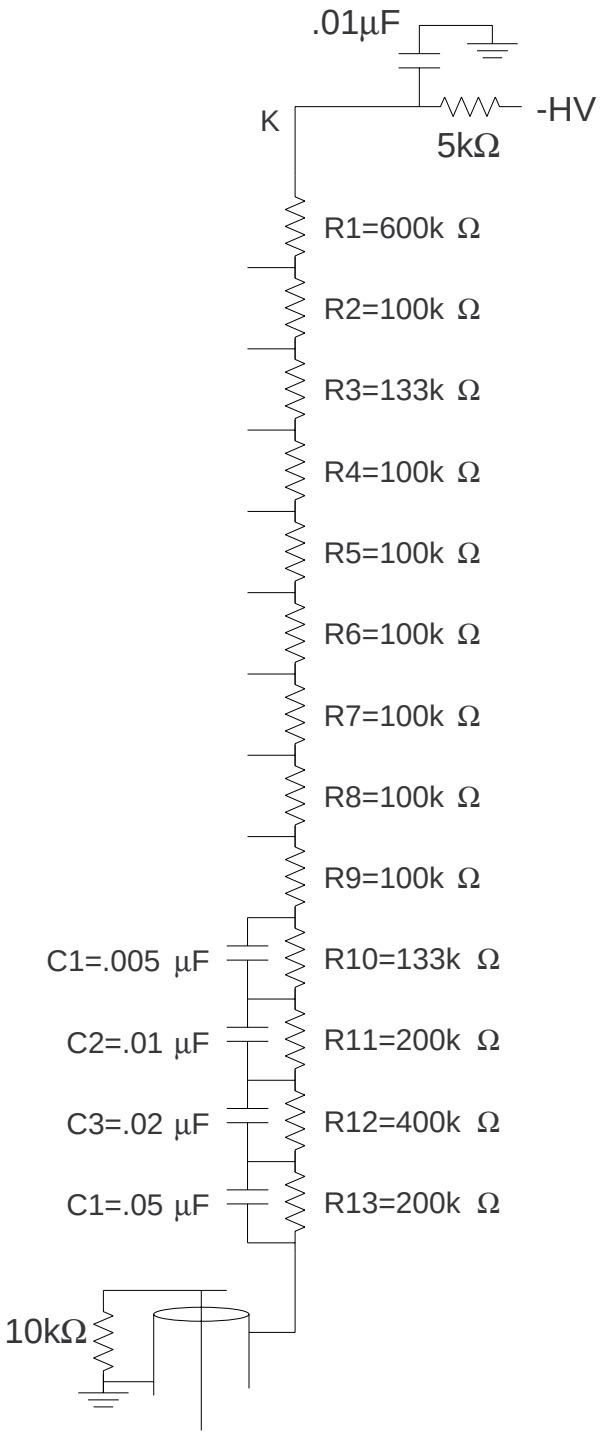

Figure 3.16: Schematic of the final version of the emiT phototube base voltage divider chain.

shields surrounding them. During the first few weeks of the run, a few of the bases began to give intermittent signals, often appearing to be dead for several hours and then reviving, although there was always one operational base per detector. This was traced to a structural problem in the socket attachment and all of the bases were repaired and reinforced before the second cycle.

Signals traveled 50 feet to a rack of commercial electronics, including level-crossing discriminators that detect signals above a potentiometer-controlled threshold. The discriminator output logic pulses were used to start and stop time-to-digital converters (TDCs) and to gated charge-integrating analog-to-digital converters (ADCs). Details of the data acquisition will be discussed in section 3.8.

3.5.3 Beta Detector Response

A particle of incident energy E_i traversing the scintillator will deposit some portion E_d of its energy. An electron of less than the 800 keV stopping power of the scintillator will deposit its full energy ($E_d = E_i$). A gamma-ray will often pass through the scintillator without interacting. The most likely gamma-ray interaction is a single Compton scattering with an electron whereby the energy deposited by the photon depends on the scattering angle θ through which it is deflected. The maximum energy is imparted to the recoil electron for backscattering of the photon ($\theta = \pi$), giving a total electron energy of

$$E_e = \frac{p_i^2 c^2}{m_e c^2/2 + p_i c} + m_e c^2, \tag{3.11}$$

where p_i is the momentum of the incident photon, and m_e is the mass of the electron. Electrons are produced in a continuous spectrum from zero to this maximum value and the measured spectrum will also depend on the geometry of the scintillator due to the effects of finite stopping power and the distribution of locations of the scattering events. Very energetic charged ("minimum-ionizing") particles will deposit nearly the same amount of energy for a given detector thickness, regardless of the exact incident energy E_i. The spectrum of cosmic muons has a Landau shape with a most probable value of 1.42 MeV for 6.35 mm of scintillator.

The total charge produced in each phototube is a function of the deposited energy E_d, the location of the particle detection, and the characteristics of the detector.

$$Q = egf(E_d)e^{(L/2-x)/\lambda_{eff}} \tag{3.12}$$

The function $f(E_d)$ is the number of photons produced upon deposition of E_d, and is simply $c_s E_d$ if the response is linear. c_s is the number of photons produced per unit energy deposited, typically 10 photons per eV.

The total gain

$$g = g_T \epsilon_q \alpha f_1 f_2 f_3 e^{-L_g/\lambda_g} \tag{3.13}$$

includes the gain in the tube g_T (approximately 10^7 electrons per photoelectron) and the quantum efficiency ϵ_q of the cathode (20-25% of photon make a photoelectron). It also includes the transmission f_i in each of the three glue joints (see figure 3.17), the fraction initially reflected internally within the scintillator (α=0.37), and the attenuation e^{-L_g/λ_g} in

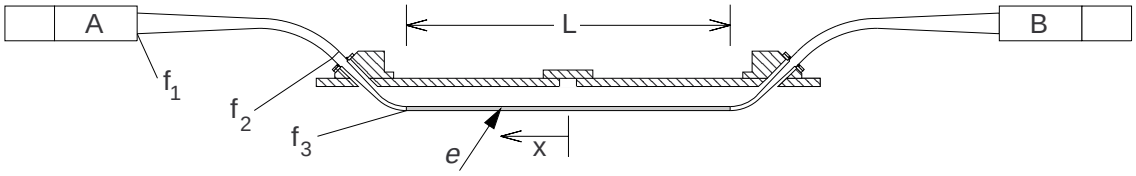

Figure 3.17: Some of the parameters used in characterizing the beta detectors. The location x of the particle event is measured from the center of the detector. The PMTs on the two sides of the detector are designated PMT A and PMT B. f_1, f_2, and f_3 are the light transmission factors at the three glue joints on one side of the detector.

the light-guides of length $L_g \approx 50$ cm. The attenuation in the scintillator depends on the position x of the event from the center of the scintillator of length L=50 cm. The effective attenuation length λ_{eff} is a combination of attenuation by absorption in the scintillator (the bulk attenuation length quoted for BC408 is $\lambda \approx$3 m) and loss at the surface with each bounce. For a scintillator of 6 mm thickness in which the photons travel at an average angle of about 30° to the surface, the photons bounce once for every centimeter of distance toward the ends. The probability for internal reflection P_r at each bounce is very close to unity, improving with surface quality and somewhat with surface treatments such as reflection coatings. The emiT scintillators have no coatings, but the aluminized mylar has a small probability of reflecting photons that escape. Since the photon bounces between parallel surfaces rather than traveling in a straight line, the path length is greater than the x-direction travel by a factor of $1/\cos 30°$. This gives

$$e^{(L/2-x)/\lambda_{eff}} = e^{-(L/2-x)/(\lambda \cos 30°)} P_r^{((L/2-x)/(1\ \mathrm{cm})}, \tag{3.14}$$

$$1/\lambda_{eff} = 1/(\lambda \cos 30°) - \ln P_r/(1\ \mathrm{cm}). \tag{3.15}$$

The product $\alpha c_s f_1 f_2 f_3 e^{-L_g/\lambda_g}$ is the light-collection efficiency. The product of the light-collection efficiency and the quantum efficiency (which is equal to g/g_T) is the quantity that primarily limits the resolution of this detector, since the limiting statistical resolution depends on the number of photoelectrons N_{pe} produced at the photocathode.

In addition to characterization and calibration of the beta detector, it is necessary to choose a trigger with the least sensitivity to the event location and the best timing and energy resolution, which are important to the coincidence detection efficiency. If the response of the two phototubes is linear, but with different gains, the charges they produce are

$$Q_A = g_A E_0 e^{(L/2-x)/\lambda_{eff}}, \quad Q_B = g_B E_0 e^{(L/2+x)/\lambda_{eff}}$$

In the gain-matching procedure described earlier, the operating voltages are chosen so that $g_A = g_B$. The geometric mean of these two charges is a measure of the energy that is insensitive to the position of the source.

$$Q_{mean} = \sqrt{Q_A Q_B} = E_0 \sqrt{g_A g_B e^{\{(L/2-x)+(L/2+x)\}/\lambda_{eff}}} = E_0 \sqrt{g_A g_B} e^{L/(2\lambda_{eff})} \qquad (3.16)$$

If the gains are matched and L/λ_{eff} is small, the linear sum is also independent of x and given by $Q_{sum} = Q_A + Q_B = 2E_0 g(1 + L/2\lambda_{eff})$. Since the linear sum is easily made electronically, this is used as the hardware trigger.

3.5.4 Testing of Beta Detectors

After their operating voltages were chosen, the four beta detectors were tested with various sources to study the gain and light-loss, energy and timing resolution, efficiency uniformity, and the effect of the hardware trigger. Sources used included Bi-207, Sn-113, Sr-90 , and a pulsed nitrogen laser.

Calibration and Efficiency

A 1 μCi bismuth-207 source was used for energy calibration and efficiency measurements. The 976 keV conversion electron peak (see figure 3.19) was the spectral feature studied. The 9% total conversion electron efficiency indicates that there are 10 gamma-rays for every electron emitted from that transition. In a scintillator spectrum, the electron peak is difficult to see over the broad compton spectrum even though the scintillator has better efficiency for beta particles than for gamma-rays. To increase the sensitivity to this

peak, the source was placed behind a thin (5.1 mm) scintillating disc as shown in figure 3.18 and triggered on events in this thin scintillator. The energy loss in the thin trigger was measured with a calibrated surface barrier detector to be 94 keV. A particle depositing energy in both this and the main detector was most likely an electron. This method greatly reduced the contribution from gamma-rays in the spectrum.

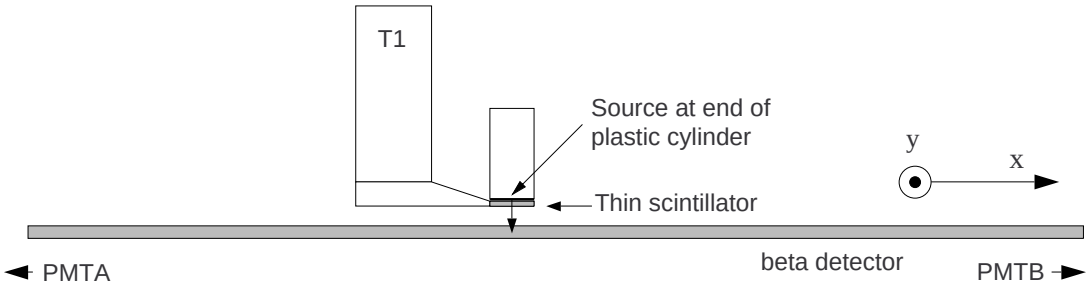

Figure 3.18: Bismuth source calibration setup. Particles pass through a thin trigger scintillator into the detector.

The whole source and trigger mechanism could be moved on two linear stages via a control rod extending outside of a large light tight box in which the detector was mounted. The extension of the rod indicated the x-position as the source was moved longitudinally down the detector, and the y-position could be read externally via a voltmeter connected to a linear potentiometer inside the box. In this way the entire surface of the detector could be scanned in a short period. The phototubes were allowed to warm up for several hours before each scan. Typical results of these scans are shown in figures 3.20 and 3.21.

A 10 μCi Sn-113 source (figure 3.19) was also used for scans and energy calibration, giving a peak at much lower energy , in the middle rather than above the neutron beta spectrum. The same scan apparatus was used with this source, although the superior conversion efficiency made the thin trigger scintillator unnecessary.

The bismuth and tin conversion electron peaks were fit with an automatic procedure that first smooths the data to find the position of the maximum. Cursors are set on the smoothed data at channels that are at 60% of the peak height on the low energy side and 10% of the peak height on the high energy side. A gaussian is then fit to the *unsmoothed* data between these cursors. The energies of the two spectral features were determined by generating a theoretical spectrum with the resolution of the beta detectors and the K and L conversion lines weighted by their relative abundances. The peak was then found with

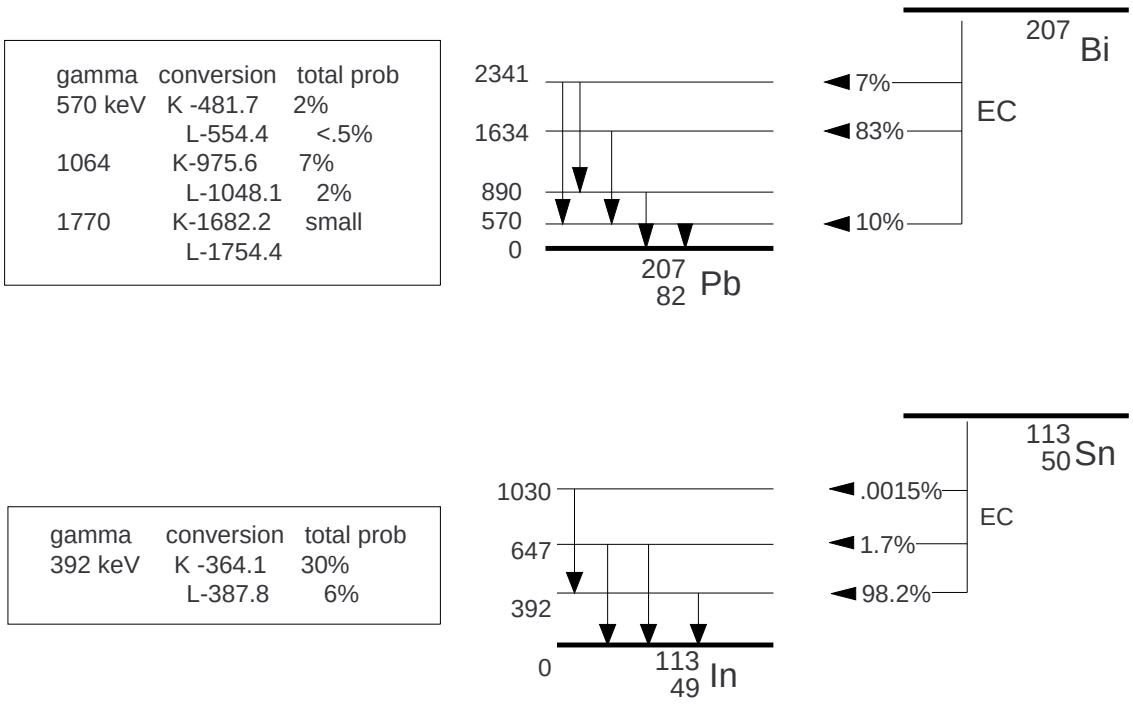

Figure 3.19: Bismuth-207 and tin-113 decay.

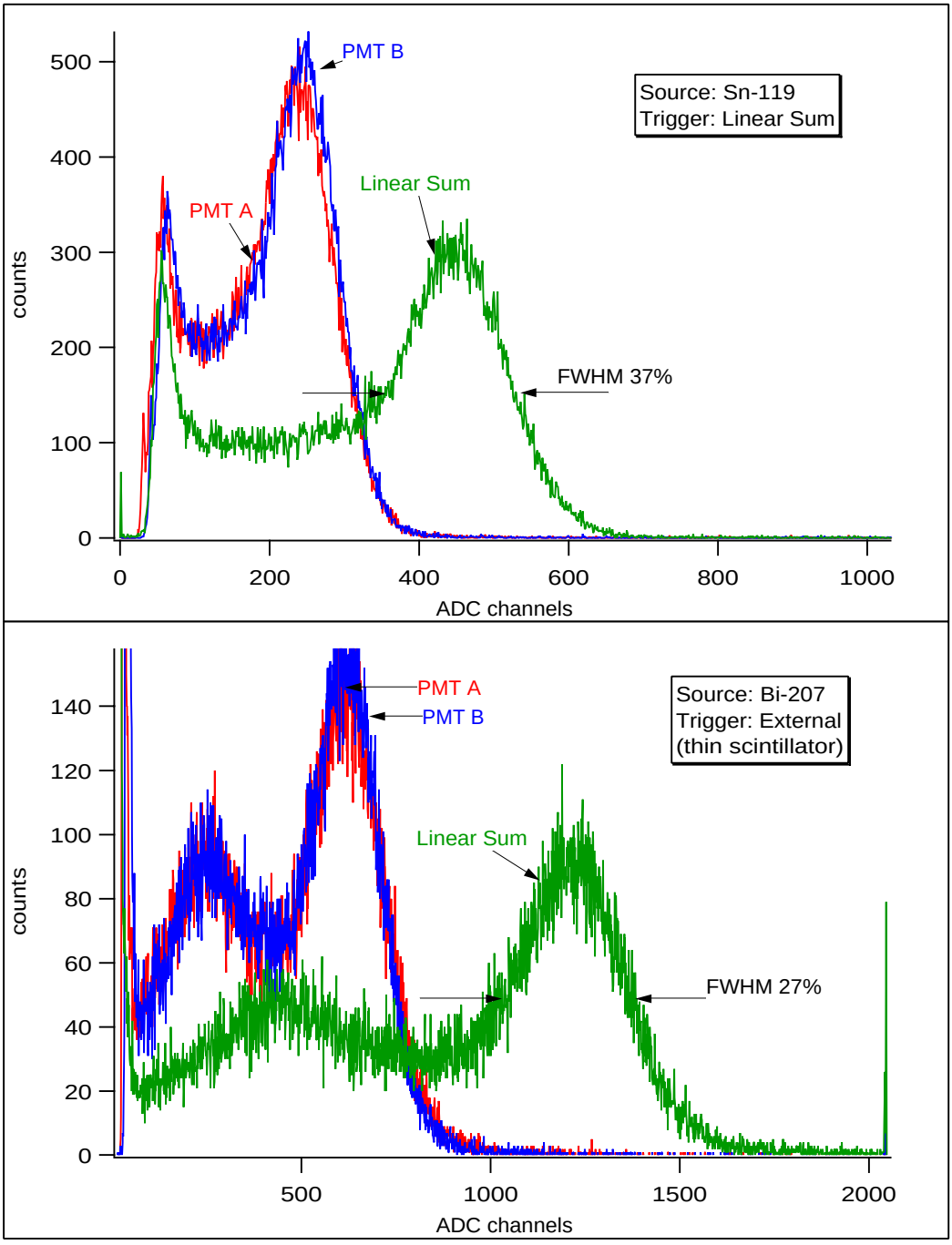

Figure 3.20: Sn-113 and Bi-207 spectra in beta detector E1 taken during initial calibration/characterization.

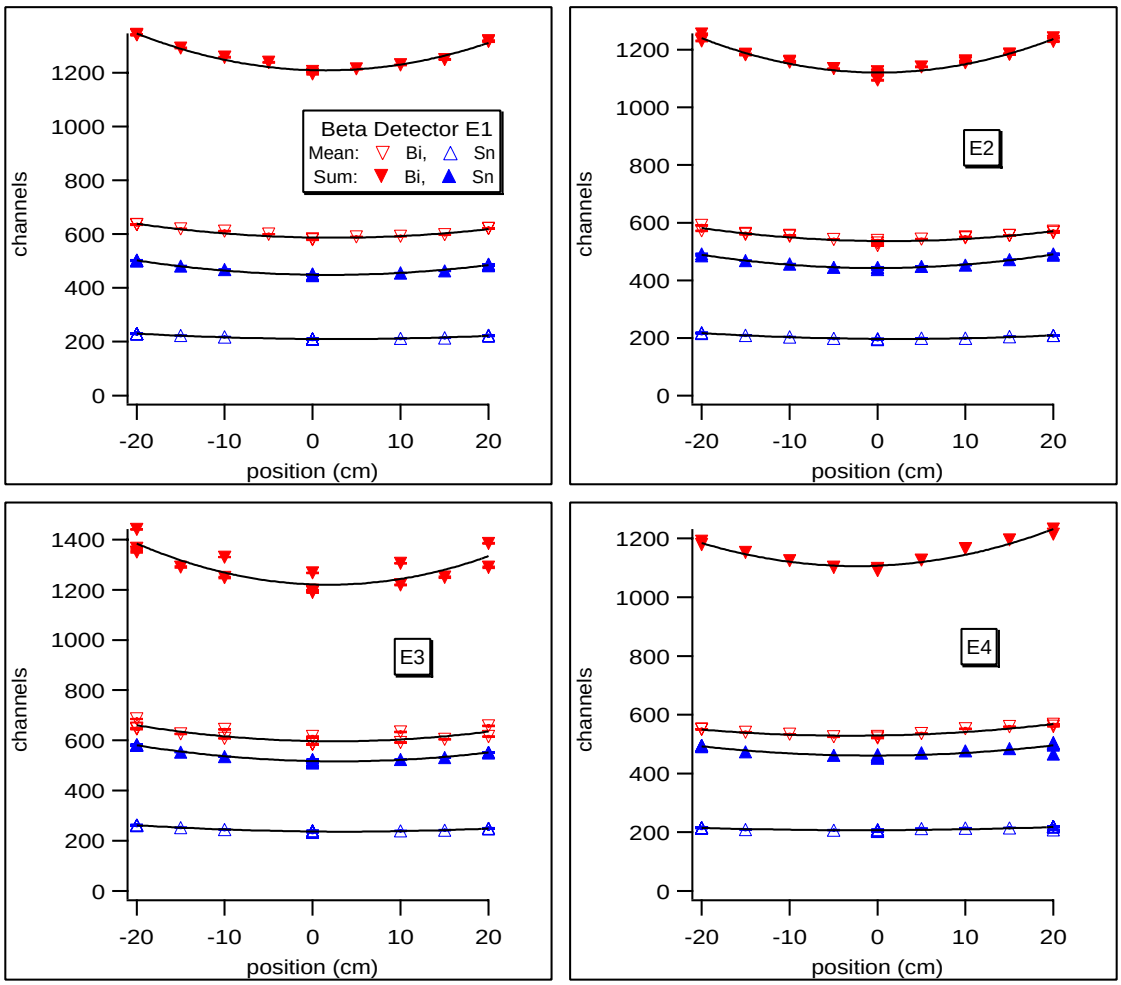

Figure 3.21: Charge (ADC channels) versus source position for beta detectors E1-E4.

the same fitting procedure used for the data. This gave 367 keV for the Sn-113 line, and 882 keV for the Bi-207 line (976 keV - 94 keV lost in the thin trigger scintillator). The calibrations obtained in this way are given in table 3.6.

From the conversion electron spectra, it was seen that the response was symmetric in x, showing less than a 5% difference in measured charge for $x \rightarrow -x$. The linear sum was chosen as the hardware trigger, with the level-crossing discriminator triggering below 50 keV. The curvature of the charge versus position curves of figure 3.21 are indicative of the finite attenuation lengths. The effect of using the linear sum is to create a slight curvature in the efficiency curve, the trigger biased slightly toward acceptance of events occurring near the ends of the scintillator. This is an effect of less than 10% from center to ends, creating an effective trigger of close to 50 keV in the center and 45 keV at the ends. However, the decay probability into these lower energies is small: For uniform illumination of the detector, the response function curvature would create a difference in count rate of less than 1%.

Beta Segment	Energy (keV from Q in channels)
E1	$E = 63 + 0.66(Q_A + Q_B)$
E2	$E = 31 + 0.73(Q_A + Q_B)$
E3	$E = -8 + 0.70(Q_A + Q_B)$
E4	$E = 4 + 0.77(Q_A + Q_B)$

Table 3.6: Calibration expressions for the emiT beta detectors. The sum $Q_A + Q_B$ of the signals from the two phototubes is taken in hardware.

The zero-energy offsets in the beta spectra (the pedestals, given in table 3.7) were found by triggering on an independent source. The resultant spikes at zero-energy were typically 5-10 channels in width. Fitting these features to a gaussian gave centroids stable to within 2 channels over time.

	Pedestals (channel)		
Beta Segment	Side A	Side B	Linear Sum
E1	32	42	16
E2	29	23	45
E3	46	41	43
E4	20	30	34

Table 3.7: Beta detector zero-energy pedestals.

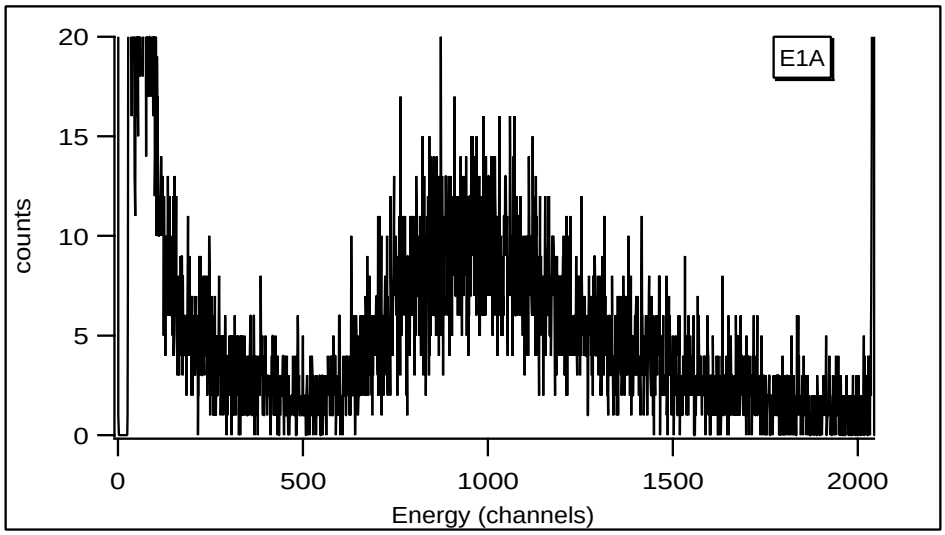

Figure 3.22: The minimum-ionizing Landau spectrum for cosmic muons, taken in coincidence with detector E3. The most probable energy at channel 960 is 1.4 MeV.

A measurement of the cosmic ray spectrum provides additional calibration verification. To reduce the background in the cosmic ray spectrum, the data acquisition was instructed to collect data from E1, but was triggered in the hardware by E3 directly above it. In this way, muons traveling vertically, depositing energy in both detectors, are the dominant contribution to the spectrum with some contamination from accidental coincidences. The data shown in figure 3.22 were taken in one hour. The most probable energy of the Landau spectrum is offscale for the linear sum, but for a single side it is seen to be collinear with the three other energy measurements (see figure 3.23.

A pulsed nitrogen laser was used for additional characterization, loading the beam into a single fiber of high-grade fused silica, coupled to 8 smaller fibers. One of these fibers was clamped to the same linear stage mechanism as the trigger detector in the Bi scanning setup. The fiber illuminated a 1 mm spot on the surface of the scintillator, and this spot was scanned across the detector face. The ultraviolet light from the laser is absorbed by the scintillator and downshifted to the scintillation wavelength. The beam intensity was attenuated by several neutral density filters before being loaded into the fiber. This put the peak of the laser spectrum in the range of the ADC. To reduce pickup in the phototubes of

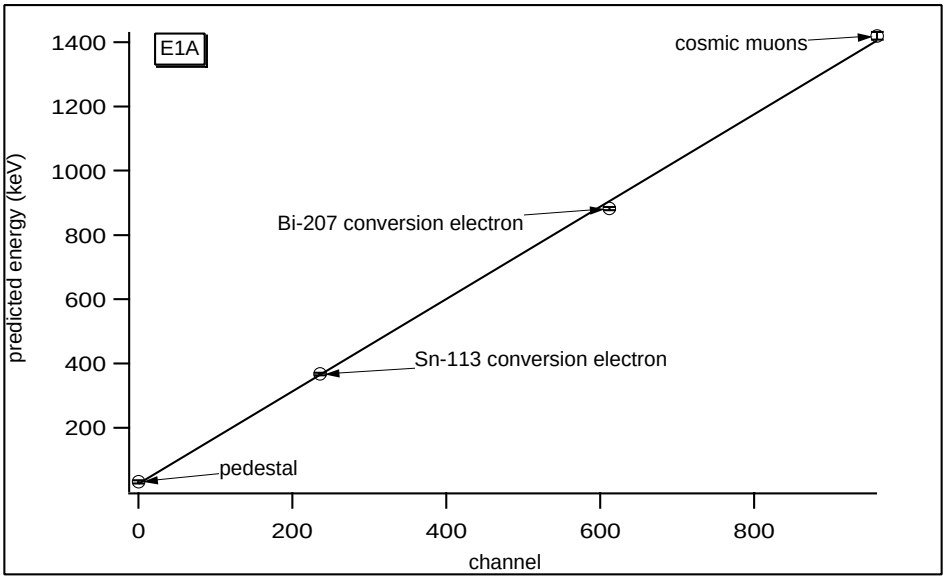

Figure 3.23: Four spectral features are used to verify the linearity of the beta detector's energy response.

radiofrequency noise from the laser, it was moved 2.5 m from the detector, and the bases and phototubes were shielded with aluminum foil wrappings.

The stability of the intensity in the laser pulses was measured by removing the neutral density filters and reducing the phototube voltage to put the peak on scale. In this configuration, the laser peak had a full width at half maximum (FWHM) of about 2%. To measure the light collection efficiency of the detector, the laser power was attenuated just enough to make a peak at the same energy as the bismuth conversion line. Looking at the charge from a single phototube, a gaussian fit of this peak gave σ=9% (21% FWHM). This width is primarily due to the statistics of the finite number of photoelectrons N_{pe}. If $\sigma = 1/\sqrt{N_{pe}}$, this implies that there are about 125 photoelectrons. The number of photons for a bismuth electron is about 8800 (880 keV $\times$ 10 photons/keV), half of which go toward the other phototube. If the quantum efficiency averages 23% for these photons, almost 550 photons reached the cathode, implying a light collection efficiency of about 12%, or 34% after the initial 67% loss at the first bounce. This is consistent with the scintillator attenuation measured as described below, combined with an effective attenuation of 1 m in

the lucite and less than 10% loss at each glue joint. The laser peak in the other phototube was 24% FWHM, implying a collection efficiency of 9%, indicative of the small differences in the attenuation, cathode efficiency, and quality of glue joints on that side of the detector.

Linearity

The bismuth scan measurements made before the modification of the phototube bases indicated a failure of linearity much greater than expected. One quantity extracted from the scan data is the effective attenuation length λ_{eff} of the scintillator. Initial studies showed that an exponential fit to $Q(x)$ gave different attenuation lengths when measured separately with the two phototubes. For example, the data in figure 3.24 indicate λ_{eff} of 122 cm and 179 cm on the two sides of one detector. It was discovered that the peak current of the signals exceeded maximum for linearity of the tube with the linear voltage divider chain built into the base. (A Burle spec sheet misprint had claimed linearity under these conditions.) The difference in measured attenuation lengths resulted from different levels of nonlinearity in the two tubes.

To further test the linearity, the scintillator was illuminated with light from two laser fibers. Light was collected for each beam alone (the other blocked by a beam stop) and for both beams shining simultaneously on the scintillator. The sum of the two independently-measured peak positions was seen to exceed that of the simultaneous measurement by close to 50% for large amounts of light, the discrepancy decreasing for lower light-levels. This is consistent with a space-charge effect [47], which was addressed with the tapered voltage divider of the final design. After this change, the linearity measured in the two-fiber tests was better than a few percent for light-levels corresponding to less than 800 keV energy deposition.

Timing

Each individual phototube pulse also triggers discriminators whose outputs are used to measure the relative time between the signals at each end. This value is an indicator of the location of the event in the scintillator. Keeping the source at a single location, the resolution of the timing signal was studied as a function of the discriminator thresholds. Figure 3.25 shows the time resolution improving for all energy ranges as the threshold is decreased, reaching a minimum for thresholds below 100 mV. This is consistent with the

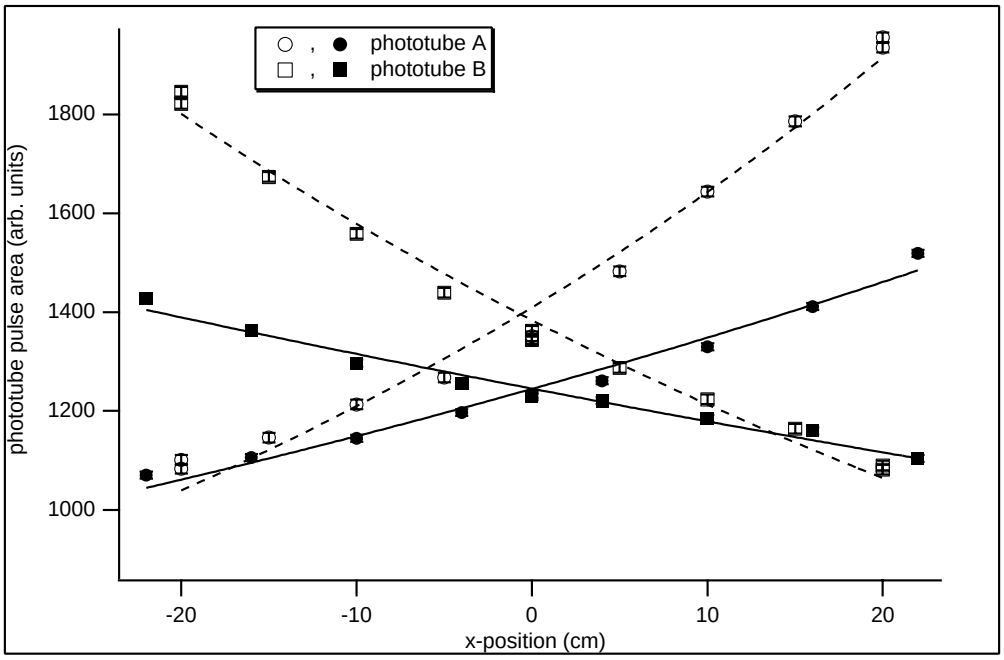

Figure 3.24: Bismuth source position scan of a detector showing fits to the peak as measured by the phototubes on each side. The exponential fits of the charge collected on each side versus the source location parametrize the loss of light as it travels from the detection site to the phototube. The exponent is the inverse of the effective attenuation length, λ_{eff}. With the old bases containing a linear divider chain (open symbols), it is apparent that λ_{eff} is quite different when measured from each side, giving values of 122 cm and 179 cm for sides A and B. With the new, tapered divider in the bases (solid symbols), there is closer agreement between sides A and B. This time the fits give λ_{eff} of 75 cm and 64 cm. These values are much less than the bulk λ of 3 m due to the angular travel and edge-loss effects. The values measured in the presence of the nonlinearity imply a greater λ_{eff} because the phototubes had lower gain at higher light-levels, which flattens out the attenuation curve.

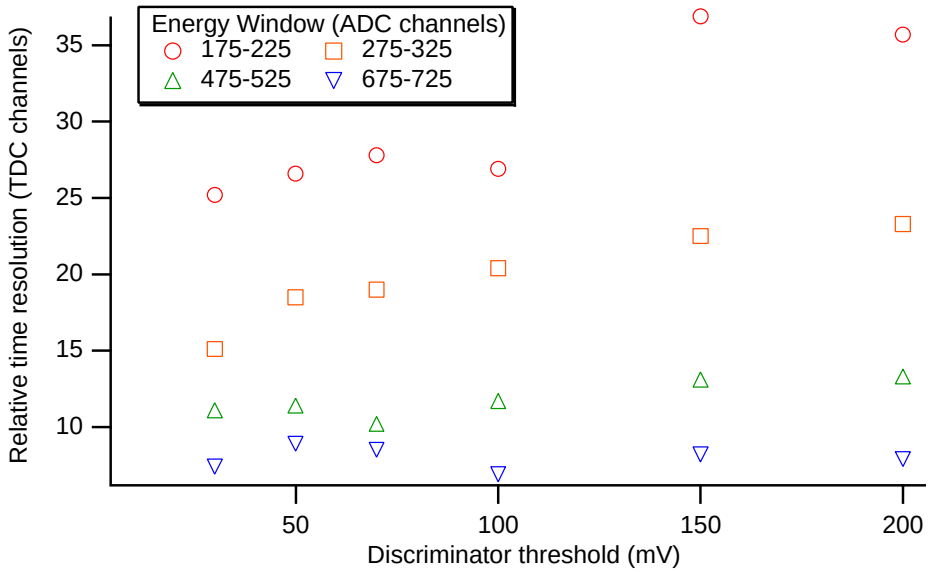

Figure 3.25: Graph of timing resolution versus the threshold set on the discriminators for the phototube signals. In this test (as in most of the run) the thresholds were the same for the two phototubes of the beta detector. The four curves are for different energy values. Higher energies experience less slewing and therefore have narrower timing peaks, but for all energies, the resolution is best for thresholds below 100 mV.

type of "slewing" effect often seen with level-crossing discriminators, an effect that is due to the finite rise-time of each pulse. During the run the gains were lower than in this test, but setting the phototube thresholds at 30 mV assured the best resolution.

3.6 Proton Detectors

3.6.1 PIN Diode Array

Each proton detector has an array of 16 PIN diodes arranged in two rows of 8. The diodes are enclosed within a high voltage electrode. Over each diode an open cylinder protrudes from the face of the electrode, shaping the field to focus and accelerate the protons onto the diode below. In this way, each 1.8 cm $\times$ 1.8 cm diode collects protons from an active region 4 cm $\times$ 4 cm. The assembly of the proton segment is shown in figure 3.27 The diodes, their supporting circuitry electronics, and the steel electrode are isolated from the rest of the apparatus on glass and ceramic supports. The electrode and its contents are held

at high negative voltage and connected to an external electronics rack, also at high voltage, which provides the power and signal processing for the diodes. A Bertan 225 supply provides the high voltage to the electrodes and power is delivered at high voltage to the electronics via a transformer connected to the Bertan. The Bertan is controlled via a General Purpose Interface Bus (GPIB) [48] with a Macintosh IIci. The HV software automatically ramped up the HV with a speed determined by the user, and could disable the system after sparks. The outer housing of each proton segment, which makes the vacuum seal with the detector chamber, also supports a frame that sits between the beam and the focusing electrode. The frame is strung with 80 3 mil (0.08 mm) gold-plated tungsten wires that define a plane of electrical ground that is 97% transmitting. Protons drift in a field-free region until they pass this plane, and then are accelerated by the high voltage and focused onto the nearest PIN below as shown in figure 3.26.

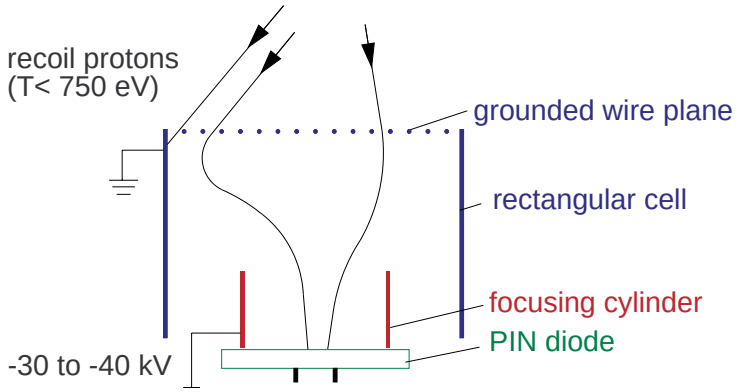

Figure 3.26: Geometry of the electrodes that accelerate and focus the protons onto a PIN diode.

The PINs are Hamamatsu S3204-06 diodes of 500 micron thickness, specified to have "dead-layers" of less than 20 μg/cm^2, approximately half the thickness of the dead-layers on the standard version of this PIN. The dead-layer of a diode is the inactive region on the face that a particle passes through before entering the active volume for detection. Protons are not highly penetrating and typically lose about 20 keV of energy in the 40 μg/cm^2 dead layer of PINs. A thinner dead-layer was necessary to reduce the proton energy loss so that the 30-40 keV signal from accelerated protons would be separated from the electronic background.

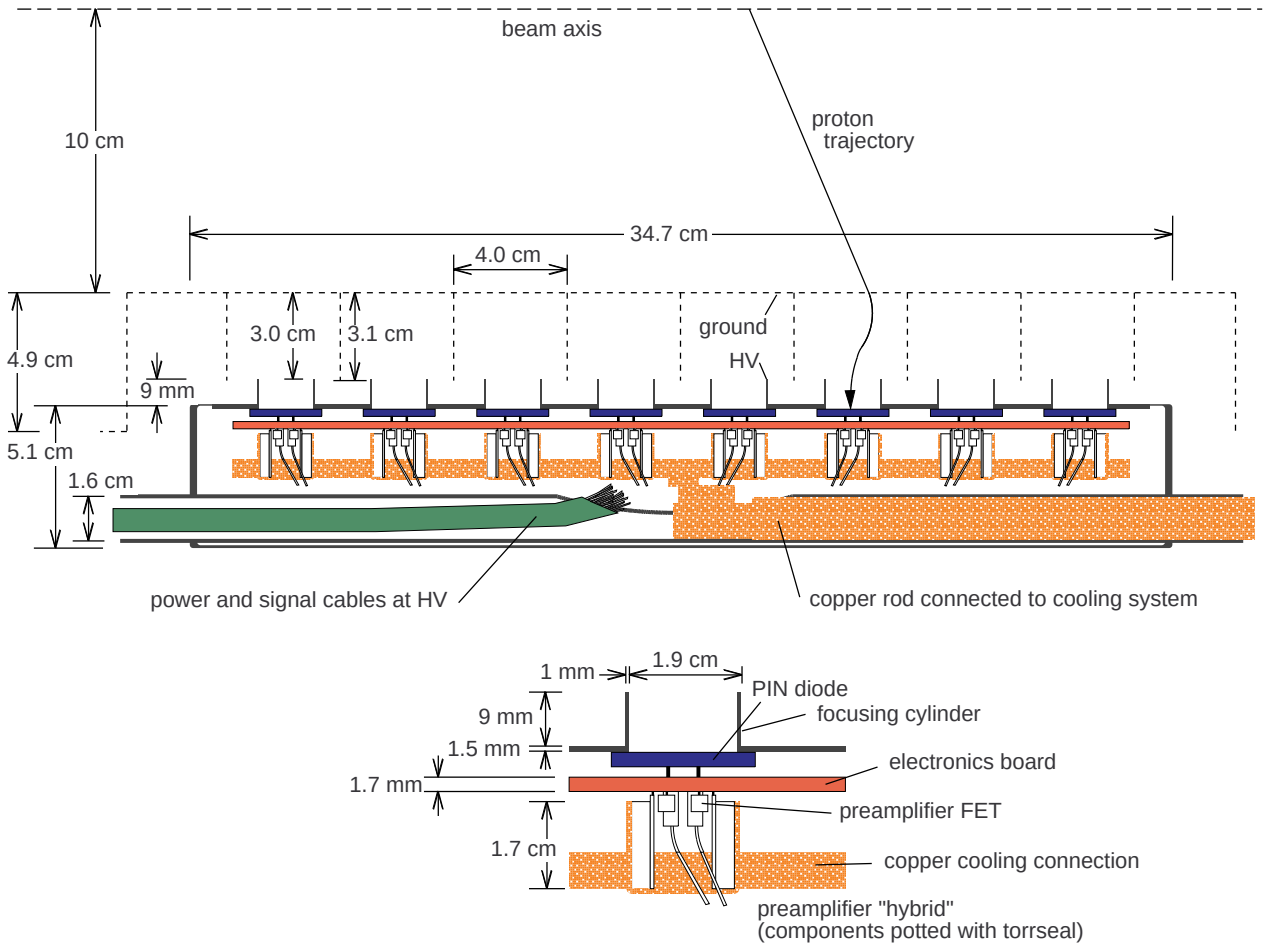

Figure 3.27: A cross section of the proton detector shows the tightly-packed region inside the high voltage portion inside the detector vacuum chamber. There are 16 spaces for the PIN diodes, each behind a cylindrical opening in the electrode that focuses the incident protons . The preamplifier circuits sit directly below the diodes, secured with Torr-Seal epoxy to the copper cooling connection.

The detector housing and components were fabricated of 304 stainless steel and annealed to reverse the increase of permeability that occurs when the metal is machined or welded. The annealing is done at 1330-1350 °C for one half hour in a hydrogen environment. Components were held with weights during annealing to prevent warping as the high temperatures release the machining stresses. The electrode surfaces were machined to have smoothed, continuous edges, and were ultrasonically cleaned and electropolished prior to installation to prevent sparking and emission.

3.6.2 Proton Electronics

For each incident proton, the PIN diodes produce a charge of less than 0.003 pC. The emiT preamplifier (see figure 3.28) creates from the PIN signals a negative tail pulse with 50 ns risetime and a 50 μs tail. The preamplifier has an inverted cascode input stage with an Interfet IF4501 JFET (C_{iss}=35 pF). The gain in this stage is 1 V/pC, and a postamplifier with 5 transistors provides a further 10-fold amplification. The preamplifiers are designed to provide low-noise amplification for the diodes, which have a capacitance of 80 pF at full bias. Noise is minimized by cooling the IF4501 JFET to 0° C. All of the preamplifier components except the IF4501 JFET and the protection diodes are surface mounted on a 1.5 × 3 cm single layer board. This portion of the circuit is referred to as the hybrid. The circuit requires +10 and -8 V with a power dissipation of approximately 100 mW.

The shaper/ADC boards shape and attenuate the pulse before sending it to a discriminator and a peak-sensing ADC, as shown in figure 3.29. The shaping and peak-detection networks are shown in more detail in figure 3.30. The gain, threshold, and mode parameters are set using an Alterra 7192QFP Field Programmable Gate Array chip as the programmable interface. The boards are constructed in VME (VersaModule Eurocard, IEEE standard 1014-187) format to receive power and communication through the VME interface [49]. Each board has 8 inputs for preamp signals, two connectors with one TTL (transistor-transistor logic, 0 to +5 V) input and one output, and an additional "D" connector with input output for monitoring discrimator levels or making a front-end clear. The boards can be initialized, read, and cleared via the VME bus. There are eight separate discriminator and ADC channels, and an Alterra 7192QFP Field Programmable Gate Array chip served as the programmable interface. During initialization, the chip is programmed

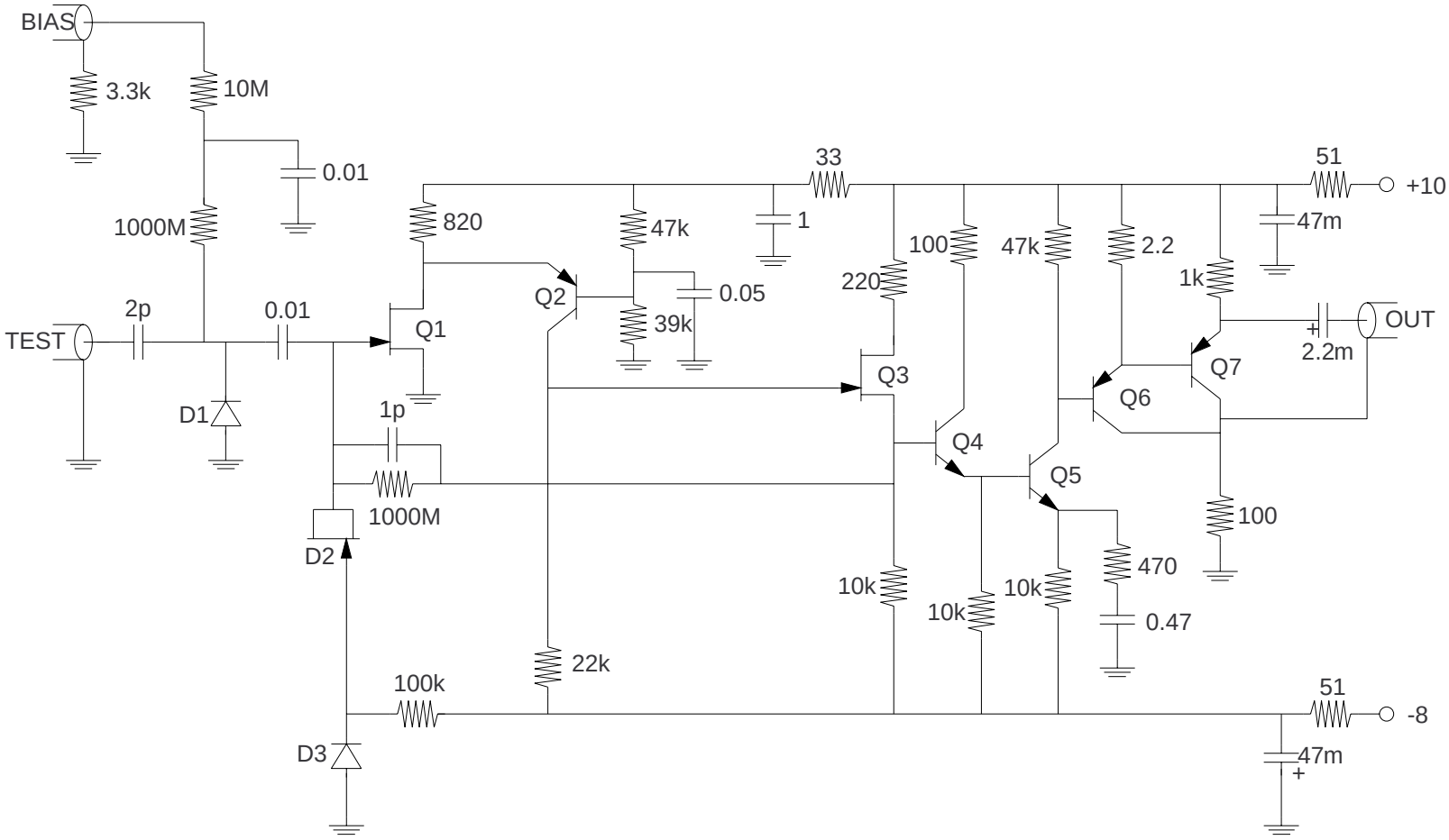

Figure 3.28: The emiT preamplifier circuit.

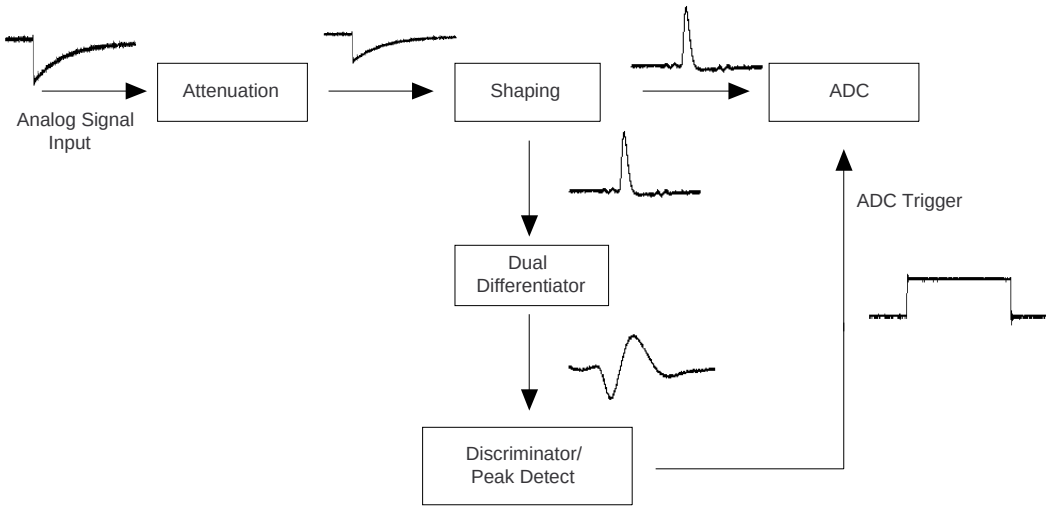

Figure 3.29: Schematic diagram of the emiT shaper/ADC board.

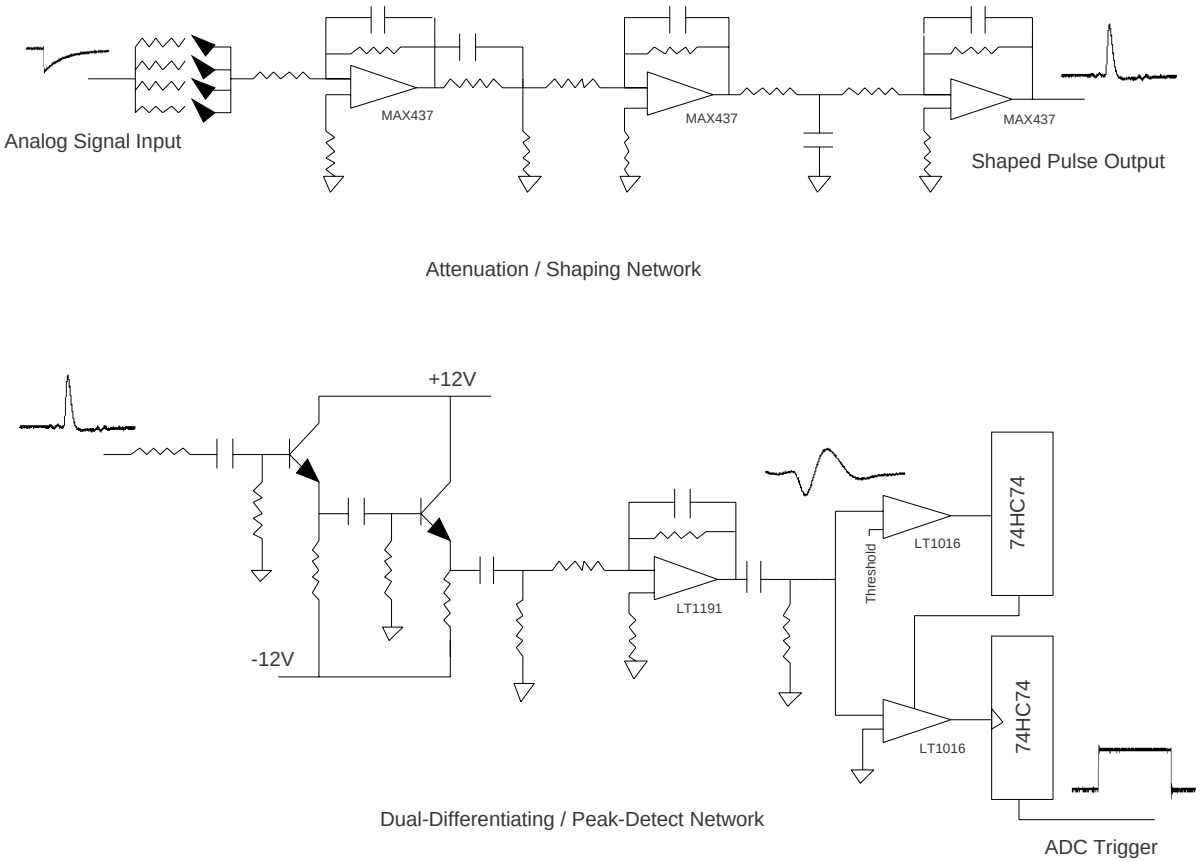

Figure 3.30: Details of the emiT shaper/ADC board.

with a shaper gain value and a discriminator threshold for each channel, and operating mode is chosen. In "independent mode", each channel operates without regard to the others. When a channel receives an input that crosses the threshold, it converts the data and waits to be read and cleared. In "lockout mode", a channel in the process of conversion causes the others to be inhibited, preventing them from accepting signals until the whole board is read and cleared. In addition, the board will accept an external inhibit via the TTL input on the front end. In order for the board to accept new signals both internal and external inhibits must be lifted. The external inhibit is cleared by bringing the TTL input low, and the internal inhibit can be lifted by the VME controller or by a front-end fast clear, which is delivered as a TTL signal through the "D"-connector. In lockout mode, the boards also make a TTL output that indicates the start of the conversion and internal inhibit of the board. This signal is correlated with the arrival time of the PIN pulse and can be used in measuring the relative time of beta and proton detections.

3.6.3 Cooling

The performance of the preamplifiers and PINs generally improves with decreasing temperature, as does the ability of the electrodes to hold voltage. Since the preamps in each proton detector produce a total of several watts and are operating in vacuum, it is crucial to have a cooling system with sufficient capacity, speed, and solid contact with each component to reduce electronic noise and prevent component burnout. A ladder-shaped copper bar was mounted on the back of the preamplifier board. The bar was connected to heat sinks on the preamplifier components. The heat flows from the ladder through a flexible connection to a copper rod that brings the heat to the end of the detector housing. This system can be seen in figure 3.27. There the copper rod is connected via a ceramic break to a low-voltage heat sink cooled by fluid lines.

The coolant used in the first cycle was several liters of alcohol cooled with a commercial chiller to a few degrees below freezing. The chiller was attached to the chamber with flexible tubing to avoid transmitting vibration that creates microphonic noise in the proton detectors. In several efforts to reduce the operating temperatures, this chiller was replaced with a colder chiller, and finally with a liquid nitrogen delivery system.

3.6.4 Proton Segment Testing

High Voltage

The electrodes required many hours of "conditioning" before they could hold high voltage. Conditioning is a process of coaxing the electrodes to hold a higher and higher voltage by either taking large voltage steps,forcing sparks in order to blow off any microscopic high points, or by increasing the voltage in small steps, waiting several hours or days at each value. Neither technique proved reliable. Conditioning generally improves the stability (reduced magnitude and frequency of sparks) and reduces the emission of electrons and x-rays. At times a large spark destroys a day's conditioning, presumably by creating more surface imperfections than it removes. The conditioning process must be repeated after exposure to air or handling, and after most large sparks.

The emission was investigated with a beta detector. The beta detector rates with no high voltage were generally near 60 Hz. With a single proton electrode (unconditioned) at high voltage on the other side of the detector, the rate in the beta detector began to rise at 20 kV, reaching 1 kHz near 27 kV, and continued to increase up to nearly 100 kHz. Spectra taken during sparks showed spikes with widths of 20-50 and energies slightly greater than the electronic noise. No high-voltage-related increase in beta detector rate was seen when a 6 mm thick sheet of clear plexiglass covered with aluminum foil was placed in the chamber between the two detectors. The plastic/aluminum was large enough to block both light and electrons, and the rate in the beta detector remained steady at 60 Hz with this in place. To determine the nature of the emission, the aluminum foil was removed, but this had no effect on the beta detector rate. This would seem to indicate that the emission-related background in these conditions was primarily electrons rather than light. The aluminum foil wrapped around each beta detector after this test is thick enough to stop a 40 keV electron.

PINs and Electronics

The PINs were calibrated with a ^{241}Am source. Figure 3.31 shows the calibration obtained at the end of the experimental run. Protons from the Notre Dame tandem accelerator were used to measure the dead-layers of several of the PINs [50]. This measurement was made by scattering 93 keV protons from a gold foil into a PIN diode. The scattered beam has a lower energy and lower intensity than that of the incident beam, whose high intensity

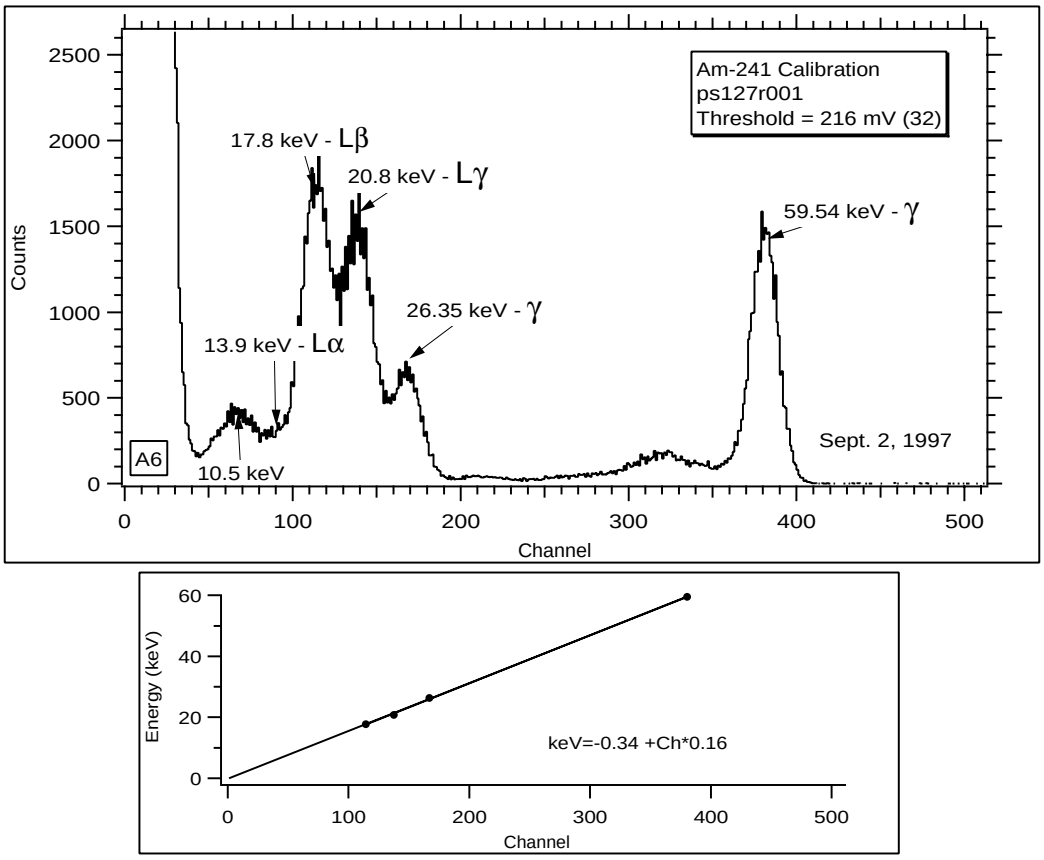

Figure 3.31: Americium calibration from the end of the run.

would damage PINs. The measurements were made in such a way as to determine this incident energy and the dead-layer thickness (d_{dl}) simultaneously. The PIN was positioned with its surface at angles of 90° and 55° to the scattered beam as shown in figure 3.32. Proton energies were determined with the ^{241}Am and ^{137}Cs (60 keV x-ray) calibrations. The energy loss (dE/dx) in silicon is approximately 0.5 keV-cm$^2/\mu$g for protons above 30 keV, and rises sharply at lower energies. The dead-layer thickness can then be calculated by looking at the difference in measured energy for the two incidence angles

$$d_{dl} \approx \frac{E(55°) - E(90°)}{dE/dx(1/\cos 55° - 1)}. \tag{3.17}$$

All but one of the PINs measured had dead-layers of approximately 20 μg/cm^2, consistent with the specification. Further measurements of the PIN dead-layers will be discussed in Chapter 4.

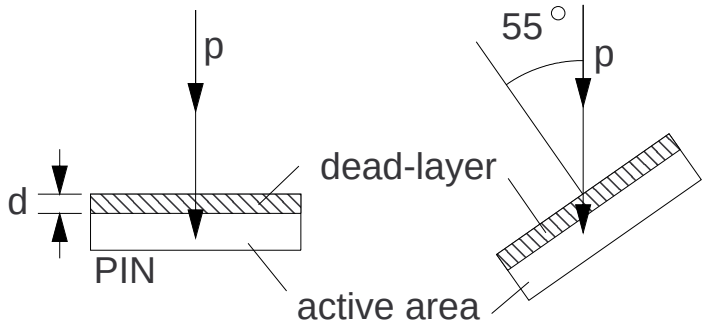

Figure 3.32: Protons from the Notre Dame tandem accelerator were used to measure the PIN dead-layer thicknesses. Part of the proton energy is lost in the dead-layer and the remainder is collected by the PIN. Measurements are made at two angles of incidence so that the dead-layer thickness can be extracted without exact knowledge of incident proton energy.

3.7 Vacuum

The vacuum pumping system is completely oil-free. The "roughing" pumps are attached at the center of the collimator. A Varian Turbo-V259 200 l/s is backed by a Varian 600 DS oil-free scroll pump. This is used to bring the pressure into the microtorr range, at which point the pumping is switched over to a CTI Cryogenics Cryo-Torr 8 cryopump capable of pumping water vapor at 4000 l/s. Although it was connected to the system with a flexible bellows, the turbopump created too much vibration on the system, visible as microphonic noise in the diodes. A vacuum of at less than 10^{-6} torr prevented scattering of the neutron beam. The pressure was measured with ion gauges at the turbo pump connection and about 1 meter downstream of the detector center. The pressure during the experiment was between 2×10^{-6} and 5×10^{-8} torr.

Because the PIN diodes are cooled well below the condensation point of water, effective water vapor removal was important to prevent condensation. The gas load in the system was in large part water, due to the large quantities of plastic in the detector region, including the beta detectors and the materials in the proton electronics such as the plastic electronics board, connectors, and heat shrink. The presence of these materials also made it impossible to bake the detector region.

To further reduce the amount water near the detectors, a "cryopanel" assembly (see figure 3.33) was designed to provide cryopumping as close to the detectors as possible. At each end of the detector chamber a tank of liquid nitrogen extends into the vacuum

chamber and is connected to aluminum panels cut to fit close to the ends of the detectors. These tanks were kept partially full by means of an automatic filling system controlled by an Ortec 786 LN2 controller.

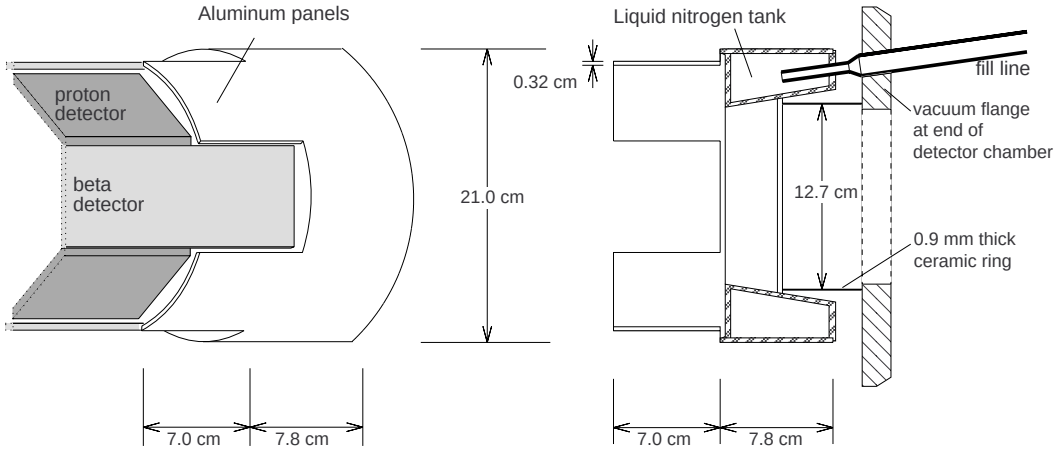

Figure 3.33: On each side of the detector chamber is a liquid nitrogen trap which fits closely around the eight detectors. The cross section at right shows the donut-shaped liquid nitrogen tank. The tank and panels are connected to the vacuum chamber by only the thin ceramic ring and the two o-rings; thus they are thermally isolated.

3.8 Data Acquisition

The data acquisition (DAQ) system was built around a Motorolla VME CPU with 12 MB of RAM. This was connected via NuBus to a 66 MHz Macintosh Quadra 950 with a Power PC upgrade running *emiT DAQ PPC*, a C++ program with three main functions: (1) Download acquisition C code to the VME CPU; (2) Periodically extract data from the CPU's buffer ; and (3) Send data to a small Macintosh II (the "Monitor" computer) which displays current experimental parameters.

The DAQ signal processing uses four primary signal standards: VME; CAMAC (IEEE standard 583-1962); NIM (Nuclear Instrumentation Methods, DOE/ER-0457, with -0.6 V logic pulses/levels); and TTL [49]. The CPU module sits in a VME crate containing several other modules including a scaler, an ADC, a Bit-3 413 digital fiber optic link controller, and a Kinetic Systems CAMAC communication module. Near this are a CAMAC crate with clocks, ADCs, TDCs, and NIM-level input and output, and two NIM bins

containing the signal processing for the beta detectors, spin-flip control, and coincidence trigger.

A separate rack of electronics is maintained at the same high voltage as the proton focusing system. The entire high voltage system is powered by means of a large transformer, and housed inside a Faraday cage lined with 13 mm lucite and protected by an interlock system. Inside are the shaper/ADC boards and a digital fiber optic controller, NIM-level trigger processing, a fast fiber optic link, and the power supplies for the PIN bias preamplifiers. Signals from the diodes are transferred through 4 bundles of HV-shielded cables. Digitial information is passed between low and high voltage via the digital fiber optic bundle, and an additional 8 optical fibers transmit the fast logic signals. Figure 3.34 contains a schematic overview of this system. Details of the electronics, trigger logic, and timing can be found in Appendix B.

The written coincidence events, averaging 40 bytes each, vary in length since the data are stored only for beta detectors that fire during the coincidence. The header includes the file name, start date and time, and the contents of the configuration file. Each coincidence event contains the following information: (a) Number of Proton triggers and an ADC value and identifier for each. (b) Number of Beta triggers and ADC, TDC, and identifiers for each. (c) TDC values for the relative time between beta events and the triggering proton and (d) Spin flipper current, flip status (the 0 or 1 sent to the flipper controller), and the time since the last spin flip. The data set is written on 81 650 MB compact disks.

3.8.1 Coincidence Trigger

Initially the coincidence logic accepted any beta detector signal that came within 7 μs of a proton signal. This gave us the full prompt background peak at zero coincidence time, the full proton drifttime spectrum at about .5- 2 μs, and 9 μs of flat accidental background with which to estimate noise under the proton signal. The length of this window was reduced to $\pm 3.5 \mu s$ midway through the experiment to reduce the deadtime.

The first version of the trigger accepted all proton events and collected any beta events in the ± 7 μs time window. However, with a deadtime on the order of a millisecond during each computer read, the percent of deadtime becomes significant when the proton event rate exceeds 100 Hz. Online at the CNRF, the proton rate was much higher than anticipated, motivating a reconfiguration of the logic to accept coincidences only. Appendix

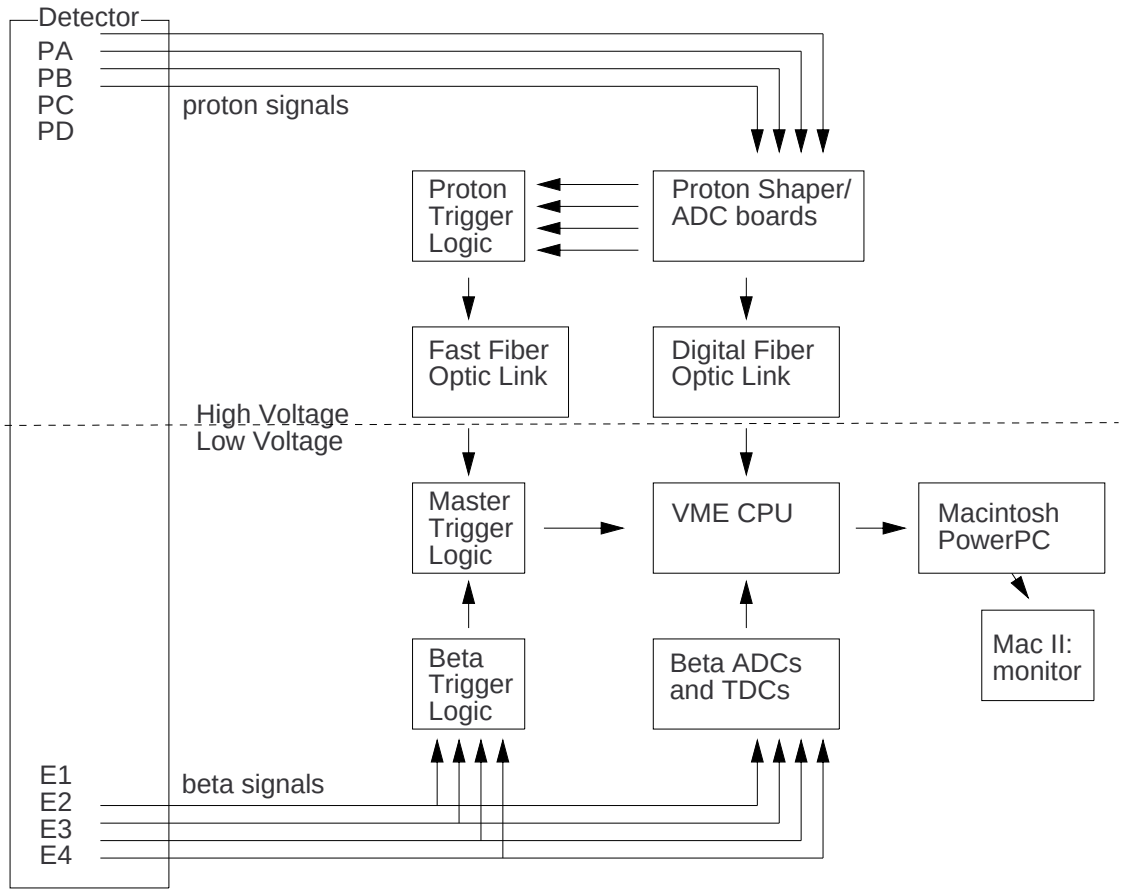

Figure 3.34: Overview of data acquisition components.

A details the configuration operating when the run ended in September 1997.

Chapter 4

Experimental Run

In August 1996, the various components of the experiment were shipped from Seattle, Berkeley, and Ann Arbor to Gaithersburg. The beam tests and data collection occurred over three 6-week reactor cycles beginning January 2, 1997.

August 1996	Ship experiment to NIST
December 1-22, 1996	Install the experiment on the beamline
January 2-28, 1997	Beam characterization and detector shakedown
February 6 - September 1, 1997	Data collection
September 2-12, 1997	Beam characterization and removal of the experiment from the beamline

Figure 4.1 is a photograph of the experiment at the CNRF. Figures 4.2 and 4.3 are photographs of two regions of the spin transport, and figure 4.4 shows the detector hoisted into the air by the CNRF overhead crane. The crane was used to raise and lower the detector into place after assembly and alignment of the beam and guide field were complete.

4.1 Installation

4.1.1 Beam Development

The flux of neutrons from the NG-6 guide was measured by activation of six gold foils for one hour each . To measure the beam profile, a fission chamber was mounted behind a 6mm thick sheet of ^{6}Li-glass with a 1 mm pinhole aperture as shown in figure 4.5. This was mounted on a computer controlled x-y stage to scan through 225 points on a 60 mm $\times$ 60 mm grid. To measure the beam divergence, a sheet of Li-plastic with five 3 mm pinholes

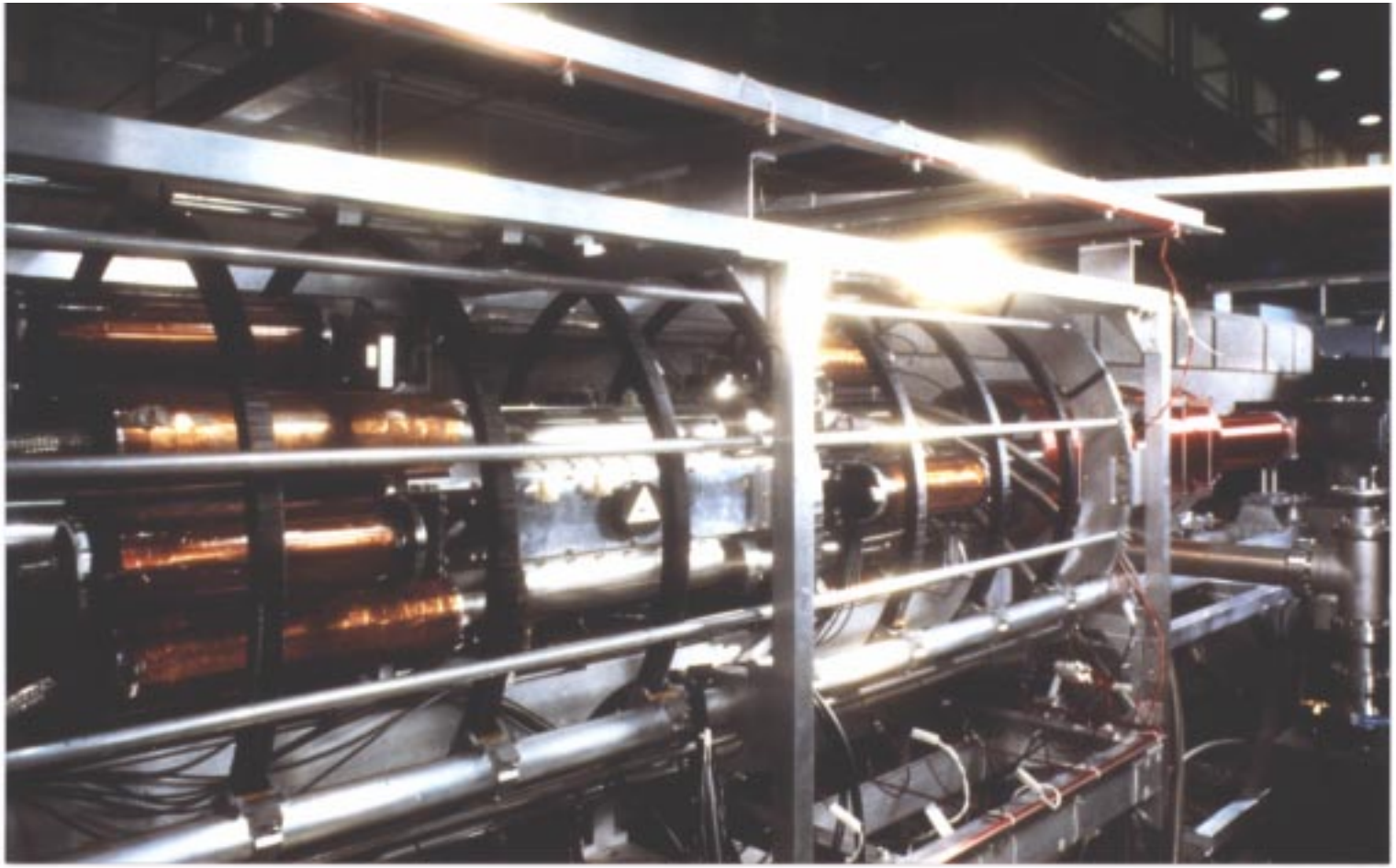

Figure 4.1: The emiT experiment installed on neutron guide 6 of the NIST CNRF. The perspective is looking at the west side, facing south toward the reactor. The detector, collimation, and spin transport regions can be seen.

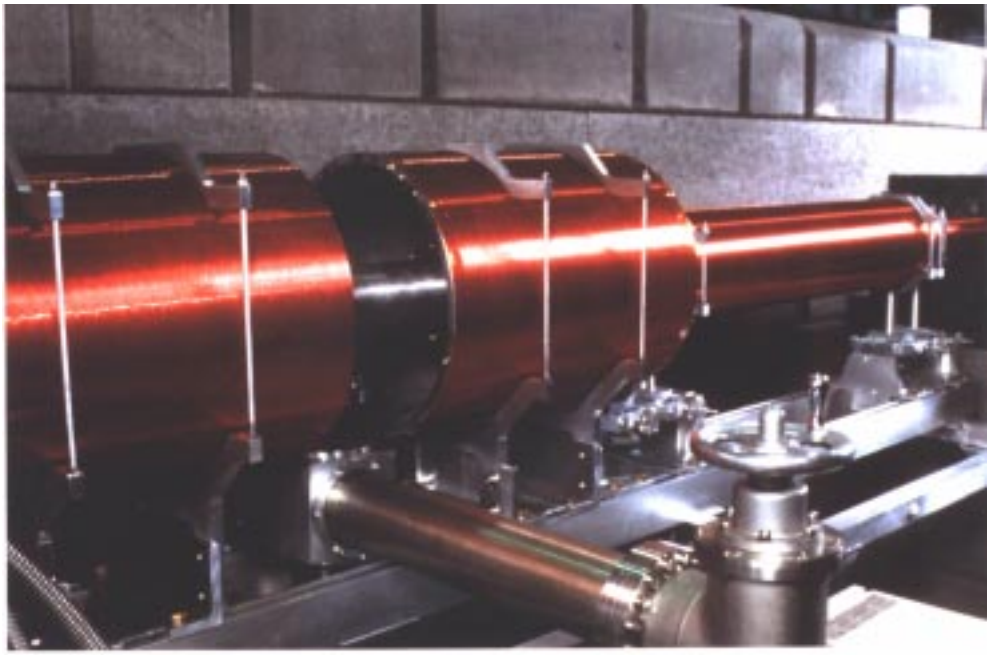

Figure 4.2: Closeup of the collimator region. The polarization in this region is maintained by the magnetic field of three large solenoids and several loops. The connection to the turbo pump and parts of the lead and concrete shielding walls can also be seen in this picture.

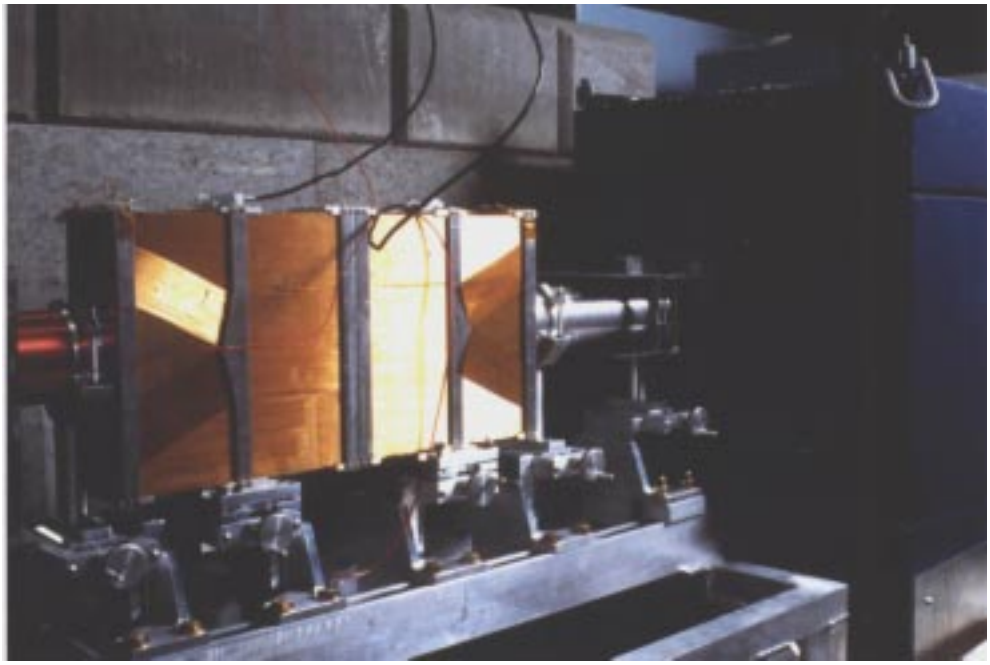

Figure 4.3: The current-sheet spin flipper and the lead shielding house for the polarizer can be seen in this photograph. The wires visible on the side of the spin flipper are the return wires for those that comprise the current sheet, located at the center of the assembly.

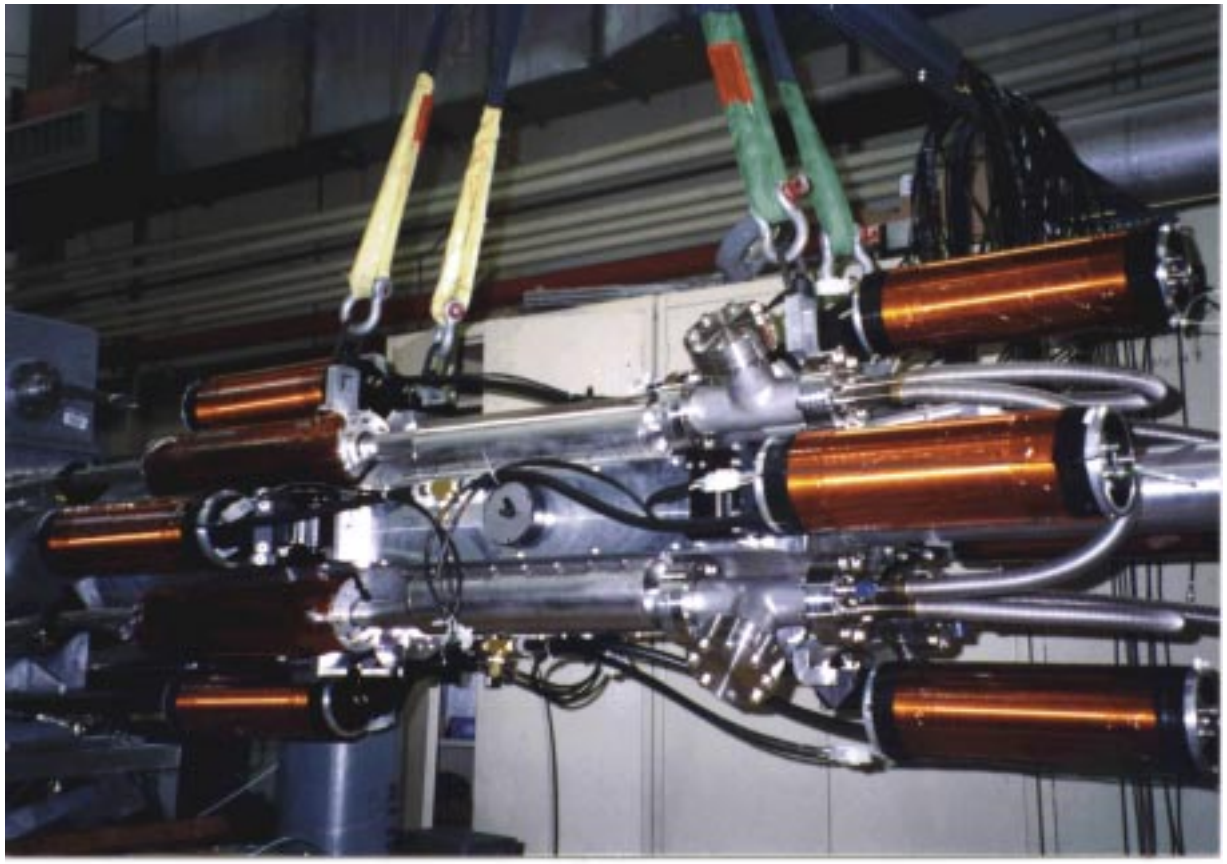

Figure 4.4: The entire detector assembly could be moved to and from the beamline by sliding the guide field coils to each end and lifting the detector with the CNRF crane. Here the detector is shown suspended above the guide hall floor during transit. In this photograph the semi-cylindrical housings for the proton detectors are clearly visible. The liquid nitrogen fill lines (evacuated, coaxial bellows) can be seen on the right linking the proton segments, and the cylindrical high-voltage shields can be seen on the left. On each end of the beta detectors, the double-solenoid magnetic shields can be seen mounted over the photomultiplier tubes.

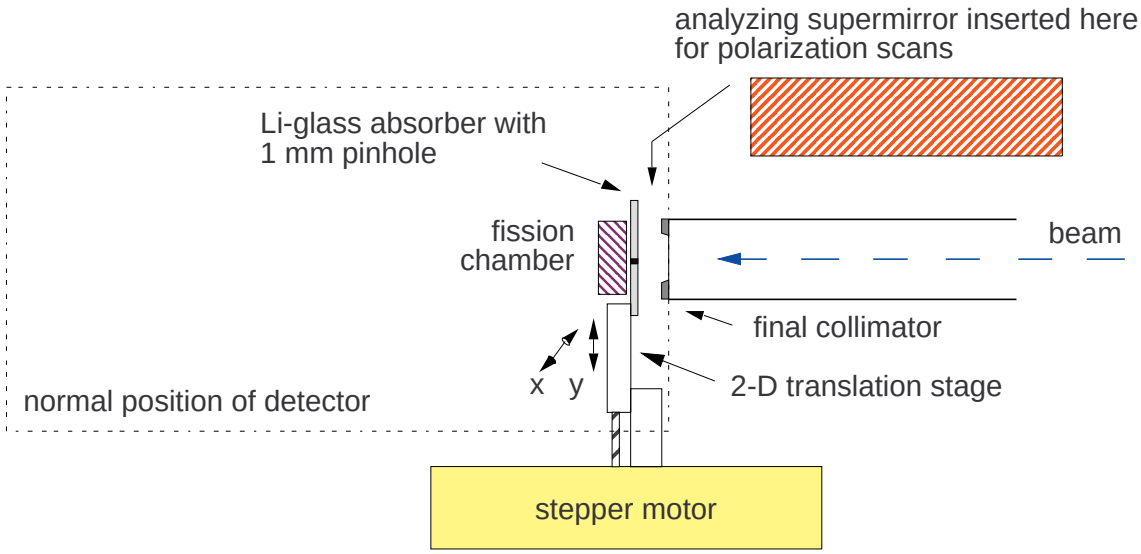

Figure 4.5: Beam characterization setup. The stepper motor translated the neutron counter (pinhole and fission chamber) vertically and horizontally in increments of 4 mm.

in a domino pattern was used. The spatial profile of the beam originating from each of the 5 points is indicative of the direction and divergence of the beam as it exits the supermirror in different locations.

The average beam deflection was measured using a single pinhole 1.33 m from the supermirror. A one meter length of helium-filled tubing was placed in between to reduce scattering and attenuation is air. The scanner's pinhole was aligned with a theodolyte to the beam direction as defined by NG-6. The beam centroid in these scans was deflected 1.1° (26 mm), in agreement with predictions based on the supermirror geometry.

The capture flux was measured with a calibrated fission chamber at several points along the beamline as it was assembled. The results are shown in table 4.1. The measured loss in the current sheet was 10%, 5 times higher than expected 2%. This was partly due to a glyptol coating on the wires. The glyptol was removed with toluene, which is safe for the aluminum wire and Formvar coating. The transmission after glyptol removal was 6%.

Measurements of the flux profile at the ends of guide tubes 1 and 3 showed an asymmetry over the beam cross section, with greater neutron density on the west side. (The neutron travel is northward.) Data from one such scan are shown in figure 4.6. The west side of the beam also appeared to have greater divergence than the east. These high-divergence neutrons, probably created by small angle scattering in the Bi filter, have a

Position (end of:)	Flux (n/cm^2)	Measured Loss (%)	Predicted Loss (%)
NG-6 shutter	1.4×10^9		
fast neutron filter	1.0×10^9	29	30
supermirror	2.2×10^8	78	60
first guide tube (plus one Si window)	1.9×10^8	12	9
current sheet	1.7×10^8	10	2
second guide tube (plus one Si window)	1.3×10^8	26	9
third guide tube	1.2×10^8	10	8
collimator	1.1×10^8	14	-

Table 4.1: Fluence rates and losses in emiT beam components.

greater probability for absorption in the guide tubes. Despite the large variation in the beam at the guides, the beam was more uniform after passing through the collimator. The centroid of the measured flux density profile was displaced 0.63 mm to the west of beam axis.

4.1.2 Polarization Measurement

The polarizing/analyzing power of a polarizer depends on the difference in transmission of the two spin components of an incident beam. Defining f to be $T^{\uparrow}/T^{\downarrow}$, where $T^{\uparrow}$ is the transmission of one spin state and $T^{\downarrow}$ is the transmission of the other spin state, the polarizing power is defined as

$$P = \frac{T^{\uparrow} - T^{\downarrow}}{T^{\uparrow} + T^{\downarrow}} = \frac{f-1}{f+1}. \tag{4.1}$$

For an unpolarized incident beam, the resultant polarization is equal to the polarizing power.

For a polarized incident beam, the analyzing power determines the total transmission. If the initial polarization is $\mathbf{P}_0$ (magnitude P_0), the two spin states have fluxes

$$\Phi^{\uparrow}(\mathbf{P}_0) = \frac{P_0+1}{2}\Phi_{total}, \quad \Phi^{\downarrow}(\mathbf{P}_0) = \frac{P_0-1}{2}\Phi_{total} \tag{4.2}$$

and the flux transmitted through the analyzer (A) will be

$$\Phi(\mathbf{P}_0, A) = T_A^{\uparrow}\Phi^{\uparrow}(\mathbf{P}_0) + T_A^{\downarrow}\Phi^{\downarrow}(\mathbf{P}_0) = \left(T_A^{\uparrow}\frac{P_0+1}{2} + T_A^{\downarrow}\frac{P_0-1}{2}\right)\Phi_{total} \tag{4.3}$$

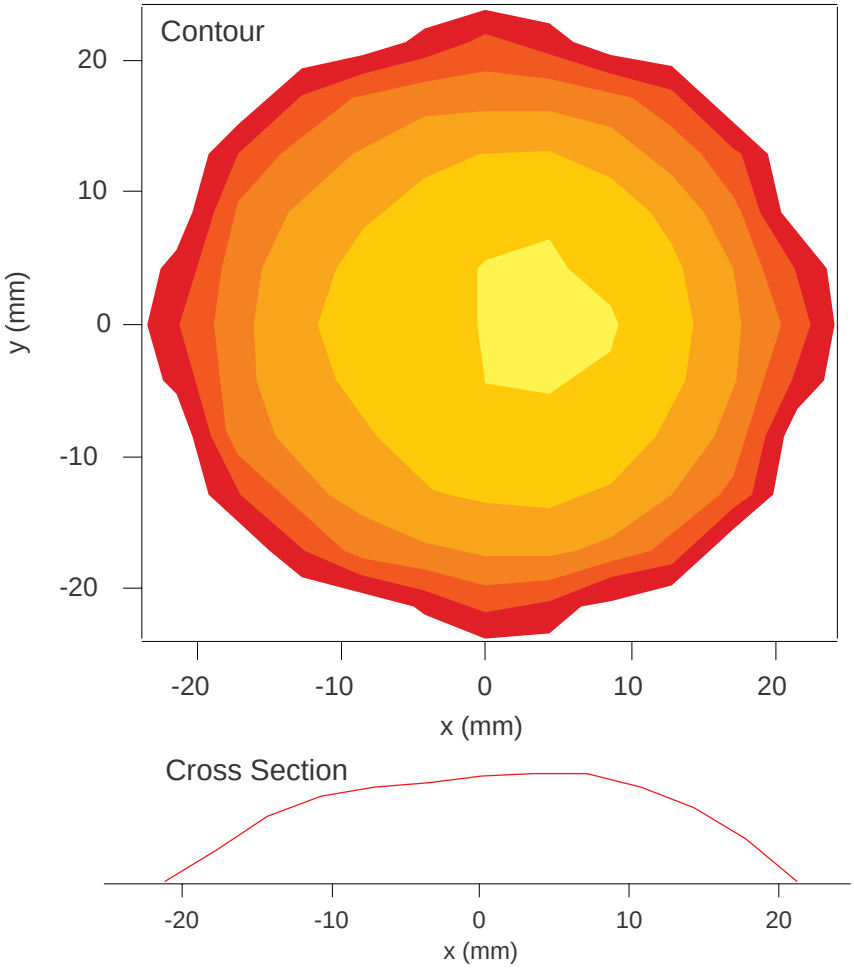

Figure 4.6: Beam flux profile at the end of the collimator. This is a viewpoint looking south: x increased toward the west. The centroid of this distribution is x=0.6 mm, y=-0.2 mm (error: $\pm$0.02 mm).

With a spin-flipper following the first polarizer, $\mathbf{P}_0 \rightarrow -s\mathbf{P}_0$, where s is the spin flipping efficiency, approximately equal to -1 for a good flipper. With the spin flipper on

$$\Phi^{\uparrow}(-s\mathbf{P}_0) = [(sP_0 - 1)/2]\Phi_{total}, \quad \Phi^{\downarrow}(-s\mathbf{P}_0) = [(sP_0 + 1)/2]\Phi_{total} \tag{4.4}$$

To make a measurement of the polarization (P_{SM}) from the supermirror, an analyzing supermirror (analyzing power P_A) is placed after the spin flipper. Defining $\Phi_{OFF} = \Phi(P_{SM}\hat{y}, A)$ as the transmitted flux with no spin flip and $\Phi_{ON} = \Phi(-sP_{SM}\hat{y}, A)$ as the transmitted flux with the spin flipper on, it can be shown that

$$\frac{\Phi_{OFF} - \Phi_{ON}}{\Phi_{ON} - s\Phi_{OFF}} = P_{SM}P_A = \frac{(f_{SM} - 1)}{(f_{SM} + 1)}\frac{(f_A - 1)}{(f_A + 1)} \tag{4.5}$$

The measured fluxes were related as

$$\Phi_{OFF}/\Phi_{ON} = 11.84 \pm 0.08 \tag{4.6}$$

Using the spin flipping efficiency of $s = -0.95 \pm 0.05$ gives $P_{SM}P_A = 0.885 \pm 0.015$. The analyzing supermirror was not identical to the polarizing supermirror, having reflective coatings on only one side of each glass plate. This indicates a flipping ratio of $f_{SM}/f_A = 2.0 \pm 0.5$. Solving for the polarization then gives $P_{SM} = 0.963 \pm 0.013$.

4.1.3 Magnetic Field Measurements

After installation of the detector frame, the magnetics were aligned to the beam axis with the theodolyte, and the currents tuned to give the most uniform horizontal field with the smallest transverse field in the detector region. The resultant field had a z-component of 5.4 gauss (northward) at the center of the detector. Results of the field maps are shown in tables 4.2 and 4.3.

4.1.4 Background Measurements

Various contributions to the background and the effects of various filters and shields were measured using the response of the detector with no proton high voltage. Background rates were measured with the beam off and on, and relative rates (above electronic noise) were compared. The results are shown in table 4.4. The 10 cm lead shielding wall around guide tube 3 proved useful for shielding gamma-rays from the reactor and neutrons scattered upstream. Beta and proton detector rates were about 20% lower with the

Field	z=-40 cm	z=0	z=40 cm
Without guide field or gradient coils:			
B_x	1.5 mG	0	-8 mG
B_y	-30 mG	0	30 mG
Without guide field:			
B_x	0.5 mG	-1 mG	-6 mG
B_y	3 mG	-4 mG	4 mG
With all fields:			
B_x	-0.5 mG	-2.5 mG	-11 mG
B_y	15 mG	2.5 mG	15 mG

Table 4.2: Transverse magnetic fields in the detector region.

Field Gradient	Maximum Value
dB_x/dy	0.5 mG/cm
dB_y/dx	0.3 mG/cm
dB_y/dy	0.2 mG/cm
dB_x/dx	0.5 mG/cm

Table 4.3: Magnetic fields gradients across the beam location.

wall. To measure the reactor gamma-rays and background produced in the supermirror, neutrons were stopped before the spin flipper in 3 mm of Li-plastic. This test indicated that approximately half of the background is from neutron absorption in the supermirror, and that the other half is produced downstream primarily from neutron scattering on the spin flipper wires, and in the nearby silicon window. The estimated backgrounds from the collimator and the beam stop were negligible [51]. To measure the effect of reactor gamma-rays and fast neutrons in the beamline, a 5 cm thick block of Bi was placed just downstream of the supermirror. A 15% reduction in the background was measured during this test, but this was due to the reduction of neutron flux (and thus less absorption in the spin flipper) rather than from useful filtering by the added bismuth. In the final test, the cryopanels were filled to estimate background from scattering by residual gas in the chamber. No effect was seen.

Radiation levels were also measured with γ- and n-detectors near parts of the beamline, and these measurements (see table 4.5) were consistent with the understanding

Configuration	Average Rate in Beta Detectors [Hz(rel.*)]	Average Rate in PIN diodes [Hz(rel.*)]
1.Partial lead wall (beam off)	140 (0.19)	0.081(0.17)
2.Partial lead wall	870 (1.18)	0.549(1.23)
3.Li-plastic before spin flipper	440 (0.60)	0.176(0.39)
4.Complete lead wall	735 (1.0)	0.466(0.95)
5.Bi block after supermirror	625 (0.85)	0.403(0.82)
6.Cryopanels filled	735 (1.0)	0.489(1.00)

Table 4.4: Detector response to background sources and shielding. In configurations 1 and 2, the lead wall was built only up to the underside of guide tube 3. The full lead wall rose 15 cm above the guide tube. The average rates in the detectors were measured with the regular beta detector thresholds. Proton rates were counted in the spectra, ignoring the lowest 150-300 channels. *Rates are given relative to configuration 6, that used in the experiment.

Location	gamma (mR/hr)	neutron (n/cm^2/sec)
Outside lead blockhouse around polarizer	5-10	30-50
Current sheet	≈ 40	≈ 1500
Lead wall	4-5	100
Various locations downstream of lead wall	< 1	$\leqq 10$
Beam Stop	5	$\leqq 10$

Table 4.5: Radiation levels outside the apparatus.

of the contributions to the background. The total contribution to the background from radiation sources was less than 1 kHz for each beta detector and below 1 kHz for all proton detectors combined. This indicates an radiation-related accidental background rate of under 16 Hz in the 14 μs coincidence window.

4.1.5 Interlock System

For most of the first run,the experiment was attended at all times. Over the course of the run, probable failure modes were considered in constructing and testing an interlock protection system, making it safe in the last reactor cycle to leave the experiment unattended for up to 6 hours. The final version of interlock system monitored the high voltage, the vacuum pressure, and the PIN leakage current. In the case of a large spark, the high voltage is disabled. This prevents further spark damage as the voltage is automatically

ramped up to the set point. In the case of a vacuum failure, the cryopump valve is closed and the HV and detector power are disabled. This prevents pressure-induced sparking and damage to light-sensitive detector components that would occur if the vacuum failure is accompanied by a light-leak. If the PIN leakage current becomes too high ($> 1\mu$A), the proton detector power is cut off. This protects the PINs from overheating in the case of a cooling failure. In this capacity, the PINs serve as a sensitive thermometer. The PIN leakage current can also rise in the event of a light-leak, which is also potentially damaging to the PINs if they remain biased. The beta detector power supplies have internal current limiting, and thus were not connected to this interlock system.

4.2 Physics Run

The stability and performance of the detector system was well below optimal in this first run. The proton energies measured in the PIN diodes were typically 10 keV lower than expected, primarily due to PIN surface dead-layers which appeared to be twice the specified thickness. Attempting to detect these lower-energy protons pushed the limits of the detector performance. Lowering thresholds increased the sensitivity to electronic noise (and thus to temperature) and other sources of background, and the sensitivity to the sharpness of the threshold. Increasing the acceleration voltage decreased the high voltage stability greatly. Many changes were made during the run to improve the detector performance. These are described below. Further improvements are being addressed for the next run and are discussed in Chapter 6.

4.2.1 Minor Changes

During the first reactor cycle, the rate of dark current noise in one of the eight phototubes (E3B) began to rise from its original rate of 100 Hz to several kHz. The light seal was thoroughly checked and the base was replaced with no effect. The tube was replaced with one of the two spares, both of which had normal dark current rates in bench tests. Unfortunately, after installation the new tube had a slightly higher noise rate than the original. The trigger on this beta detector was raised by 20 mV to 80 mV, giving a trigger rate of just over 1 kHz. With the beam on, the total background rate in this detector was typically twice that of the other three. Towards the end of the run, a tube on another detector had become noisy, and that detector's threshold was also raised 20 mV.

In an attempt to recover some of the cold neutron flux lost to absorption in the fast neutron filter, the 15 cm of bismuth was removed. The loss for each of the three 5 cm crystals is about 8%. With no filter, the flux increased by 28%, with negligible effect on the background rates. However, the increased flux of fast neutrons being scattered in the apparatus created a significant increase in background in the neighboring experiment. The concrete wall between the two experiments was not adequate for shielding this type of background. Several attempts at a compromise were made with smaller amounts of Bi, Bi and Be, and with 2.5 cm of sapphire crystal. The sapphire attenuated the flux by 30% more than the initial 15 cm of Bi. 10 cm of Bi gave the maximum tolerable background in the other experiment with the smallest loss (15%) of flux for emiT.

4.2.2 Proton Electronics

There was noise on the VME shaper/ADC boards due to pickup in the boards, some cross-talk, and errors during conversion due to the fact that the discriminator pulse and the pulse to the ADC were not the same. The signal pulse, which is negative and unipolar, is first split, with one pulse being converted to the derivative (bipolar). The discriminator fires when the negative edge of the bipolar pulse crosses a threshold level, triggering the ADC to read when this bipolar pulse crosses zero. This position is the peak position of the unipolar pulse. Therefore, its amplitude at that time is its peak height. If this pulse has high frequency noise on it, the measured peak height is the real amplitude plus or minus the noise amplitude. If the conversion to bipolar is inexact, causing a second, smaller dip to the negative to follow, this second dip can trigger the discriminator. The ADC will then register a low energy value as it reads the pulse height in the tail of the unipolar pulse. This type of effect is illustrated in figure 4.7. Modifications in the boards during the run reduced the pickup and cross-talk. There is also noise on the boards introduced through the VME connector when the VME bus is used to poll the boards to determine if there has been an ADC conversion. This is the method used when collecting proton singles data. The coincidence acquisition used the front-end logic signal as the conversion alert. Thus the coincidence data do not have noise from this source.

The discriminators in the shaper/ADC boards do not have "hard" thresholds. With a hard threshold, the electronics accepts all pulses with amplitude above V_{thresh} and excludes all pulses below, which is equivalent to multiplication of the spectrum by

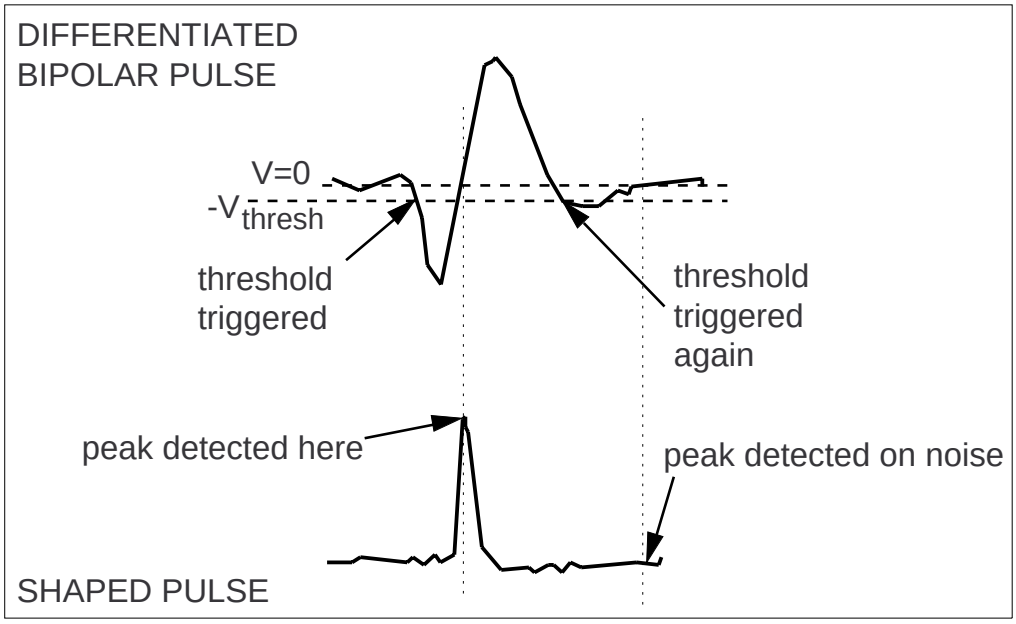

Figure 4.7: The shaper/ADC board makes two pulses from the negative, unipolar input pulse from the preamplifiers. One pulse is a shaped and amplified copy of the input and the other is bipolar, the differential of the input. After triggering the discriminator by crossing its negative threshold, the next zero crossing of the unipolar pulse signals the ADC to read the peak voltage of the amplified pulse. Imperfect shaping of the bipolar pulse can give it a second negative dip, which will trigger the ADC to read noise.

$\theta(V - V_{thresh})$. The emiT boards have "soft" thresholds, in which the fraction of signals accepted rises from 0 to 1 slowly as the energy increases. The discrimination follows the peak detection: both use the same crossover circuit. The discriminator acts on a pulse that is differentiated two more times after the pulse is analyzed. Also, the threshold-crossing is detected at a time different from the sample-and-hold time. This difference leads the observed threshold behavior. Since the proton peak in the energy spectrum was not well-separated from the background, there was always some lower-energy background accepted by the discriminator. This is illustrated in figure 4.8. Figure 4.9 shows typical data for the position of the proton peak, plotted against the threshold.

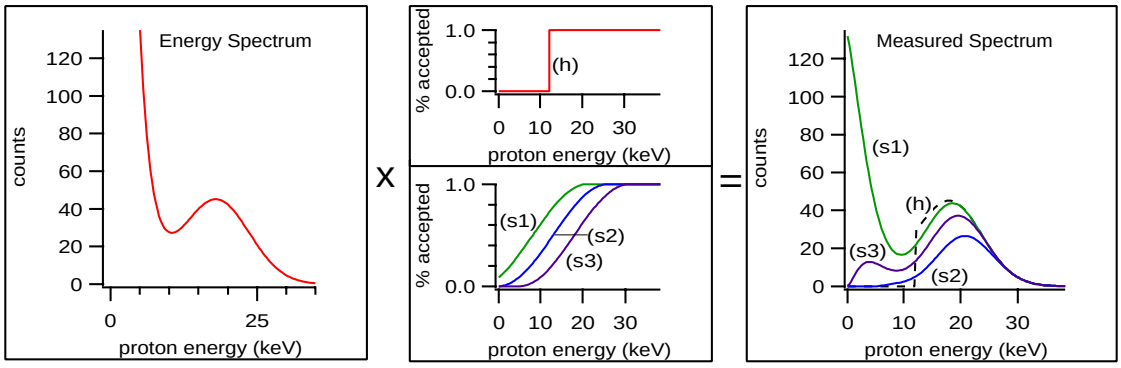

Figure 4.8: Comparison of "soft" and "hard" thresholds. A hard threshold (h) more effectively rejects low-energy background. Note that as the soft threshold is raised (s1-3), the centroid of the peak becomes higher.

4.2.3 PIN Diodes

Another source of noise in the proton detectors was associated with the PIN leakage current. This current decreased with improved cooling and varied among the portions of the detectors due to temperature inhomogeneities. In one test of the cooling system, a drop in the leakage current from 0.7 μA to 0.4 μA allowed the thresholds to be lowered enough to give a factor of 3 increase in the proton detection rate. With the improved cooling (see section 4.2.4) the leakage current was in the nanoampere range and the thresholds could be set low enough in some PINs to give rates close to the estimated beam-limited rate of 0.25 Hz per PIN.

In preliminary tests, the dead-layers of the PINs were measured to be $20\pm2\mu g/cm^2$ as specified by the manufacturer. In a dead-layer of this thickness a 35 keV proton loses

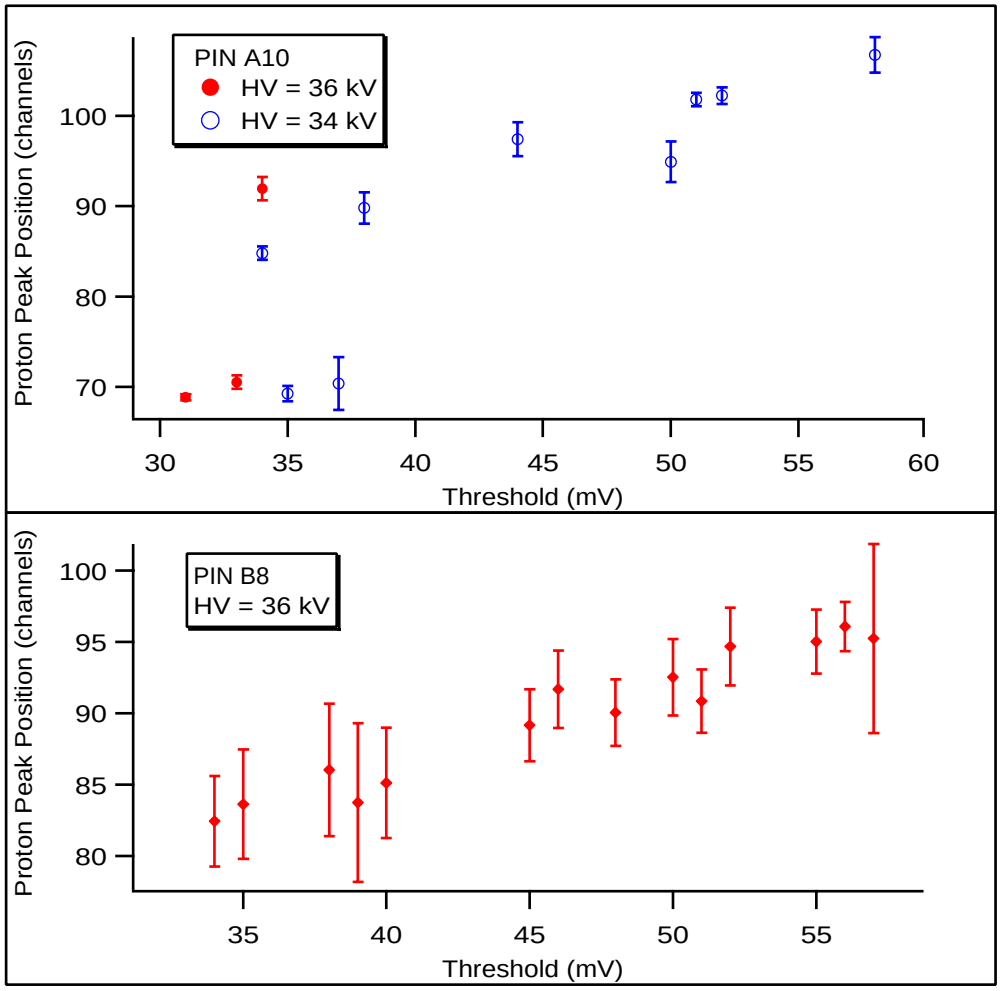

Figure 4.9: Proton energy peak position versus ADC threshold setting for two representative PINs.

Date	Location	Technique	Error
1/95	Notre Dame	protons (E and ΔE)	10%
3/96	Notre Dame	protons (E only)	15-20%
4/97	Notre Dame	Gd alpha	15%
6/97	NIST	Gd alpha	15%
9/97	Washington	Gd alpha	15%
5/98	Washington	Gd alpha	15%

Table 4.6: Dead layer measurements. The first test at Notre Dame is that described in section 3.6.4, using protons scattered on gold foil, and comparing the energy loss at different angles of incidence. The 3/96 test was a check of 6 PINs in which the proton incidence angle was not varied. In this test, all PINs showed dead layers of $20 \pm 4\mu g/cm^2$. The 1997 and 1998 measurements used alphas from gadolinium-148. The alphas were collimated with a 5 mm pinhole and energy measurements were made with incidence angles of 0 and $\pm 45°$.

10 keV of energy. The proton energies measured during the experiment, however, were an average of 20 keV below the energy imparted to them by acceleration through 34-38 kV. The width (FWHM) of the proton peaks was approximately 10 keV, and at 12-18 keV, these peaks were not well separated from the background. The energy loss was determined with the calibrations from ^{241}Am (see figure 3.31). There was also a single Sn-119 x-ray source permanently installed on the inside of the focusing plate over PIN C14. The tin produces a 24 keV x-ray. This peak was always higher in energy than the proton peak (see figure 4.11).

The dead-layer measurements described earlier were made in 1995. A similar measurement was made during the experiment using alpha particles instead of protons and again comparing the measured energies at different angles of incidence. These measurements generally indicated dead-layer thicknesses of up to 40 $\mu g/cm^2$. A summary of the dead-layer measurements is given in tables 4.6 and 4.2.3. The explanation for this is unclear. These tests were done at room temperature, so it was clear that the extra dead layer is not due to condensation on the cold detectors. Additionally, during the run, there was no clear trend in peak energy as the cooling temperature varied, which one would expect with a condensation effect. Only one of the PINs, b02, could be seen by these tests to increase in thickness. Another PIN, a19, was very stable, and another b20, actually showed a decrease in dead-layer.

The dead-layers and energy resolution of several PINs were also compared before and after attempts at annealing the PINs. This was a test of possible radiation damage

	Dead-Layer Thickness (μg/cm^2)					
PIN	1/95	3/96	4/97	6/97	9/97	5/98
o05			32			
o11				18		
a06	17					
a10	21					
a11				38		
a19	44		44		35	
b01		≈20				
b02		≈20	40	39		
b03	≈20					
b04	≈20					
b05	≈20					
b06	≈20					
b20			41	38		20
b23						23
b30				53		

Table 4.7: Results of the PIN the dead-layer measurements described in table 4.6.

and defects contributing to the apparent dead-layer thickness or reduction of the resolution. To anneal each PIN, it was placed in a vacuum chamber and heated with a resistor. The temperature was stabilized with feedback from a thermocouple mounted onto the back of the PIN. In the tests described above, one PIN had an initial measurement indicating a thin dead-layer and upon remeasurement later appeared to be thick. This PIN was annealed to see if it would recover, but, unfortunately, it was damaged during a malfunction. The results are shown in table 4.8. One of the three PINs tested showed increased resolution and a slightly decreased dead-layer. These tests were done right before the last reactor cycle to determine if annealing all of the PINs would be useful and safe. Because the data were inconclusive, no more annealing was done.

Comparing proton energies at different acceleration voltages showed that for each increase of 1 kV the proton energy increased on average only 0.5 keV. This is not, however, due to a loss of gain, but instead is largely due to the effect of the soft threshold. The soft threshold tends to make peaks appear higher, an effect that decreases as the peak moves away from the threshold. Figure 4.10 shows the results of a study of this effect. In this test, the amplitude of the pulser signal input into the preamplifiers was varied and the effect on

	Thickness (μg/cm^2)		Resolution (FWHM/E)		Annealing Regimen
PIN	Before	After	Before	After	
a11	38	34	1.07%	0.77%	1 hr @ 80 °C
		35		0.76%	vented and repumped
b20	38	40	3.46%	3.39%	50 min @ 90 °C
b30	53	51	0.76%	0.93%	1.5 hr @ 65 °C, 1 hr @ 80 °C
		-		≈8%	2 hrs @ 100 °C

Table 4.8: Results of PIN annealing tests. The vent cycle in the second line was done to determine if the dead-layer reduction was due to loss of a condensed layer during the heating. In the last line, the 2 hours at 80 °C damaged the PIN.

the final peak position, amplitude and width were seen to be consistent with the predicted influence of the soft threshold.

In the last month of beamtime, two surface barrier detectors were installed in proton detector C. These were purchased with standard thicknesses of 150 μ and 300μ, and the specified dead-layers corresponded to about 5-10 keV proton energy loss. The thicker detectors requires a higher bias voltage (160 V) than the PINs, so it was underbiased for this test. Still they consistently measured much higher proton energies than the PINs. Figure 4.11 shows an example of proton spectra as measured in the surface barrier detectors and two PINs. With the increased noise-proton separation, the noise was successfully reduced by threshold adjustment without significant loss of the proton signals. Unfortunately, the surface barrier detectors died toward the end of the run (during unprotected sputtering, see section 4.2.5), and thus could not be tested offline and observed long-term. Since the surface barrier detectors measured proton energies well above the threshold, they were as not susceptible to the effect of the threshold on the peak position. The surface barrier detectors were not calibrated before they were destroyed, but an estimate can be made of the calibration assuming energy losses of 5-10 keV in the dead-layers. The increase in energy with increased acceleration then is seen to be as large as 0.93 keV/kV. Figure 4.12 shows the increase in measured energies as a function of high voltage. Also shown is a comparison of the rate of proton detection as a function of high voltage for the surface barrier detectors and for the detector as a whole. The detector rate increases with high voltage as the protons move farther away from the noise and the threshold. The energies in the surface barrier detectors, however, are sufficiently far from the threshold not to benefit from this added acceleration and remain at the beam-limited rate of ≈0.25 Hz. The proton

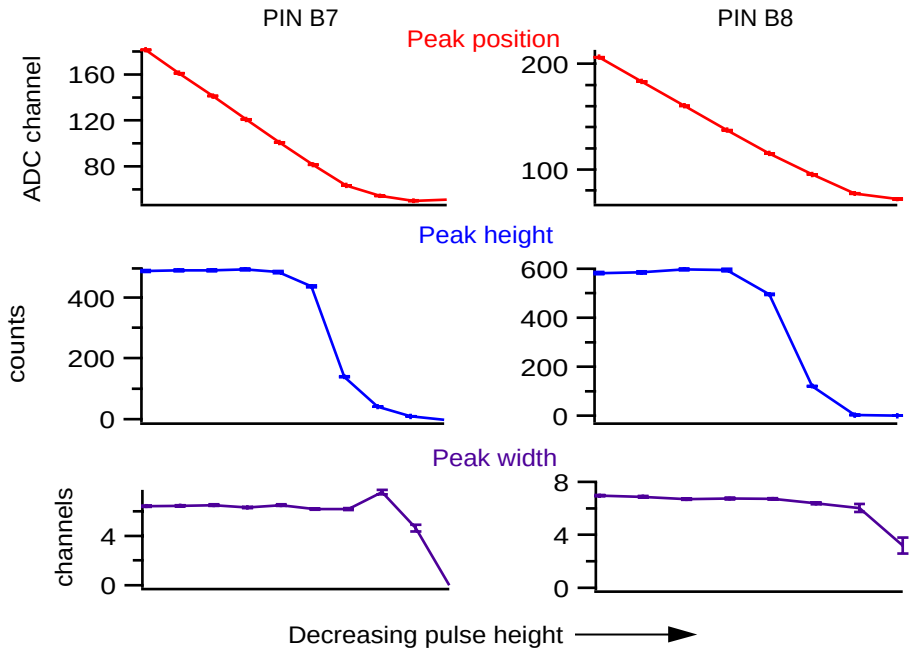

Figure 4.10: A pulser was used to test the effects of the soft threshold on the peak position. The pulse height was reduced in several steps by the same increment. Results are shown for two illustrative PINs. All of the singles spectra look like gaussians rather than a gaussian with one edge cut off as you would get with a hard threshold. Peak positions, widths (FWHM), and magnitudes are obtained by fitting gaussians to the peaks, and the errors shown are fit errors. As the peak gets nearer to the threshold, its magnitude decreases, and the distance between peak positions also decreases. This apparent ΔE, smaller than the real difference by a factor that can be larger than 2, could account for the observed proton energy shift with high voltage, $\Delta E/(e\Delta HV)$, always under unity.

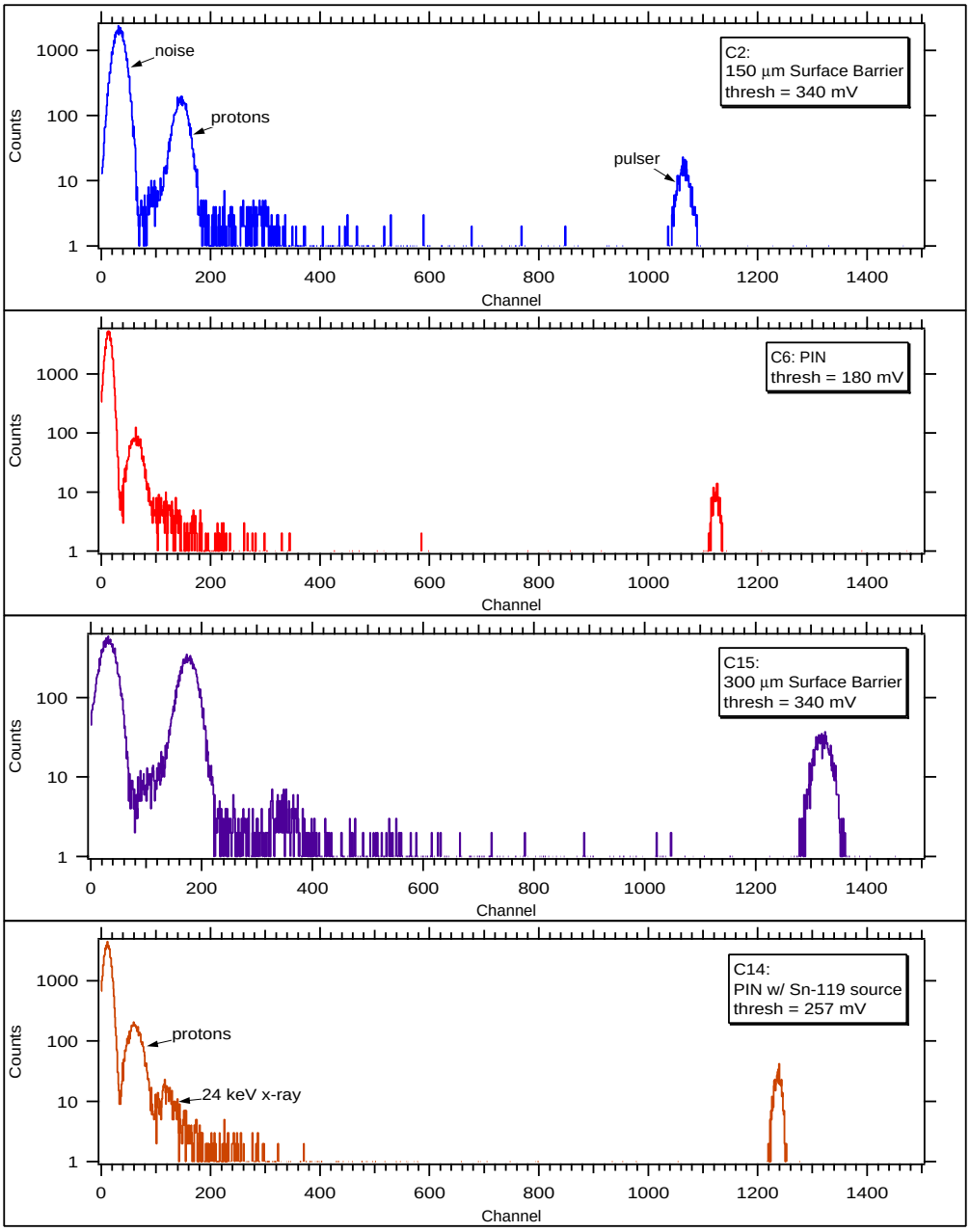

Figure 4.11: Proton singles spectra from series 113. Electronics noise, proton peaks, and pulser peaks can be seen in all spectra. The spectra from the surface barrier detectors, C2 and C15 show much better separation of the proton peak and the noise. This is not due simply to a gain increase, which would also affect the pulser position. The poorer resolution of C15 results from operating the detector at half its rated bias voltage so that it could be powered in the same circuit as the PINs.

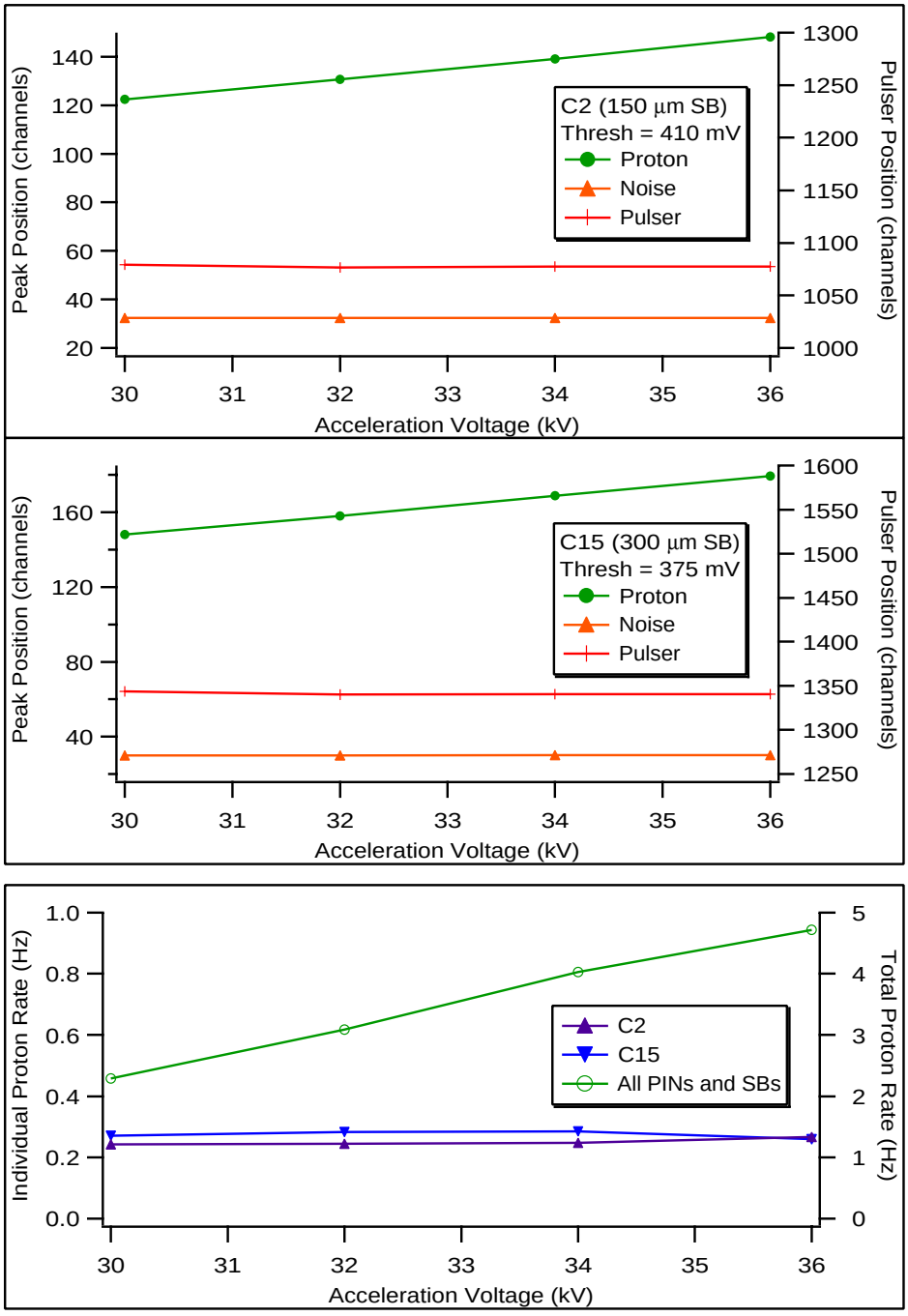

Figure 4.12: Energies and proton rates in the surface barrier detectors versus acceleration voltage. The increase in energy is close to 1 keV/kV. While the total proton rate improves with increased high voltage, the surface barrier rates remain constant, since its rate is beam-limited even at 30 kV.

energies measured in these detectors did not change over 15 days of operation, indicating that there was no significant buildup on these detectors in this period.

During the last round of detector repairs, it was found that all of the 50 Ω protection resistors (see section 4.2.5) had become become damaged. Two resistors were in the kΩ range, and the others were 55-100 Ω. These increases in the resistance had resulted in loss of gain. This detector and another had new resistors installed, a third was found to have all resistors less than 60 Ω, and the fourth could not be checked because of time constraints.

4.2.4 Cooling

Several steps were taken during the run to improve the cooling capacity, stability, and uniformity of the cooling system. The first cooling system used a Neslab CFT-25 recirculating chiller with a minimum set point of -10° C. During operation of the full detector, the coolant bath temperature was near 0°C, indicating PIN and preamplifier temperatures of 20-40°C. Cooling the PINs and preamplifiers to 0°C is necessary to reduce the electronic noise. A Neslab ULT-95 chiller with a minimum -90° C set point (rated to 340 Watts at -80°C) also failed to cool to this target temperature.

The next attempt involved using liquid nitrogen as a coolant, fed into the cooling lines from a dewar regulated by a needle valve. This system had the desired cooling capacity: the temperature at the cooling outlet was measured to be -60°C. It did not, however, have the desired stability. The needle valve required constant attendance. It often froze and also needed to be adjusted at least once an hour to get the desired pressure. Too little pressure gave inadequate cooling and too much pressure was potentially dangerous to the cooling lines and rapidly depleted the dewar.

The temperatures reached in these cooling scenarios differed by up to 50°C among different proton segments and by smaller amounts within a segment, leading to differing rates of electronic noise. The cooling capacity of the nitrogen gas decreased as it passed, and was warmed by, each of the four proton segments. The steel housings of the diode array (the HV electrodes) had temperatures that increased in the order of their connection in series: B,A,C,D. To cool the system adequately required cooling the first detector to close to liquid nitrogen temperature. This was undesirable because the electrodes showed an increased tendency to spark when this cold. The variations in temperature due to variances in the

heat load (different number of instrumented channels) and to variances in the conductivity of the internal cooling connections were at times greater than the variances due to the series cooling. Measurements of the PIN leakage currents on 3/31/97 gave values of i_A=11 nA, i_B=17 nA, i_C=3 nA, and i_D=25 nA. Variations in PINs and other leakage resistances could also have contributed to these differences.

The finite conductivity of the copper cooling system also lead to nonuniformity within a proton detector segment. Additionally, the system was under mechanical stress due to the rigidity of the connections and the pressure of the tightly packed components. Twice the indium seals between two copper connections were loosened during assembly. When the preamplifiers were powered the epoxy between the hybrids and the copper heat sinks expanded and broke the connection. Once the connection was broken the hybrid quickly burned up. Midway through the run, a major redesign with flexible connections was implemented to relieve some of the mechanical stress.

During the final reactor cycle, an automatic system with a PID controller was implemented to regulate the flow using a thermocouple on one of the proton detectors to sense the temperature. This thermocouple, mounted on the low-voltage side of the ceramic break in the cooling system, typically measured -170 ° C with this system. This temperature, well below that necessary to reduce PIN leakage current, was maintained to inhibit the HV emission. The controller also periodically reversed the direction of the nitrogen flow to reduce the asymmetry in temperature among the proton segments. This system was stable enough to run unattended for 5-6 hours, and used an average of 1.5 160 liter dewars each day, roughly half as much as the needle-valve regulated system.

4.2.5 High Voltage

The 20 keV energy loss in the PIN dead-layers made it necessary accelerate the protons through the highest voltage possible. Figures 4.12 and 4.13 show the results of several tests of decay proton detection rate as a function of high voltage. At the normal operating voltage of 36 kV, the electrodes were highly unstable. Polishing and conditioning over many weeks made it possible for them to hold as much as 38 kV for a short period - less than one day. At 36 kV, there were from 2 -20 sparks each day. The electrodes also displayed the emission described earlier even when stable. The tendency and size of the sparks and the rate of emission were very sensitive to vacuum pressure and temperature, as

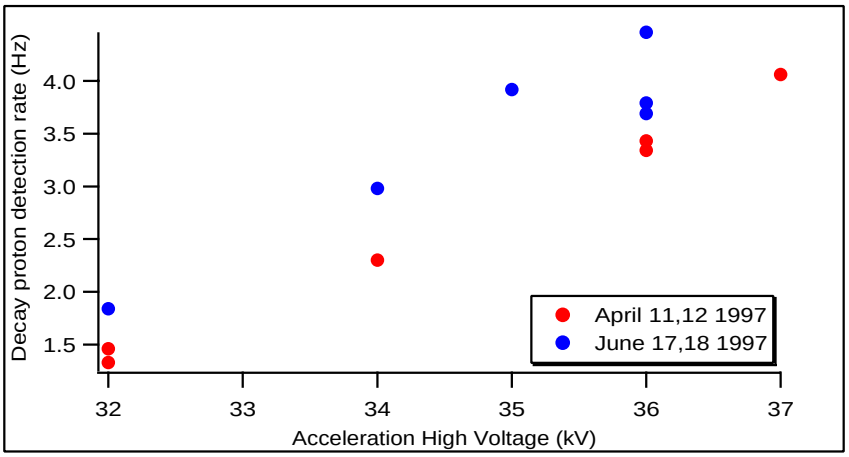

Figure 4.13: Two tests of decay proton detection rate were made during the run, one in April 1997 (series 56 to 59) and another in June 1997 (series 92 to 95). Shown above are the deadtime-corrected rates. The April tests had typical deadtimes of 10%, and in June the deadtimes were 40-65%. The increase in detection rate with increase in voltage does not appear to be diminishing even at 37 kV. In series 95, however, the rate (at 36 kV) did go as high as 8 Hz as the cooling improved. The expected decay coincidence rate in the full detector is near 10 Hz.

well as other factors we could not identify. Many of the sparks were between the electrodes and the ground plane between the electrode and the beam. After many weeks of running, the inside of this ground assembly had regions of brown discoloration. These discolorations were seen in locations nearest to the rims of focusing tubes and also near several spots where the tops of screws securing the focusing plate were not entirely flush with the plate surface. Sparking is most likely to occur in regions such as these where the surface is least smooth and thus the electric field the strongest. Replacing and sanding these screws was effective in preventing sparks from these points. The focusing tubes and the rest of the electrode were polished on several occasions with some success. Because each spark was a danger to the electronics and also caused a drop in voltage, an electrode with persistent severe sparking could not be used. Much of the data were taken with only 2 or 3 proton segments because the other(s) did not respond to prolonged conditioning, sparking at least once an hour or sometimes every few seconds. During these periods, the efforts were continually made to address this instability get the problematic detectors operational again.

All proton detector electrodes were reconditioned after being exposed to air. Electrodes rendered inoperable by voltage instability or unacceptable emission levels were cleaned either by hand polishing offline, or by sputtering inside the chamber. The sputtering pro-

cess cleans the electrodes with ion-bombardment. The chamber is filled with 10 mtorr of argon and between 1 and 10 kilovolts are applied. This worked very well in several cases, reviving several proton segments whose stability had been destroyed by several large sparks and could hold less than 10 kV. The sputtering process discolored the PINs, leaving dark spots 3 mm wide at the center of each. However, no change in response was found for these PINs. A later attempt at sputtering was not successful.

The larger sparks (>100 μA) often disabled data acquisition, tripping the PIN bias supply or the power to the electronics in the high voltage rack. Often there was grave damage to the electronics in the detector, or to the components in the rack. The shaper/ADC boards were the most susceptible, and although they were continually modified for greater spark protection, more than 20 were lost during the run. Sometimes there were not enough shaper/ADC channels to instrument the PINs. Sparks also destroyed several VME modules and a NIM power supply. 50 Ω resistors were added on the preamplifier output to protect the preamplifiers from spark damage. Better grounding of the VME boards was very helpful in protecting them from damage. The outer conductors of the BNC inputs were initially connected to ground through the board's ground plane connection to the VME bus. Tying the BNC plugs directly into the front end of crate chassis provided a shorter, and less dangerous path for spark-related currents. Previously the chip most often destroyed during a spark was the one closest to the path connecting the front end ground to the VME backplane ground. High voltage leakage currents also found paths along the PVC shields on the ends of the proton detectors and along the glass and ceramic stand-offs supporting the inner conductor. Periodic cleaning, sanding, or replacement of these components reduced these currents. High leakage currents traveling through the air inside the PVC shields were also observed during periods of high humidity. A quick spray of dry air into the shield immediately reduced this current.

In the first half of the run, the background due to emission was not significant. The aluminum-wrapped beta detectors showed no noticeable increase in rate with high voltage, and the extra background in the PINs was much less than the electronic noise. In the second half of the run, the emission rates increased dramatically. The phototube voltage was applied incrementally and halted when the emission-related background rate went above 20 kHz. The high emission rates were often correlated with a very large HV leakage current (1-10 μA) (although at times the leakage current was external and did not cause background). Most likely this was due to fluxes of x-rays so large as to compensate

for their poor detection efficiency. Also, the beta detectors were not light-tight internally, so any visible glow discharge inside the chamber could be reflected into the scintillator or guide and down to the phototube. The rate of emission-related background in the beta detectors decreased with an increase of pressure as shown in figure 4.14.

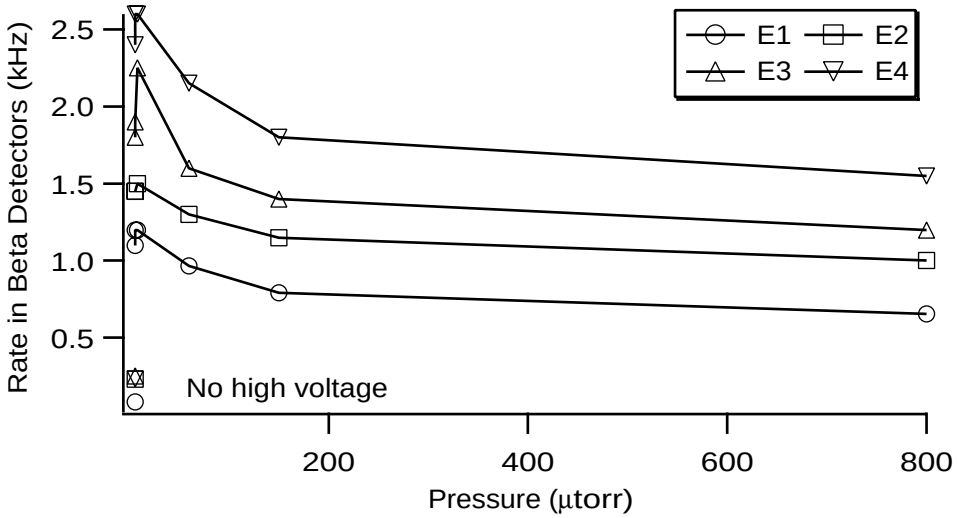

Figure 4.14: Emission-related background rates in the beta detectors at varying vacuum pressures. Except for the points labeled "No high voltage" all measurements were made at 36 kV. The pressure was not changed monotonically in order to avoid measuring a trend that is actually drift over time. (Data taken 7/25/97.)

High rates of emission-related background in the beta detectors was usually accompanied by high rates of up to 1 kHz in each PIN. Much of the emission-related background was measured to have the same energy as the protons. The emission-related background was almost entirely eradicated in a test in which the proton detectors were covered with plastic wrap. This test indicated that the primary emission products being detected were charged particles, not x-rays. It is believed that these were protons created by hydrogen ionized near an emission point. Perhaps these are protons created when the field emission electrons strike the stainless steel ground assembly. These protons are then accelerated towards the PINs. This is an unfortunate type of background since it cannot be reduced by a threshold adjustment during the run and cannot be rejected in analysis on the basis of energy value since the background is at the same energy as the neutron decay protons.

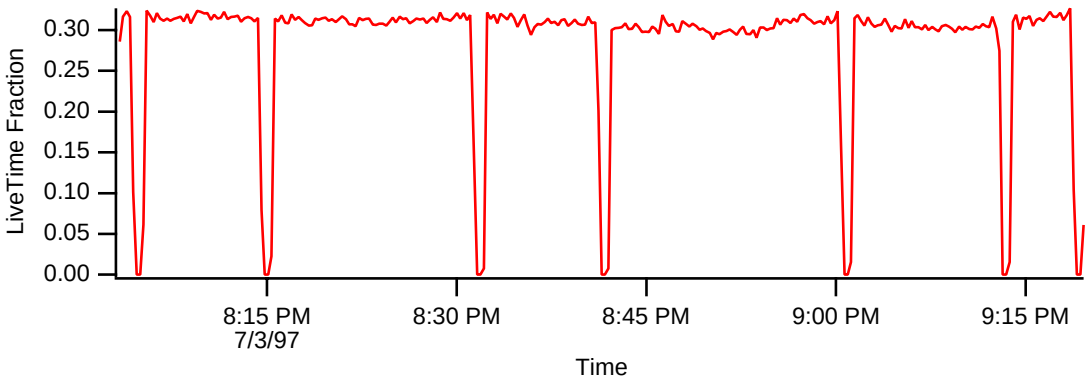

Figure 4.15: Livetime plot of file s106r015 showing dead periods when the DAQ is locked up awaiting a reset.

4.2.6 Data Acquisition

During the run, several changes were made to the data acquisition (DAQ) system, primarily to reduce the large deadtimes in coincidence data taking. The event trigger logic was rewired in April to accept only coincidences rather than any proton event. With the initial configuration, the deadtime per event was 0.6-1.5 ms, and proton rates of over 1 kHz lead to sizable deadtimes (see figure 5.1). The shaper/ADC boards were modified to include a front-end fast-clear input, allowing the trigger to be changed to accept only coincidences. The deadtime remained high, however, since the rates increased as more of the detector became operational, and thresholds were lowered when possible to accept more decay events. The deadtime per event increased to 3 ms after series 83 when delay was added in the code to prevent failures believed to be associated with the CAMAC communication module's limited speed. In July, the coincidence window was changed from 14 to 7 μs, involving an acceptable loss of background data. At times the DAQ suddenly stop accepting events and could be revived with a reinitialization of the CAMAC crate. A "reset everything" procedure was added to the code to enact such a reset after 15 seconds with no trigger. An example of a run with many resets is shown in figure 4.15. However, the most likely failure mode was associated with sparks and required human intervention. A plot of the livetime percentage versus written event rate (see figure 4.16 is useful in illustrating the effect of these changes and of other subtleties in the DAQ.

The Phillips 7182 TDC gave spurious data 1-2% of the time. Two gate and delay

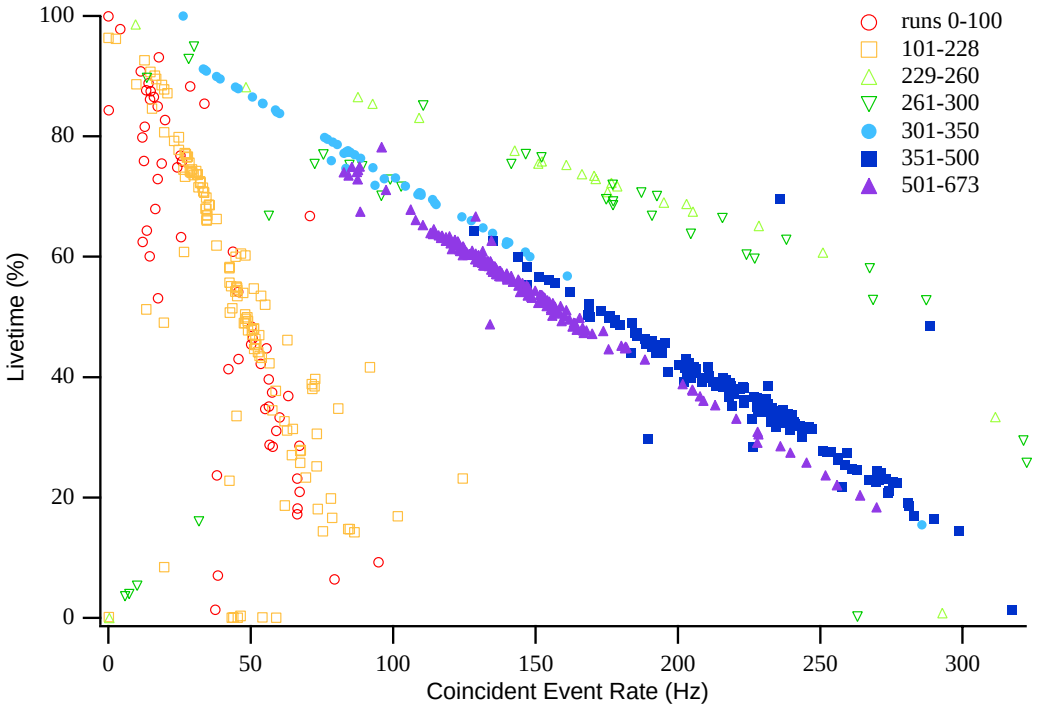

Figure 4.16: The livetime percentage shows several trends throughout the physics run. It often was quite low, since the event readtime was as large as 3 ms. Before run 229 the slope is very steep because non-coincident proton events also incurred a full event read, although the event was not stored unless a beta detector fired. Thus in the early files the livetime is linear in coincidence rate only to the extent to which its proportional dependence on the proton singles rate did not vary. This is true to the extent to which the majority of coincidence events are accidental coincidences rather than real decays or correlated background. The second trend shows a much shallower slope correlated with the installation of liquid nitrogen cooling. This greatly reduced the low-energy background, increasing the fraction of proton events in coincidence. However, the slope increased near file 300 due to changes made in the DAQ code that added a delay in the read cycle to improve acquisition stability, thus increasing the readtime per event.

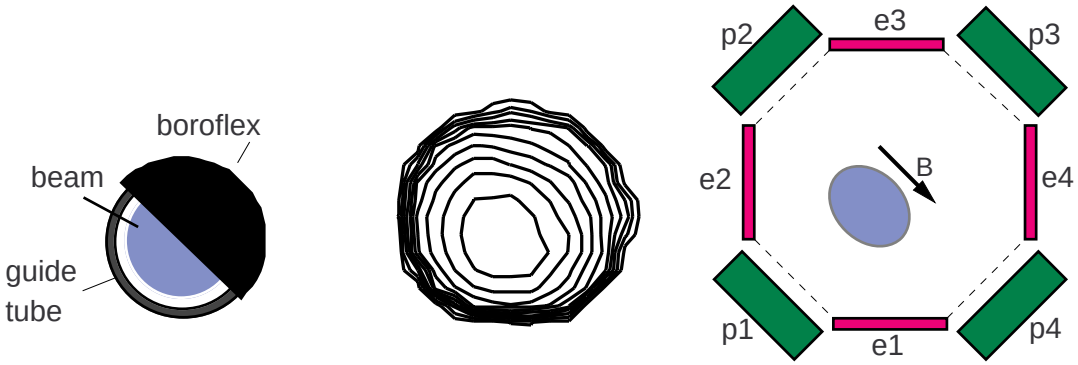

Method of beam blockage just downstream of the spin flipper.

Results of beam profile scan of blocked beam.

Geometry of beam and field in detector region.

Figure 4.17: To induce a large false D-coefficient, an asymmetric transverse polarization was induced by rotating the guide field to point to one proton segment and blocking half of the beam so that there was a net displacement perpendicular to the polarization direction.

modules (a LeCroy 222 and a Phillips 794) were replaced during the run, and others showed some drift in gate length. An initial asymmetry in the time spent in each polarization state was traced to a faulty gate and delay. The discriminators also showed drifts in threshold of up to 10 mV. For two weeks an important inhibit cable in the beta detector NIM logic was loose, allowing some beta detection energy data to be lost.

4.3 Forced-Systematic Measurement

As a test of the analysis, the beam configuration was modified as shown in figure 4.17 to induce a false D-coefficient large enough to be measured in a short period. The guide field was turned off and the sine coils were used to create a field pointed toward proton detector D, perpendicular to the neutron travel. Half of the beam was blocked upstream with a semicircle of borated rubber attached to the end of guide tube 2 just past the spin flipper.

To achieve a precision of 2% on the predicted false D, data were taken for almost a week with these modifications. The analysis of this data will be discussed in Chapter 5. During the final beam measurements, the blocking configuration was recreated, and the beam profile measured. The density contour showed the beam to be still highly symmetric after collimation, with a centroid displaced by 1.1 mm from the detector axis.

Chapter 5

Data Analysis and Results

During this first run, over one billion coincidence events were collected, but only a small fraction of these are the neutron decay events needed to determine the D-coefficient. The first step of the analysis is selection of a data set with the maximum number of neutron decay events consistent with the smallest number of background events. The selection criteria described below use timing and proton energy information with a simple figure of merit. Data taken under poor operating conditions are rejected.

The second step of analysis is the determination of D and the statistical and systematic uncertainties. In this experiment, the efficiency varied significantly among the diodes and over time. The determination of D under these conditions is quite complicated. Nonuniformities also increase the sensitivity to various systematic effects. To assess the magnitude of the various systematic uncertainties, each contribution is estimated with analytic arguments and simulation, and tested against the data.

5.1 Data Format

There were 667 data runs, totalling over 50 GB of data on 81 compact disks. Each file is assigned a series number and run number; s090r002 for example indicates series 90, run 2. The data in each of the 126 series were taken with the same proton acceleration voltage, the same configuration of the data acquisition code or logic, and the same configuration of the proton detectors and electronics. Changes of individual thresholds on the PINs did not normally justify a series change. Each run is a continuous data taking period, generally under 4 hours.

Dispersed within each data set are monitor events recording the experimental conditions. Figure 5.1 shows the entire run history of several of these conditions; event rate, livetime, high voltage leakage current, and PIN leakage current. (The livetime fraction is defined as the fraction of time the data acquisition system is waiting for the next event. Deadtime is the time the DAQ spends processing each event. Livetime = 1 - deadtime.) Figure 5.2 shows the number of operational PINs for each data series.

5.2 Event selection

Protons from neutron decay have a maximum energy of 750 eV, corresponding to a maximum velocity of 4×10^7 cm/s. The shortest time a proton takes to travel the 7 cm from the edge of the beam to a detector is 0.2 μs, while the electron reaches a detector in less than one nanosecond. The greatest number of protons are detected 0.5 μs after the electrons. The delayed coincidence is used to identify the neutron decay events. One useful way of displaying the data is to plot proton energy versus proton-beta relative time as shown in figure 5.3. The position of the prompt background peak defines zero relative time. Background is subtracted from the total number of events in the delayed-coincidence or"drift-time" window by counting events in other regions of the proton-beta relative time spectrum where there can be no real neutron decay events.

5.2.1 Determination of the Offset in the Proton-Beta Relative Time

The relative arrival time of the proton and beta particle in each event is measured with the 14 μs-range TDC. The position of the "prompt" background peak, corresponding to simultaneous beta particle and proton detection, is offset from zero in the TDC range, and this offset is subtracted from each TDC value to calculate the true coincidence time. The offset has a different value for each PIN-beta detector pair due to differences in hardware delays. The beta signal delays are set manually with a potentiometer on one of the gate generators and differ slightly among the four beta detectors. The delay between arrival of the proton at a PIN diode and generation of the "conversion" logic pulse also varies among shaper/ADC boards and among the channels on a board. The difference in the delays varied up to 0.3 μs between beta detectors and up to 0.5 μs between PINs to create spread as large as 450 channels between the locations of the prompt peaks in a single file. The prompt peak is cleanly recognized by gating on proton energies above channel 300 in the

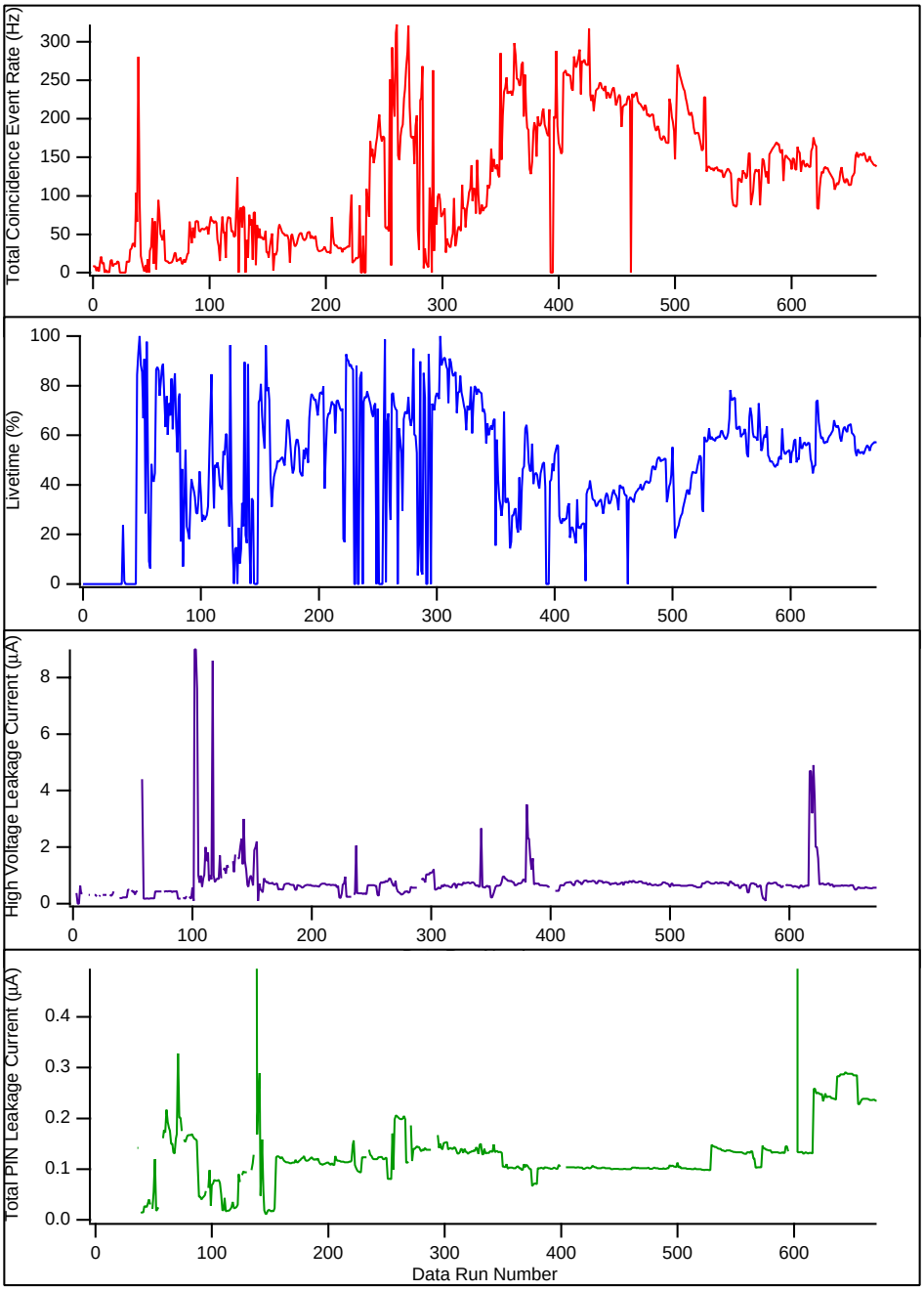

Figure 5.1: These graphs show the values of several monitored parameters over the entire period of data collection. The coincidence rate, which is dominated by accidental background, is limited to approximately 330 Hz by the speed of the event read, and is highly correlated in this way to the livetime. (Deadtime-corrected rates were as high as 1 kHz.) The high-voltage leakage current is not highly correlated to other experimental conditions since it was often high due to external leakage currents, especially along the PVC shielding. The PIN leakage current is most sensitive to the number PINs that were operating at a given time and to their temperature.

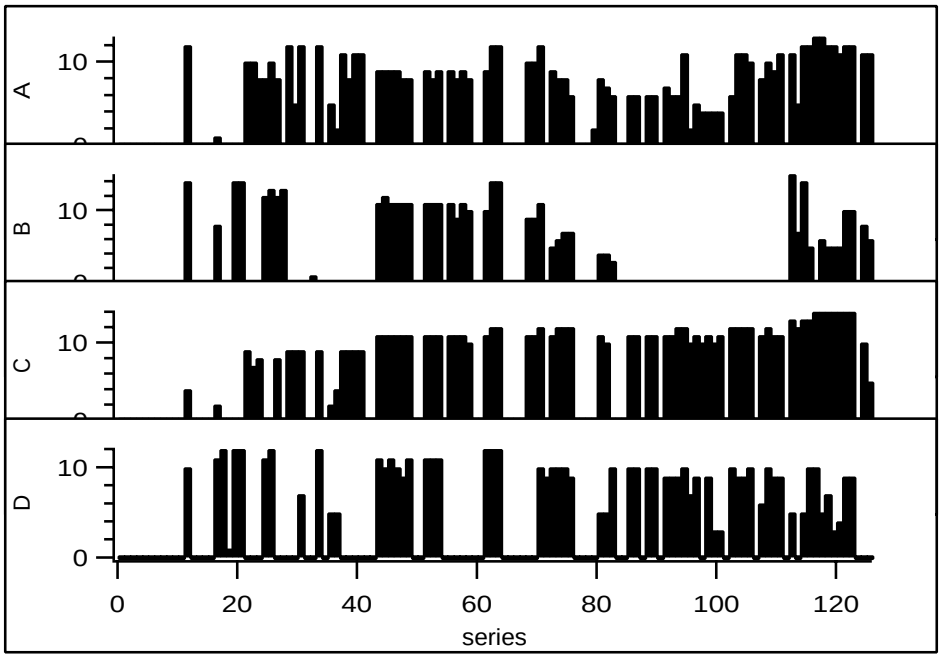

Figure 5.2: The number of functioning PINs in each proton detector varied from series to series. A functioning PIN is defined as one showing a positive rate of detection of decay protons. (Series with no operational PINs are series for which no good data were taken. Usually these were brief runs during a test or repair period.)

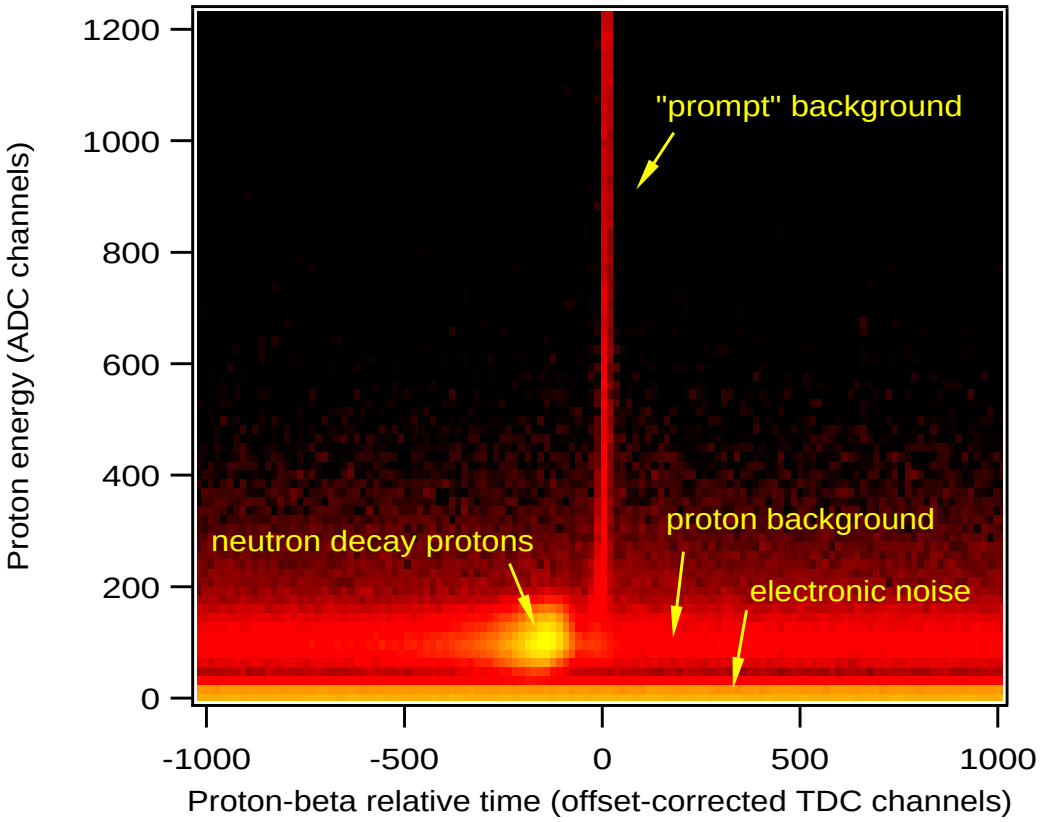

Figure 5.3: An image plot of proton energy versus coincidence time shows several distinct characteristics. At the lowest energies the electronic background is detected as accidental coincidences over the entire time spectrum. In a slightly higher energy band are protons, which also appear as accidental coincidences, but show an enhancement at delay times greater than 0.2μs, corresponding to the minimum beam-to-detector drift time of the neutron decay protons. This appears at negative time because the proton signal serves as the start for the TDC and the delayed beta particle signal the stop. We define zero coincidence time as the position of the prompt background peak, which extends to high energies in the proton and beta spectra. These data are from series 90.

PIN ADCs. This excludes real protons from the spectrum, resulting in a spectrum with only one major feature with a FWHM of 2-5 channels as shown in figure 5.4. Offsets vary among data series due to changes of shaper/ADC channels, yet when the hardware is not changed they are stable to within a few channels.

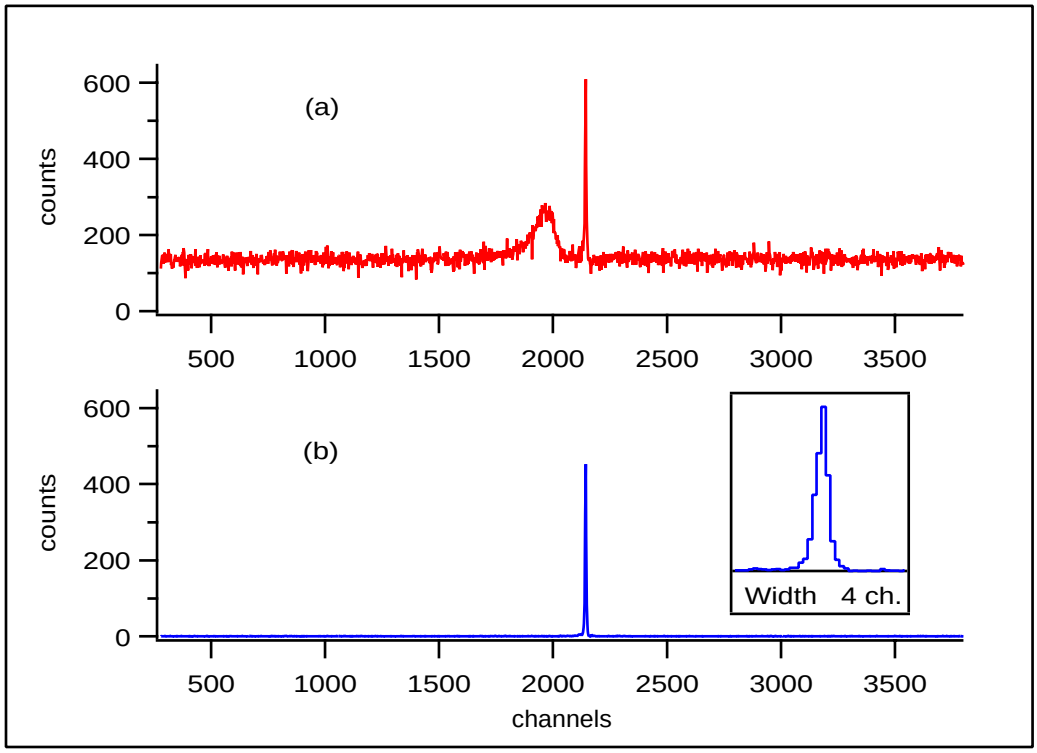

Figure 5.4: To find the position of zero time (the TDC offset) in the proton-beta relative time spectrum (a), the prompt peak is located for each PIN-beta detector pair for each run. This is facilitated by rejecting events with proton energy below channel 300, resulting in a time spectrum like (b). Shown are the relevant spectra for PIN A5 and beta detector E3 in series 90.

5.2.2 Timing Windows

The timing windows used to measure delayed coincidences and accidental background are set by eye. All windows are sufficiently distant from the prompt peak to avoid small tails, and windows for estimating background rates are chosen as shown in figure 5.5. These windows varied over time (see figure 5.6) to respond to changes in the data acquisition and background. We define N_{ON} as the total number of events in the drift-time window, and N_{OFF} as the total number of events in the two background windows.

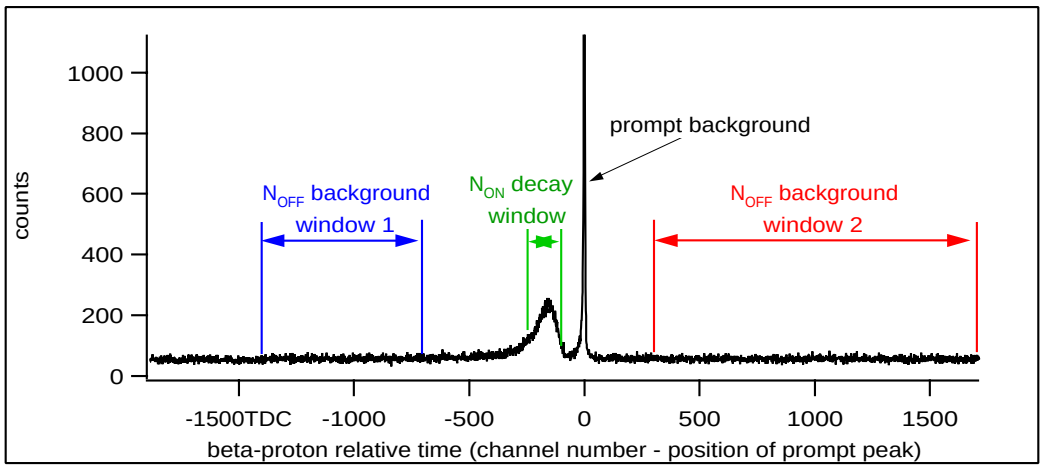

Figure 5.5: Time windows used to find the signal and estimate the background. The "ON" window contains the decay coincidences and the "OFF" windows contain accidental coincidences.

5.2.3 Proton Energy Cuts

The variance in gain and count rate from PIN to PIN and run to run makes an energy cut based simply on predicted spectral shapes problematic. During the final reactor cycle when the majority of the decay events were collected, very few of the installed PINs were those that were installed during calibrations, owing to frequent replacement of PINs and ADC boards. The simple procedure described below produces carefully chosen upper and lower bounds event selection by proton energy, maximizing the statistical precision.

The number of decays is estimated by taking a difference (Δ) between the number of events having a relative time in the delayed-coincidence window (ON) and events in the background window (OFF) of the TDC spectrum.

$$N_\Delta(\beta, PIN, spins, runs, pADC) = N_{ON}(\beta, PIN, spins, runs, pADC) - sN_{OFF}(\beta, PIN, spins, runs, pADC). \quad (5.1)$$

Here s is a scale factor accounting for the different widths of the ON and OFF windows.

With no background ($N_{OFF} = 0$), the fractional statistical precision of N_Δ would be

$$\frac{\sigma_{N_\Delta}}{N_\Delta} = \frac{\sigma_{N_{ON}}}{N_{ON}} = \frac{1}{\sqrt{N_{ON}}} = \frac{1}{\sqrt{N_\Delta}}. \quad (5.2)$$

With background coincidences the statistical error is the quadrature sum:

$${\sigma_{N_\Delta}}^2 = {\sigma_{N_{ON}}}^2 + s^2{\sigma_{N_{OFF}}}^2 \quad (5.3)$$

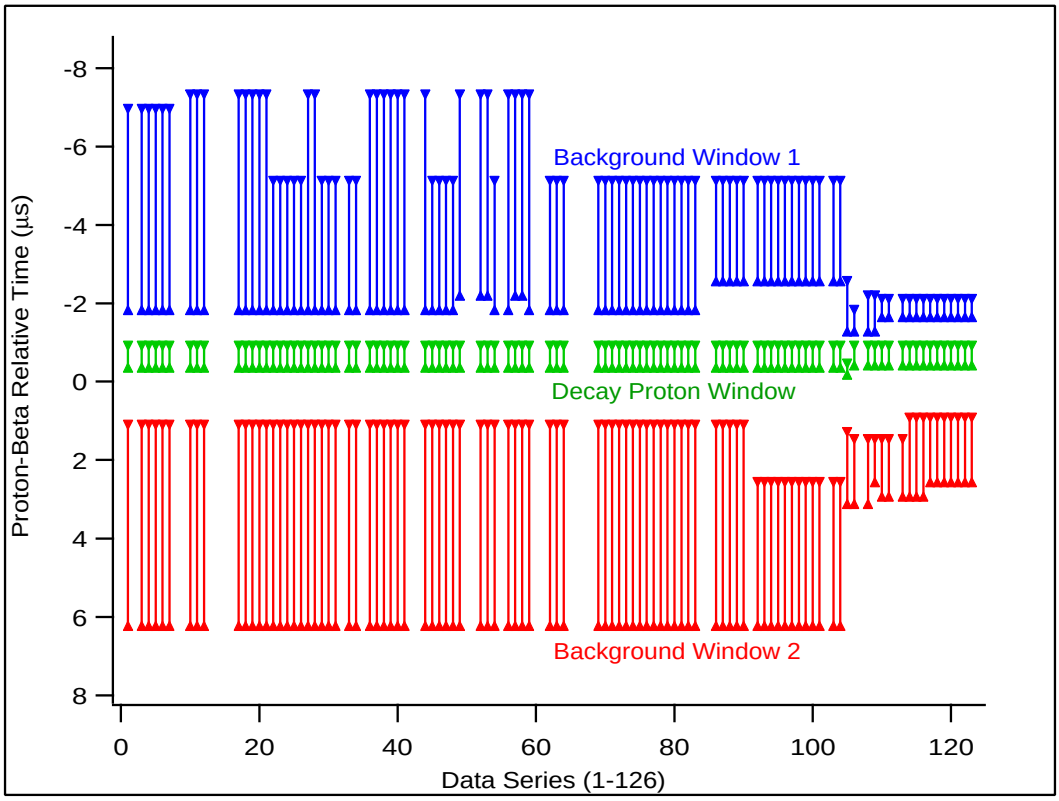

Figure 5.6: Time windows used for this run's data. The windows are placed in regions where the background appears most flat. The sharp change after series 105 is due to the reduction in the coincidence window that was made to reduce deadtime.

However, with a large background window, s and $\sigma_{N_{OFF}}/N_{OFF}$ are small, and the error on N is

$$\frac{\sigma_{N_\Delta}}{N_\Delta} \approx \frac{\sqrt{N_{ON}}}{N_\Delta} = \frac{\sqrt{1+1/f}}{\sqrt{N_\Delta}}, \tag{5.4}$$

where f is the signal to background ratio. This fractional error is minimized when optimizing the time cuts. The approximation is useful for assessing backgrounds, but the final calculation uses the exact errors.

For each data series, corresponding to consistent running conditions, the effect of varying the lower proton energy bound (LB) is investigated. The quantity $\frac{\sigma_{N_\Delta}}{N_\Delta}(PIN, LB)$ is computed for the sum of all events in a given PIN. The neutron spin state and the identity of the beta detector involved in the coincidence event are both ignored in this sum.

$$N_\Delta(PIN, LB) = \sum_{\beta} \sum_{spins} \sum_{runs} \sum_{pADC=LB}^{pADC_{max}} N_\Delta(PIN, \beta, spins, runs, pADC) \tag{5.5}$$

$$f(PIN, LB) = \frac{N_\Delta(PIN, LB)}{sN_{OFF}(PIN, LB)} \tag{5.6}$$

The lower bound is chosen to minimize $\frac{\sigma_{N_\Delta}}{N_\Delta}$ (see figure 5.7). The upper bound (UB) is found by an analogous procedure, minimizing $\frac{\sigma_{N_\Delta}}{N_\Delta}(PIN, UB)$.

$$N_\Delta(PIN, UB) = \sum_{pADC=LB}^{UB} N_\Delta(PIN, pADC) \tag{5.7}$$

The upper and lower bounds are verified by checking that the decay proton energy peaks fall between the bounds. If there are sufficient data to find the peak, the proton peaks in the subtracted (Δ) spectra are fit to a gaussian. Figure 5.8 shows an example of how this results of this verification procedure for one PIN over the entire experiment.

The raw data contain 15 million decay events; 18 million background events in the delayed-coincidence window (ON) must be subtracted. Using proton energy to reject events reduced the subtracted background to 6 million, with a negligible loss in real events.

5.3 File Rejection

Occasionally poor experimental conditions rendered data unusable, usually due to a malfunction of some part of the apparatus. These runs were rejected. They are listed along with the reasons for rejection in Appendix C. Data were also ignored in some of the

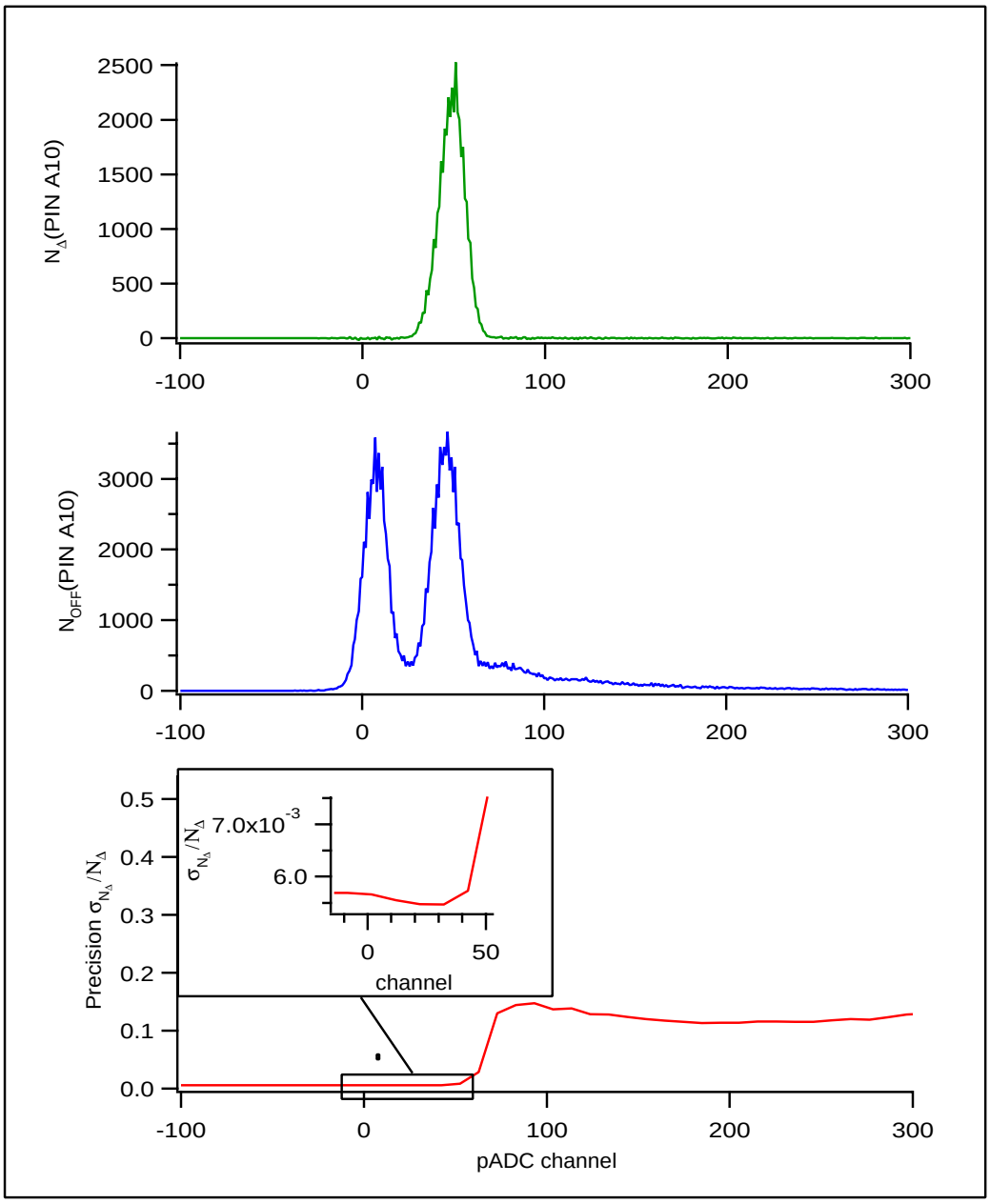

Figure 5.7: Dependence of the statistical precision on event selection using proton energy. The lower bound (LB) is chosen to maximize the statistical precision of the number of decay events counted. Shown are the background-subtracted proton spectrum (N_Δ) and the accidental background spectrum (N_{OFF}) for PIN A10. In both cases a sum has been taken over spin states, beta detectors, and all runs in series 90. Also shown is the fractional precision as a function of the lower bound value. The inset shows the region where σ_Δ/N_Δ has a minimum. The value of LB for this point is that used to cut the data.

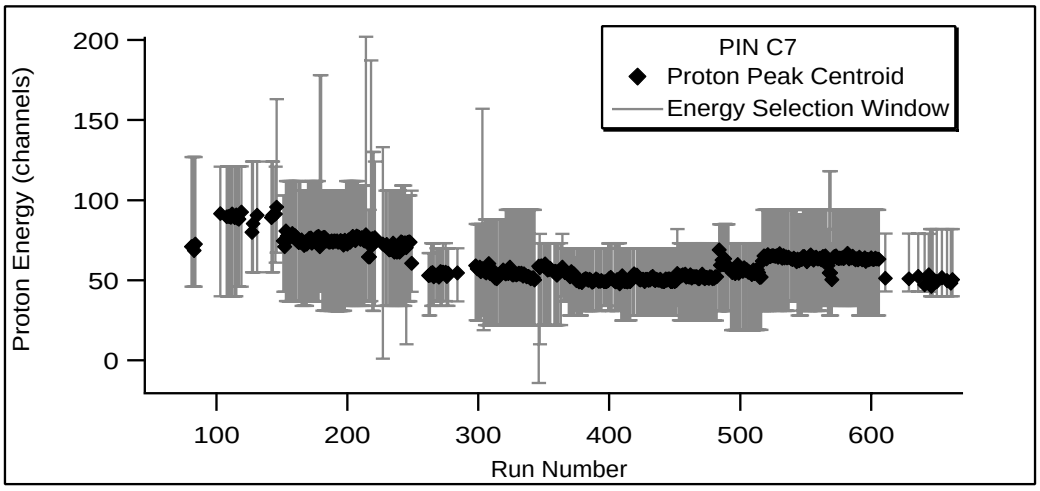

Figure 5.8: Decay proton energy centroids and event selection energy windows.

remaining files to correct a slight inconsistency in the numbers of background events for the two spin states. This inconsistency was traced to a fault in the data acquisition startup condition easily remedied by ignoring all events from the first spin flip cycle, and from any partial cycles at the end of a run. There also were occasional episodes of anomalously high or low rates of up to twice the average background rate. These episodes typically lasted from one to several cycles. Most were are explained by sparks. To avoid the systematic effects from these anomalies, all data in a full spin-flip-cycle portion were ignored if that portion of the data contained a statistically significant difference in rate. For each file, a cutoff rate difference was chosen so that one cycle (out of typically 1000-3000) would be removed purely from statistical fluctuations. This generally set an acceptance limit of within 3 standard deviations of the average rate. This process, which would have removed 0.1% of the events if the rates had purely statistical variations, removed 2.2% of all events and 1.7% of all flip cycles in the raw data.

5.4 Determining D

When obtaining the D-coefficient from the data, it is important to to consider the effect of the other spin-dependent correlations on the coincidence data. The beta and neutrino asymmetries parametrized by A and B (equation 2.3) are large and this leads to

possible systematic effects. With our detector geometry, these systematics are eliminated by a simple average if the proton detection efficiency is uniform. Unfortunately, the effective proton detection is not uniform and an alternative procedure is necessary.

The problem is most easily understood if we first investigate a single set of coincidence rates for one PIN diode and one beta detector as shown in figure 5.9, comparing the two spin states. In coincidence with a proton detection there is a neutron spin-beta momentum correlation of the form

$$(\frac{A}{E_e} - \frac{B}{E_\nu})\hat{\sigma_n} \cdot \mathbf{p_e}, \tag{5.8}$$

giving a preference for an electron going in the direction opposite the neutron spin. If we consider a single PIN at $z = z_{PIN}$ and one beta segment centered at $z = 0$, we see that the probability for coincidence detection is greater when the neutron spin points in the positive z direction.

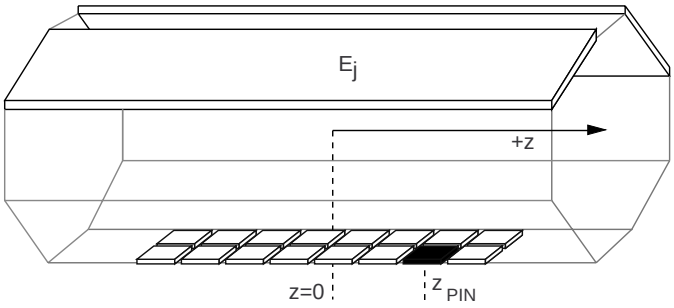

Figure 5.9: Geometrical detector asymmetry created when considering only a single PIN. The effect of the A and B correlations, favoring electron momenta opposite the neutron spin, makes detection of a decay more likely for neutrons in the -$\hat{z}$ spin state.

Quantitatively, we can express the coincidence probability as

$$N_{E_i PIN_j} = N_0 \epsilon_i \epsilon_j (1 + K_{A,i,j} PA + K_{B,i,j} PB + K_{D,i,j} PD) \tag{5.9}$$

The ϵ are detector efficiencies and P is the polarization. The K are geometrical factors derived from equation 2.3 integrated over the solid angles of the relevant beta detector and PIN. The K parametrize the effect of each term on the coincidence rates in the emiT detector. For a single neutron decay point, the K indicate the contribution to the coincidence rate in detectors i and j from each term in the decay probability.

$$K_{l,i,j} = \frac{\int_{E_i, PIN_j} G^2 F(E_e)(X_l) d\Omega_e d\Omega_\nu dE_e}{\int_{E_i, PIN_j} G^2 F(E_e)(1 + aX_a) d\Omega_e d\Omega_\nu dE_e} \tag{5.10}$$

$$X_a = \frac{\mathbf{p_e} \cdot \mathbf{p}_\nu}{E_\nu E_e}, \quad X_A = \sigma_n \cdot \frac{\mathbf{p_e}}{E_e}, \quad X_B = \sigma_n \cdot \frac{\mathbf{p}_\nu}{E_\nu}, \quad X_D = \sigma_n \cdot \frac{\mathbf{p_e} \times \mathbf{p}_\nu}{E_\nu E_e} \tag{5.11}$$

In the integrals, the necessary substitutions are made to express the constraints on the neutrino parameters as constraints on the proton parameters. For a continuous neutron beam, the K are integrated over the beam volume and density.

Monte Carlo simulation was used to determine these parameters. The Monte Carlo code incorporated the neutron event generator of E. Wasserman [40] an the CERNLib GEANT Monte Carlo package. All simulations assume unity polarization and the values of a=0.1, A=-0.118, and B=0.995. The emiT detector geometry is specified with uniform efficiency over the active area of each scintillator and each square focusing region of a single PIN. The beam shape and polarization direction can be varied. The coincidence events recorded for each beta detector and PIN diode include the electron energy. The values of K_D are obtained by fitting a line to the calculated $K_D D$ versus the value of D input into the simulation as shown in figure 5.10. In these simulations, the polarization was perfectly

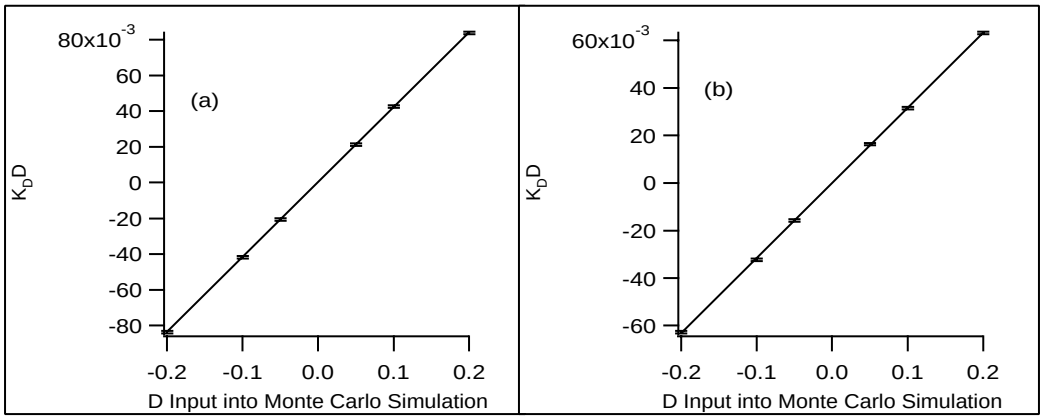

Figure 5.10: $K_D D$ vs. D_{input} from Monte Carlo simulation for (a) small-angle and (b) large-angle coincidences (see Section 5.4.1). The lines shown are linear fits.

aligned to the detector axis and the beam was given a uniform profile with a diameter of 6 cm. The K values for a given PIN differ in coincidence with the two opposite beta detectors because the average coincidence angles are different, slightly smaller or larger than 135°. The values of K_D are 0.419 $\pm$0.002 and 0.317$\pm$0.002 for the small and large-angle coincidences, respectively, with statistical errors from the simulation. Table 5.1 shows the magnitudes of the sum of $AK_A + BK_B$ from the Monte Carlo. If the values of K were known precisely, D could be extracted from any combination of proton and beta detectors.

PIN z-position (cm)	Small-Angle Coincidence	Large-Angle Coincidence
±14	∓.045	∓.047
±10	∓.029	∓.030
±6	∓.016	∓.017
±2	∓.006	∓.003

Table 5.1: Monte Carlo estimates of $AK_A + BK_B$. The difference between the two values at each z-position are due to the dependence, introduced through the a-correlation, on the cosine of the electron-proton angle.

However, the exact value of the calculated K is sensitive to the accuracy in modeling the detector geometry and polarized beam. Rather than use the simulations to calculate the systematics from A and B, the analysis procedure reduces the sensitivity to A and B. This is accomplished by extracting from the data a quantity (in this case a ratio) that depends on D, but is unity when D is zero.

If the effects of A and B were integrated with uniform proton detection, systematic deviations would sum to zero.

$$\sum_i \epsilon_i (AK_{A,i,j} + BK_{B,i,j}) = 0 \text{ for } \epsilon_i = \epsilon \tag{5.12}$$

For the actual emiT data and varying ϵ_i, a ratio is constructed with data from pairs of PIN diodes at the same z-position in a proton segment, exploiting the symmetrical placement of the two PINs to cancel the effect of the spin asymmetries.

5.4.1 PIN Pair Calculations

As noted for a single PIN, there is a significant effect on the coincidence rates from the A and B correlations. Now consider two PINs, which we label PINa and PINb, at the same z-position in a proton segment as shown in figure 5.11.

Each PIN is displaced from $x = 0$, so the angles to the two beta detectors are slightly different. Considering PINa or PINb in coincidence with E1 and E2, there is a preference for coincidences in the positive spin state from the A and B correlations. For PINa and PINb in coincidence with the same beta detector, the preference for coincidences with positive neutron spin has a slightly different magnitude since the average angles, slightly

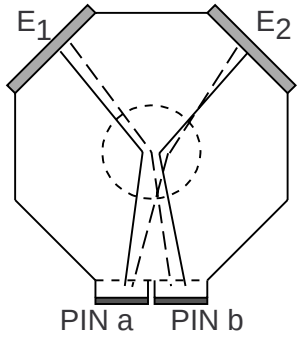

Figure 5.11: The data from two PINs at the same z-position in a proton segment can be used to cancel the effects of the beta and neutrino correlations. The coincidences shown by solid lines (E1,PINa and E2,PINb) have the same angle, a little less than 135°. These are referred to as "small-angle" coincidences. The "large-angle" coincidences for this pair of PINs (E1,PINb and E2,PINa) are the dashed lines.

greater or less than 135°, are not the same. Even for D equal to zero we have:

$$\frac{N^{\uparrow}_{E1,PINa}}{N^{\downarrow}_{E1,PINa}} \neq \frac{N^{\uparrow}_{E2,PINa}}{N^{\downarrow}_{E2,PINa}}. \tag{5.13}$$

For example, for a PIN pair at z=2 cm, these ratios are 0.988 and 0.994. We cannot use these four values to form the desired ratio. However, if we consider the small-angle ($< 135°$) and coincidences of two different PINs with these beta detectors, the angles are identical and

$$\frac{N^{\uparrow}_{E1,PINa}}{N^{\downarrow}_{E1,PINa}} = \frac{N^{\uparrow}_{E2,PINb}}{N^{\downarrow}_{E2,PINb}} \tag{5.14}$$

This relation follows from

$$AK_{A,E1,PINa} + BK_{B,E1,PINa} = AK_{A,E2,PINb} + BK_{B,E2,PINb} = C_{s,PINPAIRab} \tag{5.15}$$

where E1 and E2 are the two beta segments opposite the proton detector. We call this asymmetry $C_{s,a,b}$ for the small-angle. Similarly,

$$AK_{A,E2,PINa} + BK_{B,E2,PINa} = AK_{A,E1,PINb} + BK_{B,E1,PINb} = C_{l,PINPAIRa,b}, \tag{5.16}$$

for the "large"-angles, i.e. greater than 135°. In both cases, the contributions from A and B should be equal, the contribution from D should is opposite, and we can use the data to cancel the effect of A and B, leaving a measurement sensitive only to D.

For the smaller-angles, four quantities are measured.

$$N^{\uparrow}_{1,a} = N_0\epsilon_1\epsilon_a(1 + C_{s,a,b}P - K_DPD) \tag{5.17}$$

$$N^{\downarrow}_{1,a} = N_0\epsilon_1\epsilon_a(1 - C_{s,a,b}P + K_DPD) \tag{5.18}$$

$$N^{\uparrow}_{2,b} = N_0\epsilon_2\epsilon_b(1 + C_{s,a,b}P + K_DPD) \tag{5.19}$$

$$N^{\downarrow}_{2,b} = N_0\epsilon_2\epsilon_b(1 - C_{s,a,b}P - K_DPD) \tag{5.20}$$

$$\tag{5.21}$$

We construct a C-insensitive ratio:

$$R_{s,a,b} = \frac{N^{\uparrow}_{1,a} + XN^{\downarrow}_{2,b}}{N^{\downarrow}_{1,a} + XN^{\uparrow}_{2,b}} = \frac{1 - K_DPD}{1 + K_DPD}, \tag{5.22}$$

$$X_{s,a,b} = \frac{N^{\uparrow}_{1,a} + N^{\downarrow}_{1,a}}{N^{\uparrow}_{2,b} + N^{\downarrow}_{2,b}} = \frac{\epsilon_1\epsilon_a}{\epsilon_2\epsilon_b}. \tag{5.23}$$

The same calculation is done for the larger-angle coincidences. From these numbers, D values are extracted separately for sets of small and large-angle coincidences, giving two statistically independent results for each PIN pair.

$$D_{(s \text{ or } l),a,b} = \frac{1}{K_DP}\frac{1 - R}{1 + R} \tag{5.24}$$

The above analysis is applied to each run. The analysis algorithm first searches for operating PINs with operating neighbors. For each neighbor pair, two D coefficients are determined, one for small-angle coincidences and one for large-angle coincidences. The statistical errors are straightforward. Note that the error in the number of decays is always larger than the root of that number ($\sigma_{N_\Delta} > \sqrt{N_\Delta}$) because of background subtraction. Neighbor pairs are identified by requiring that the four relevant coincidence numbers are statistically significant: $N > 2\sigma_N$. Figure 5.12 shows the total number of decay coincidence counts in each PIN for each data run.

If we define N_1 as $N^{\uparrow}_{1,a}$, N_2 as $N^{\downarrow}_{1,a}$,N_3 as $N^{\uparrow}_{2,b}$, and N_4 as $N^{\downarrow}_{2,b}$

$$N_1 = N_{ON}(1, a, \uparrow) - sN_{OFF}(1, a, \uparrow), \tag{5.25}$$

$$\sigma_{N_1} = \sqrt{N_{ON}(1, a, \uparrow) + s^2N_{OFF}(1, a, \uparrow)}, \tag{5.26}$$

$$\text{and} \quad R = \frac{N_1 + \frac{N_1+N_2}{N_3+N_4}N_4}{N_2 + \frac{N_1+N_2}{N_3+N_4}N_3} \tag{5.27}$$

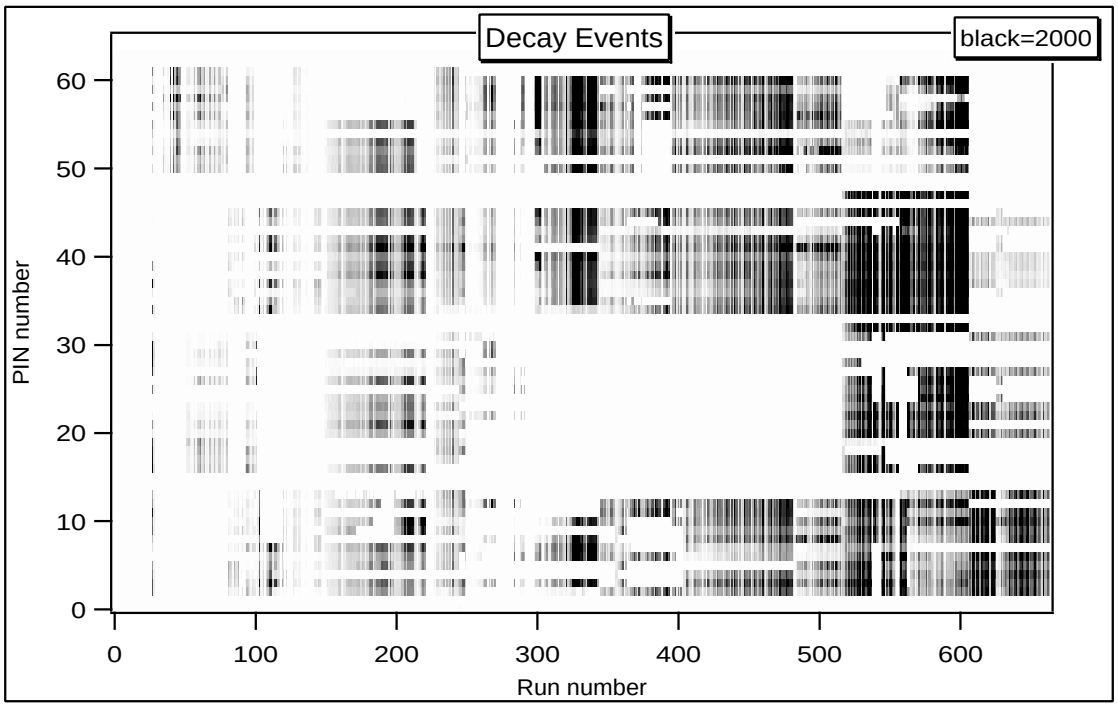

Figure 5.12: Distribution of decay events over runs and PINs. The neighbor pairs used in the analysis are adjacent vertically on this graph, the smaller index in a pair being an even number, i.e. (4,5).

Then the error in R is given by

$$\frac{\sigma_R}{R} = \left[\left(\sigma_{N_1} \frac{2N_4 + N_3}{2N_1N_4 + N_1N_3 + N_2N_4} - \frac{N_3}{2N_2N_3 + N_1N_3 + N_2N_4} \right)^2 + \left(\sigma_{N_2} \frac{N_4}{2N_1N_4 + N_1N_3 + N_2N_4} - \frac{2N_3 + N_4}{2N_2N_3 + N_1N_3 + N_2N_4} \right)^2 + \left(\sigma_{N_3} \frac{N_1}{2N_1N_4 + N_1N_3 + N_2N_4} - \frac{2N_2 + N_1}{2N_2N_3 + N_1N_3 + N_2N_4} \right)^2 + \left(\sigma_{N_4} \frac{2N_1 + N_2}{2N_1N_4 + N_1N_3 + N_2N_4} - \frac{N_2}{2N_2N_3 + N_1N_3 + N_2N_4} \right)^2 \right]^{1/2} \tag{5.28}$$

$$\sigma_D = \frac{2D\sigma_R}{1 - R^2} \tag{5.29}$$

5.4.2 Combining PIN Pair Data

The individual determinations of D must now be combined. We start with a weighted average for small- and large-angle coincidences. For small-angle coincidences in PIN pairs of proton segment A

$$D_{A(s)} = \frac{\sum_{runs} \sum_{pairs} \frac{D(run,pair(s))}{\sigma_D^2(run,pair(s))}}{\sum_{runs} \sum_{pairs} \frac{1}{\sigma_D^2(run,pair(s))}} \tag{5.30}$$

and

$$\sigma_{D_{A(s)}} = \frac{1}{\sum_{runs} \sum_{pairs} \frac{1}{\sigma_D^2(run,pair(s))}}. \tag{5.31}$$

Average values for small- and large-angle D in each segment are shown in figure 5.13. Unless otherwise indicated, the error bars shown are one sigma statistical uncertainties. Systematic effects, which will be discussed in the next section, cause the variation among the detector segments that is evident in figure 5.13. Taking the weighted average of the results in figure 5.13 is not appropriate here. One measure of the consistency of the results is that the reduced χ^2 be unity. For the small-angle averages ($D_{A(s)}, D_{B(s)}, D_{C(s)}$, and $D_{D(s)}$), the reduced χ^2 are 0.88, 1.00, 1.07, ad 1.00, respectively. For $D_{A(l)}, D_{B(l)}, D_{C(l)}$, and $D_{D(l)}$, the reduced χ^2 are 0.90, 0.88, 1.00, and 1.05. In all of the calculations, data from runs before series 20 are ignored. In these early runs, experimental conditions are changing rapidly and the data are inconsistent. In particular, the fast neutron filter crystal changes

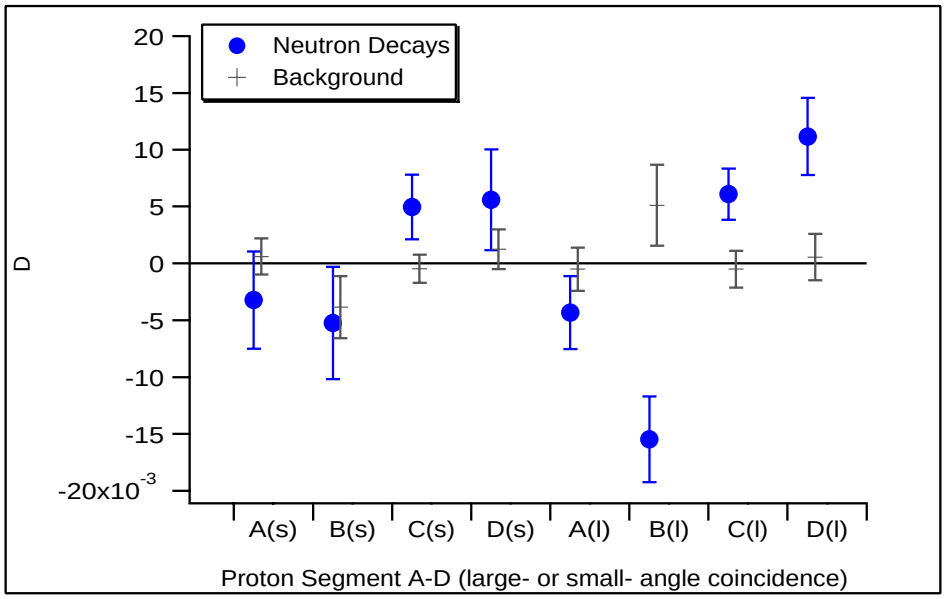

Figure 5.13: Weighted averages of D-coefficients calculated using the PIN pair method in proton segments A, B, C, and D. Averages are found for small- and large-angle coincidences separately. Also shown are the same results when the background, rather than the decay events, are used in the calculation. Error bars are statistical.

several times. Systematic effects due to the changing beam profile are possible and it was decided to ignore these runs.

The consistency of the data is graphically displayed by making a histogram of the fluctuations around the average value. The histogram of $(D_i - D_{avg.})/\sigma_{D_i}$ should be a gaussian with a standard deviation of unity if the fluctuations are purely statistical. Figure 5.14 shows these D/σ histograms for the eight data sets.

Yet another test of consistency over time involves calculating the eight D averages for different subsets of the run and comparing them. One such test is illustrated in figure 5.15. No trends are evident, although low statistics make this test less compelling.

The eight average D should not be combined in a weighted average because they measure systematic effects of different magnitude and sign. (The reduced χ^2 for this weighted average is about 6.) The final result is obtained from an arithmetic average.

$$D = \frac{1}{8}(D_{A(s)} + D_{B(s)} + D_{C(s)} + D_{D(s)} + D_{A(l)} + D_{B(s)} + D_{C(s)} + D_{D(l)}) \qquad (5.32)$$

The statistical errors are combined in quadrature. It will be shown in the following section and in Appendix D that combining the data in an arithmetic average reduces the sensitiv-

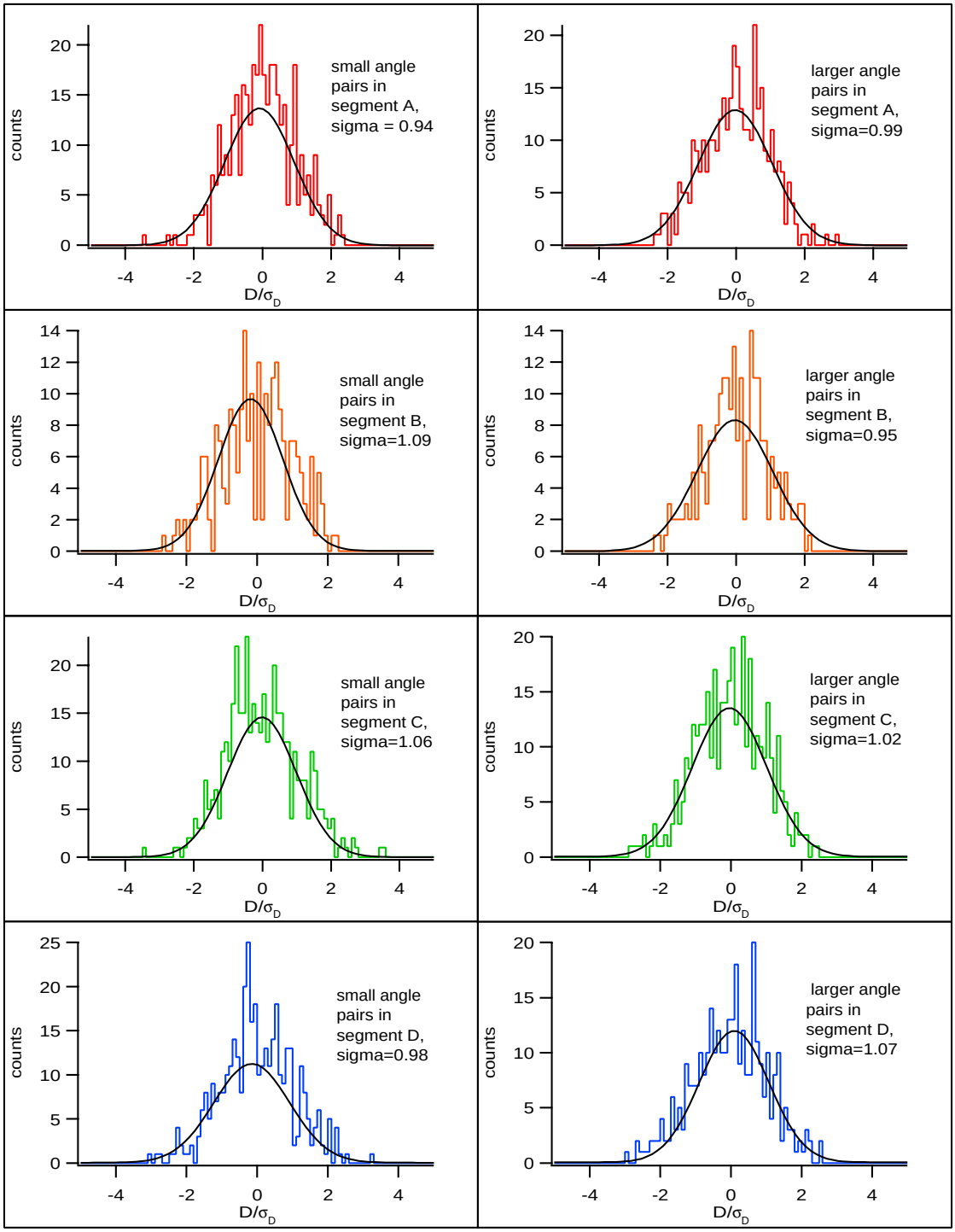

Figure 5.14: Histograms of the deviations of each set of D measurements from the weighted average value for the eight cases. Shown are $(D_i - D_{avg.})/\sigma_{D_i}$ plots with gaussian fits of near unity standard deviation. This indicates that the deviations from the average value are primarily statistical.

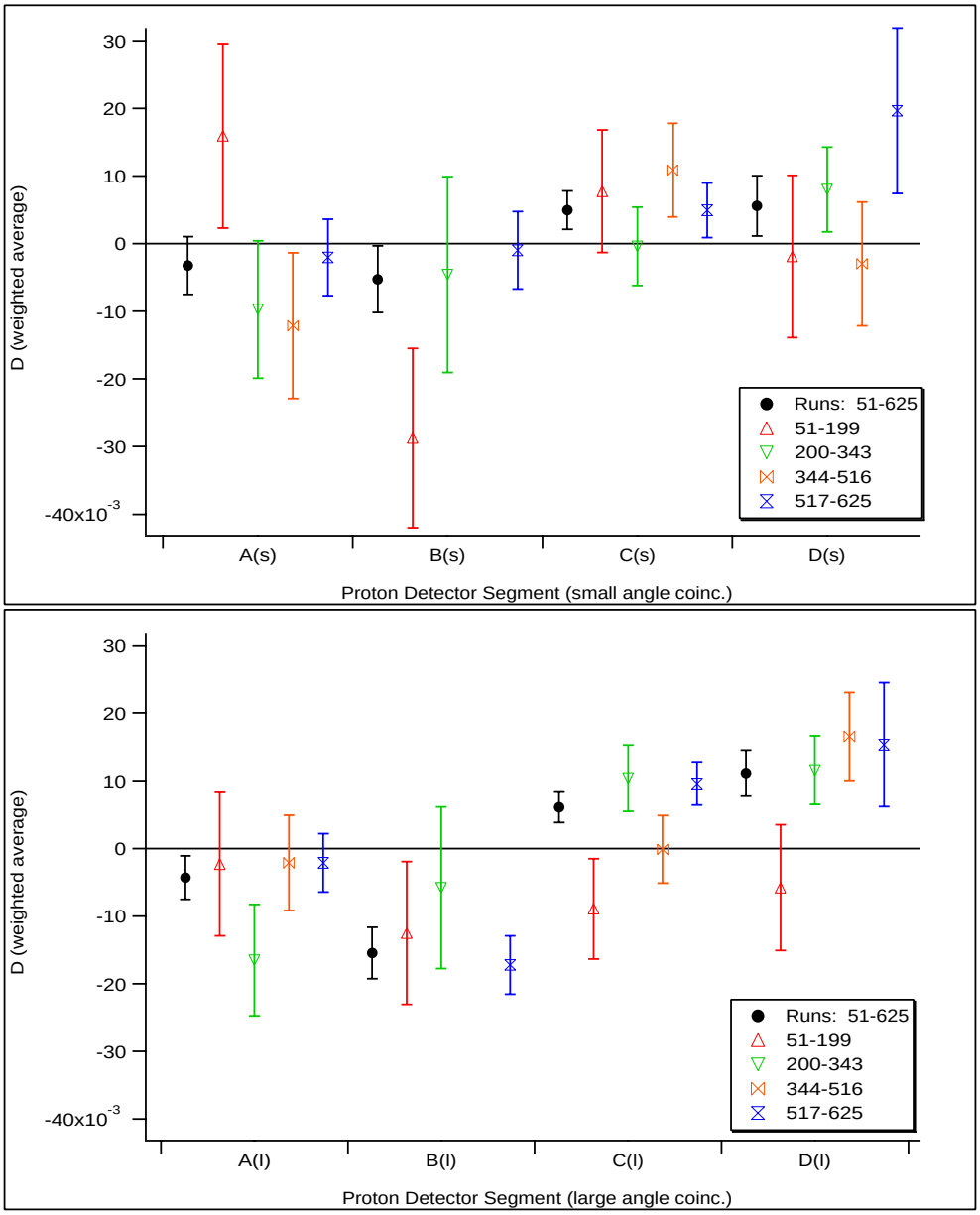

Figure 5.15: A comparison of the eight D values computed with all data in series 20-124 and 126, with those computed in subsets of the data. The four subsets are each approximately 150 consecutive files. This display is useful for studying the consistency of the measurement over time.

Data Series	Data Requirements	Decay Events (10^6) Small-Angle Coincidences	Large-Angle Coincidences	$D(10^{-3})$
20-124,126	$N > 2\sigma_N, f_{min} > 0$	2.89	6.78	-0.053±1.320
20-124,126	$f_{min} > 0$	3.02	6.95	-0.201±1.315
20-124,126	$N > 2\sigma_N, f_{min} > .20$	2.82	6.71	0.126±1.324
20-124,126	$N > 2\sigma_N, f_{min} > 1.0$	2.04	6.15	-0.725±1.427
20-124,126(*)	$N > 2\sigma_N, f_{min} > 0$	2.91	6.81	-0.130±1.323
125(ATP Test)	$N > 2\sigma_N, f_{min} > 0$	0.13	0.31	-69.7±12.3
Background 20-124,126	$N > 2\sigma_N, f_{min} > 0$	1.90	2.12	0.274±0.768

Table 5.2: D results. In the (*) calculation only background events in which the proton arrives before the beta particle are used for background subtraction.

ity of the measurement to a specific systematic effect called the "Asymmetric Transverse Polarization" effect.

$$\sigma_D(stat.) = \frac{1}{8}\sqrt{\sigma^2_{D_{A(s)}} + \sigma^2_{D_{B(s)}} + \sigma^2_{D_{C(s)}} + \sigma^2_{D_{D(s)}} + \sigma^2_{D_{A(l)}} + \sigma^2_{D_{B(l)}} + \sigma^2_{D_{C(l)}} + \sigma^2_{D_{D(l)}}} \tag{5.33}$$

There are additional contributions to the error from the uncertainties in the polarization and the geometrical K_D factors.

$$\sigma_D = \sqrt{\sigma^2_D(stat.) + (D\frac{\sigma_P}{P})^2 + (D\frac{\sigma_K}{K})^2} \tag{5.34}$$

$$\frac{\sigma_P}{P} = 0.02, \quad \frac{\sigma_K}{K} = 0.005 \tag{5.35}$$

Table 5.2 compares the results for various cuts on the data and the result when only the background in N_{OFF} window 2 is used for subtraction. The results of the forced systematic test (the "ATP" test, see section 4.3) are also shown as well as an analysis test in which only background events are used. Figure 5.16 show the decay event rates and signal to background ratios for this data set.

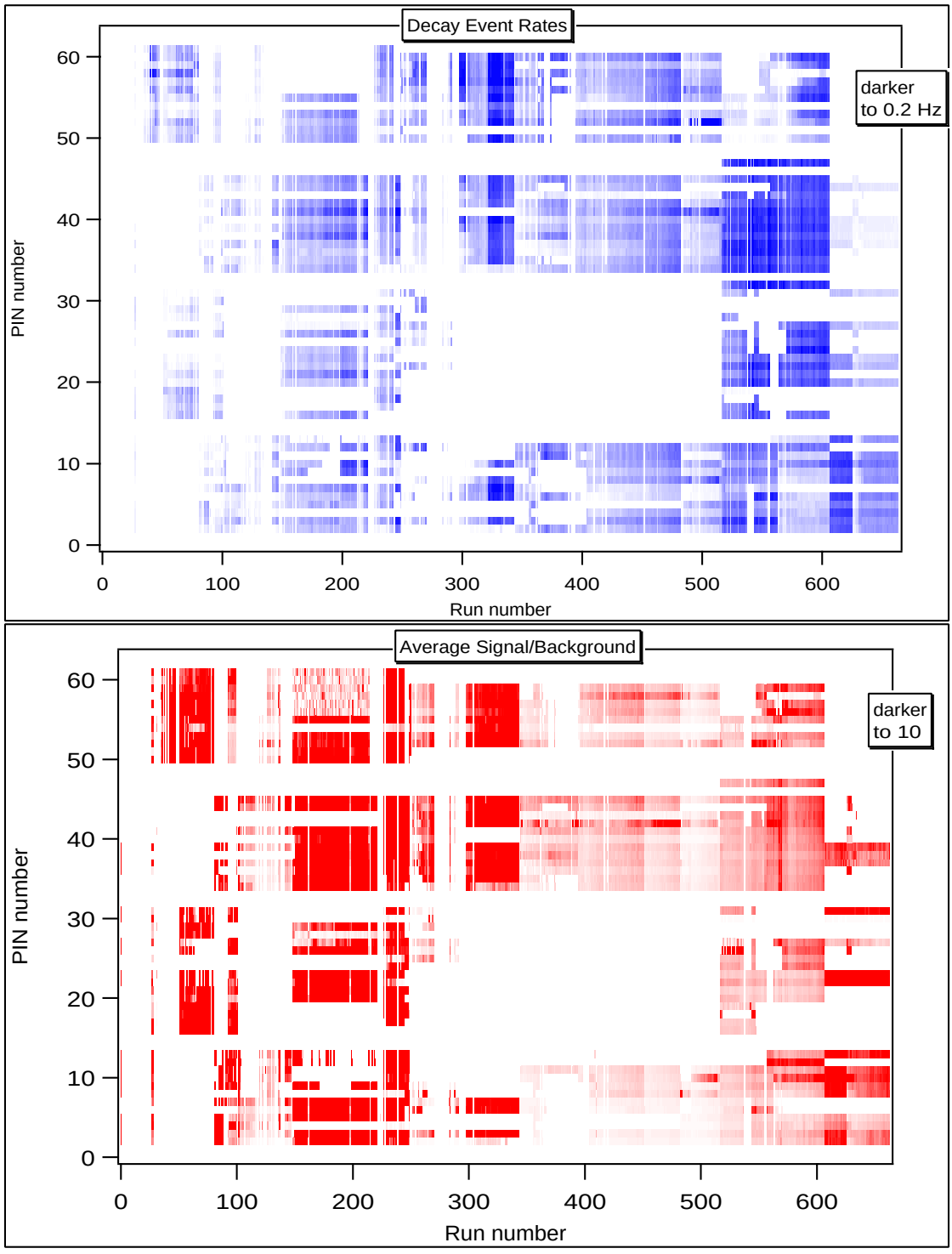

Figure 5.16: Decay event rates and signal/background ratios (f) for this run.

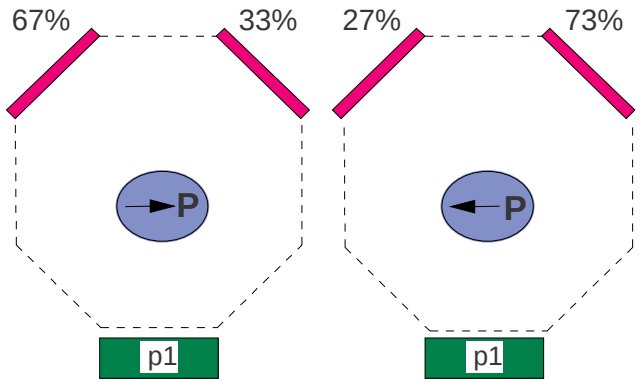

Figure 5.17: Asymmetry created in proton-beta coincidences for a polarization tilted toward a proton segment. The A and B asymmetries create a greater rate of decay into the beta segment in the opposite direction of the spin. The percentages given represent the actual count rates for coincidences with proton segment A in the forced systematic test of series 125(the ATP runs).

5.5 Systematic Errors

There are several systematic effects in the measurement of D. Some of these effects simply cause shifts proportional to D. These are shown to be less than 10% of any real D, and they are well below our sensitivity. Many effects can be shown to proportional to the measured D and can also be limited. More serious false-D effects arise from polarization-dependent systematics effects of the A and B correlations coupled with particular asymmetries in the apparatus or beam. These contributions can be large and will be discussed first.

5.5.1 Asymmetric Transverse Polarization

Polarization Tilt Plus Beam Asymmetry

If the polarization is not perfectly aligned with the detector axis, the A and B correlations can give a false D-like effect. This systematic effect is referred to as the "Asymmetric Transverse Polarization" effect, or ATP. To understand its origins, consider the situation shown in figure 5.17. Here the neutron spin points at a proton segment. The beta detector on the left in figure 5.17 detects more coincidences than the one on the right. The situation reversing with the polarization. This type of spin-dependent asymmetry might lead to a false D-coefficient.

In an ATP test conducted near the end of the run (see section 4.3), the polarization

was tilted 90° to point to proton segment D. The distribution of decay events for coincidence with one proton segment is indicated in figure 5.17. As predicted, there is a large asymmetry in coincidences for the two beta segments opposite one proton segment. For proton segment A, in which the effect should be greatest, the ratio is greater than 2 to 1.

The magnitude of the ATP effect can be shown to proportional three quantities: ξ, the tilt of the polarization with respect to the detector (z) axis; ϕ, the direction of the transverse polarization in the x-y plane; and f_r, a factor which quantifies the effect of a displacement $\mathbf{r}$ of the beam axis from the detector axis. The false D created by these

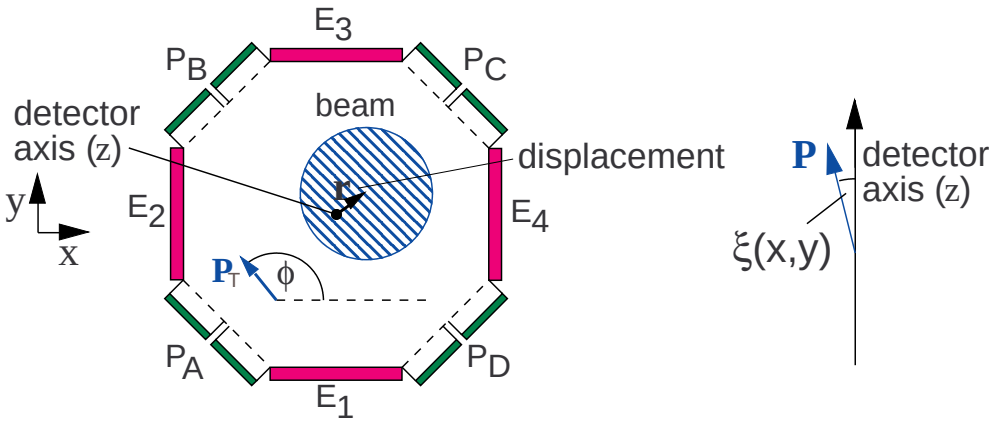

Figure 5.18: The relevant parameters for ATP systematic effect.

misalignments is proportional to

$$D_{ATP} \propto \sin\xi[\sin(\phi + 45°) + \cos(\phi + 45°)]f_r. \tag{5.36}$$

This relation is derived in Appendix D.

The value of D for the ATP test runs is 0.070 ± 0.012. In these runs the value of $\sin\xi$ is about unity. The polarization guide field in the data runs was aligned to within 3 mrad at the onset of the run, and thus $\sin\xi$ should be less than 0.003. The ϕ-dependent term in brackets in equation 5.36 is also unity for the ATP test runs since ϕ was 45°. With no information about ϕ in the data runs, this term can be as large as $\sqrt{2}$. Beam scans in both runs show displacements in x and y of always less than 1 mm. The measured displacement was larger for the ATP runs, which is expected since half of the beam was blocked upstream. From this it is expected that the fractional effect of the beam asymmetry

should be smaller in the real data than it was in the ATP runs. However, this difference is not large, and the relative size is not entirely estimable from the beam profile data since the measurements were made only at the upstream end of the detector region and not along the length decaying into the detectors. A conservative estimate of the beam asymmetry effect in the data is that it could be as large as that in the ATP runs.

Using these assumptions, we can scale the ATP D to estimate the false D in the data runs.

$$|D_{ATP}(data)| \leq (0.003)(\sqrt{2})(0.070 \pm 0.012) = 2.9 \pm 0.5 \times 10^{-4} \tag{5.37}$$

Another approach to estimating this false D is to extract the relevant parameters from the data set itself. This calculation is detailed in Appendix D and gives the result $|D_{ATP}(data)| \leq 6.7 \times 10^{-4}$. The increase over the simple calculation above is due to an apparent value for $\sin\xi$ which is 0.01 rather than 0.003. The increased tilt might be due to a sag in the detector frame after the alignment procedure was completed.

Other ATP Effects

The effect described above is actually a special case of a general category of effects due to asymmetric transverse polarization. In the case of a tilted polarization, the transverse polarization is not asymmetric unless the beam has an asymmetry. For completeness we consider other types of polarization asymmetries and assess their contribution to a false D. The measured false D will be proportional to [40]

$$\hat{z} \cdot \int \mathbf{r} \times \mathbf{P}(\mathbf{r})\rho(\mathbf{r})dV. \tag{5.38}$$

In the case of a tilted polarization, this integral is zero unless the neutron density, ρ, is asymmetric. If there are transverse components arising from a source other than a tilted guide field, these could have their own asymmetry and give a positive effect even with a symmetric beam. If the transverse polarization components are radially oriented (towards or away from the beam axis) there will be no false D since the cross product in the integral vanishes. However, components of $\mathbf{P}$ in the $\pm\hat{\phi}$ cylindrical direction can give a false D. Variations in the guide field across the beam could be caused by permeable materials close to it, distorting the guide field, or position-dependent spin-flipper inefficiencies. These contributions were all minimized, setting 1 mrad as the maximum acceptable local distortion

of the field in the beam volume. This corresponds to a maximum transverse distortion of 5 mgauss for the 5 gauss guide field. With this constraint, the total effect can be at most 10^{-4}.

5.5.2 Polarization and Flux Variations

Variations in the flux (Φ) and polarization (P), even with spin-state dependence, can be shown to give false D proportional to the real value of D. In each case, the value of the efficiency correction factor X (eq. 5.23) is effected. X is related to the actual efficiency ratio by $X = X_0(1+\delta)$ and the contributions from the A and B correlations fail to cancel. In the case of variations in the flux such that $\Phi^{\uparrow} \neq \Phi^{\downarrow}$, we let $\Delta\Phi = \Phi^{\uparrow} - \Phi^{\downarrow}$,

$$\delta = \frac{\Delta\Phi}{\Phi_{avg}} K_D P D \tag{5.39}$$

to first order in $\Delta\Phi/\Phi_{avg}$ This leads to a false D of

$$D_{false}(\Delta\Phi) = \frac{\Delta\Phi}{2\Phi_{avg}}(AK_A + BK_B)PD \tag{5.40}$$

to first order in D. The difference in beam flux for the two states can be estimated by examining the time-dependence of the flux as measured by the fission chamber at the beam stop. The neutron count rates were recorded every 15 seconds in the monitor events. These rates exhibit statistical variations only, distributed around the central value as a gaussian with a standard deviation equal to the square root of the number of neutrons counted in each interval. The fission chamber typically counts about 19,000 neutrons in the 15 second interval, showing fluctuations of order 140, or 0.7%. If there were a difference in flux for the two spin states, it would broaden this distribution since the 15 second counting time is equal to 3 full spin cycles. Thus the flux variation between spin states must be less than 0.4% or it would be noticeable. For D less than 10^{-3}, $D_{false}(\Delta\Phi)$ is less than 2×10^{-7}.

The case of polarization variations is identical. For $\Delta P = P^{\uparrow} - P^{\downarrow}$,

$$\delta = \frac{\Delta P}{P_{avg}} K_D P D \tag{5.41}$$

to first order in $\Delta P/P_{avg}$ This leads to a false D of

$$D_{false}(\Delta P) = \frac{\Delta P}{2}(AK_A + BK_B)D \tag{5.42}$$

to first order in D. The difference in polarization for the two spin states comes from the measured spin-flip efficiency of 95±5% for the current sheet spin flipper. For D less than 10^{-3}, $D_{false}(\Delta P)$ is less than 2×10^{-6}.

5.5.3 Accidental Background Subtraction

As discussed earlier, the accidental coincidence background to be subtracted is estimated by counting events in the "OFF" windows of the proton-beta time spectrum. Scaling this background by the relative widths of the windows before subtracting it from the counts in the "ON" window is correct if the spectrum is flat. Accidental coincidences in theory have an exponential time-dependence, but a flat spectrum (constant detection rate) is an excellent approximation as long as the rate of accidentals is much lower than the reciprocal of the coincidence time window ($\tau_c = 14,7\mu s$). The coincidence rates were 100 Hz to 3 kHz, which is a fraction 0.001 - 0.02 of $1/\tau_c$.

A comparison of the background rates in the two background ("OFF") windows shows that they were not always the same. This was quantified by calculating R_b, the ratio of rates in the window before the prompt peak to the rate in the window after.

$$R_b = \frac{\text{(events in background window 1)/(width of window 1)}}{\text{(events in background window 2)/(width of window 2)}} \tag{5.43}$$

Figure 5.19 shows a histogram of R_b calculated separately for all working PINs in each run with and without the proton energy cut. Figure 5.20 illustrates for several runs how R_b varies among the PINs. In the later runs (with $\tau_c = 7\mu s$), when R_b is greater than 1 it appears to become even larger with the energy cut This is consistent with a very long tail on the proton drift time that extends into window 1. This indicates that for these cases, it is better to use only background from window 2 to avoid oversubtraction of the background. The results of the analysis using only background window 2 are included in table 5.2. However, at times the background in each window also had different slopes, indicating that there are other factors that could affect the validity of the subtraction. The slopes were typically less than 0.03 counts per bin, but were occasionally as large as 0.15 for the background in N_{OFF} window 1.

Another diagnostic of the accuracy of the subtraction is made by examining the coincidences outside the energy range of the neutron decay products. In the absence of decay coincidences, the number of events in different time windows should scale purely with width of the window. This assumption can be tested by measuring the scale factor with events that are not neutron decays, looking only at events with proton energy values well

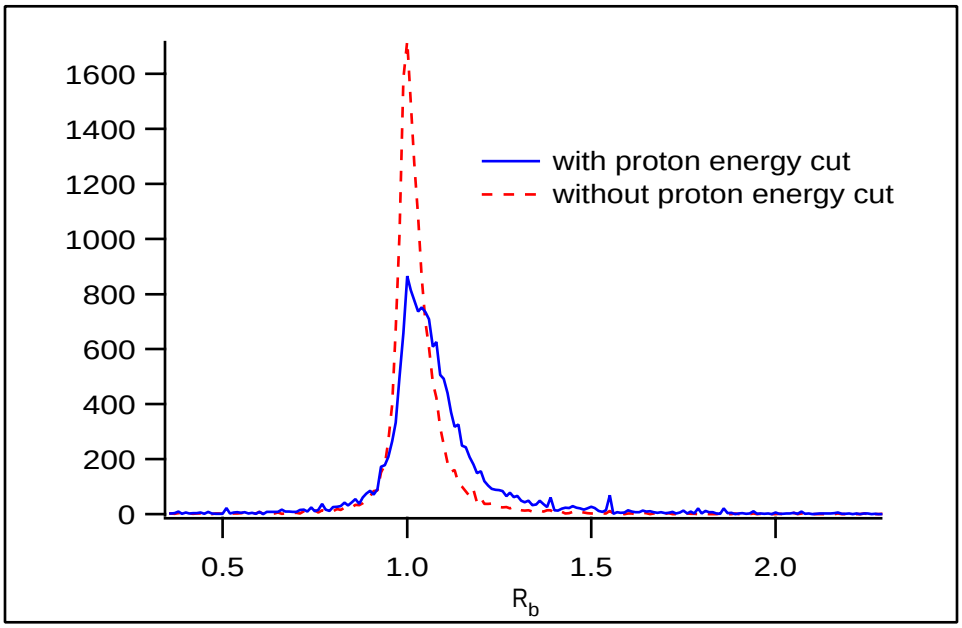

Figure 5.19: The ratio of the rate in the two background windows is not always unity. Making the proton energy cut increases the discrepancy.

below the decay proton energy peak as shown in figure 5.21.

$$s_{\text{measured}} = \frac{\sum_{pADC<E_{prot}} N_{ON}}{\sum_{pADC<E_{prot}} N_{OFF}} \tag{5.44}$$

It is apparent in figure 5.22 that the measured scale factors generally agree with the simple ones, although many of the calculated values have poor statistics even in large files due to the hardware threshold's rejection of events at low energy.

These diagnostics are interesting, but still do not tell us whether there are time-dependent rates in the proton energy window which could create an error in the subtraction. If the scale factors we use in the subtraction are not correct, the measured number of decay events will have an error.

$$N_{\Delta} = (\#\text{ decay events})(1 + \epsilon/f) \tag{5.45}$$

where the scale factor is wrong by the fraction ϵ and f is the signal to background fraction. If ϵ were constant, each PIN pair calculation would yield a false D value of

$$D(\epsilon) = \epsilon\Big(\frac{1}{f_a} - \frac{1}{f_b}\Big)\frac{AK_A + BK_B}{K_D} \tag{5.46}$$

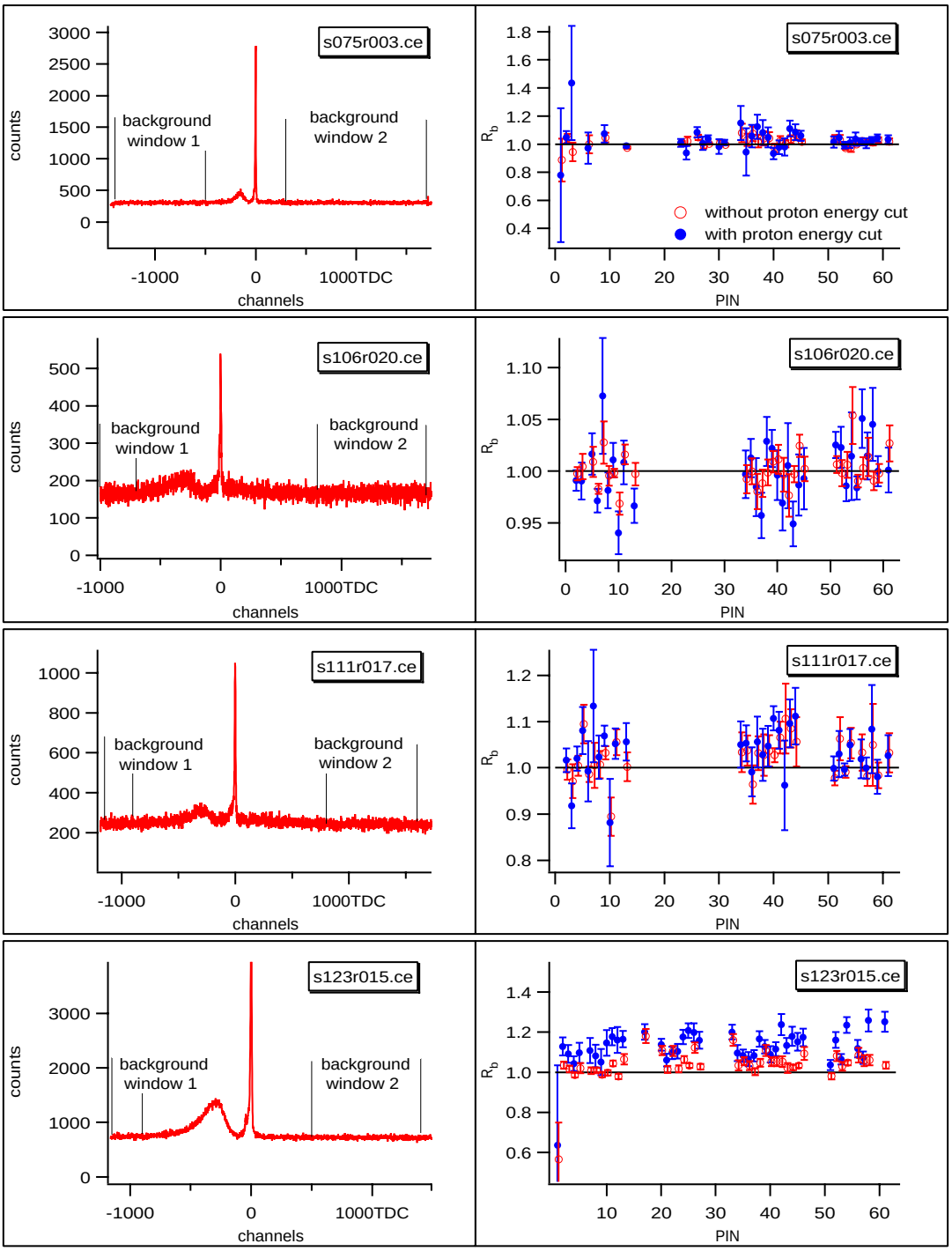

Figure 5.20: The ratio of background rates in two time windows is compared for four typical runs. Ratios are displayed for each operational PIN before and after the proton energy cut.

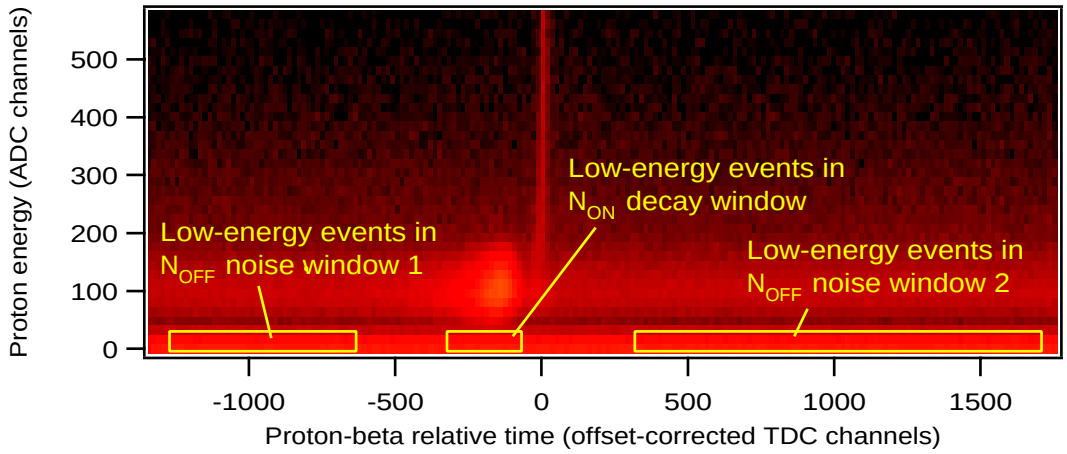

Figure 5.21: The background scale factor can be estimated by comparing the numbers of low-energy events in the timing windows.

where f_a and f_b are the signal/background values for the two PINs in the pair. The signal to background values vary greatly as can be seen in figure 5.16. Since the difference $(1/f_a - 1/f_b)$ fluctuates over time and space and has no preferred sign, the average false D from this effect is zero.

5.5.4 Error Summary

The errors are summarized below.

Sources of Error	Estimates ($\times 10^{-4}$)
Statistics	13
Tilt ATP	7
Twist ATP	<1
Flux Variations	<0.002
Polarization Variations	<0.02

Table 5.3: Contributions to the error.

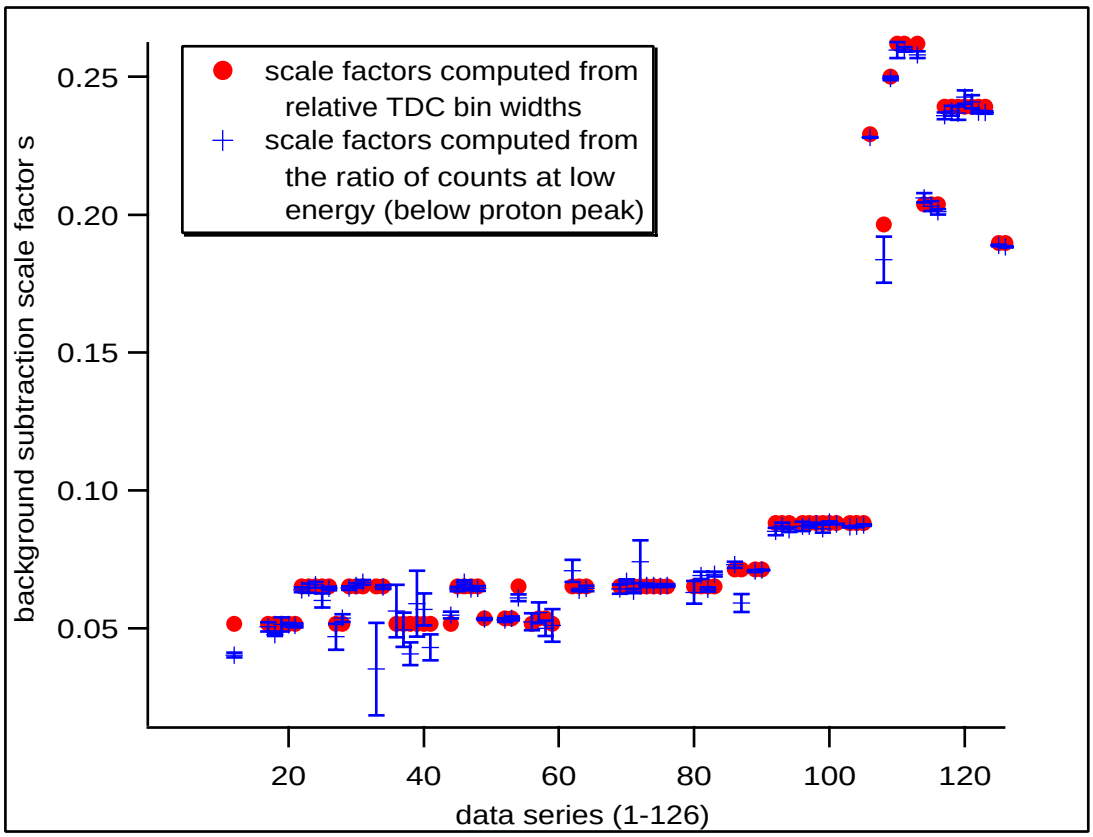

Figure 5.22: The background scale factors can be computed in two ways. Using the relative widths of the TDC windows assumes the accidental background is flat. The second method measured the ratio of counts in an energy window well below the proton peak, and agrees quite well with the flat background assumption. The average scale factors change dramatically toward the end of the run when the coincidence window was shortened to reduce the deadtime.

Chapter 6

Conclusion

6.1 Interpretation of First Run Results

The results from the first run of emiT had relatively large statistical and systematic uncertainties due to the poor performance of the detector system. The statistical uncertainties are slightly smaller than the world average, with systematic uncertainties only a factor of two smaller. The results are consistent with time reversal invariance and thus with the Standard Model. No new physics is indicated by these results.

Kurchatov	$2.2 \pm 3.0 \times 10^{-3}$
ILL	$-1.1 \pm 1.7 \times 10^{-3}$
This work	$-0.1 \pm 1.3(\text{stat.}) \pm 0.7(\text{syst.}) \ \times 10^{-3}$

6.2 The Second Run of emiT

The possibility for collecting a very good data set is excellent given the comprehensive modifications outlined below. The same total running time would provide an opportunity to place a constraint on the D-coefficient as low as 5×10^{-4}.

The upgrades for the next run are designed to increase the stability of the experiment, the uniformity of the detector response, and the livetime of the data acquisition. The PIN diodes in the proton detectors will be replaced with surface barrier detectors or PIP diode detectors, both of which have dead-layers below 20 μg/cm^2. Protons detected in these detectors will require only 30 kV or less of acceleration voltage for noise-signal separation. Improvements to the preamplifiers include non-magnetic FETs, on-board thermocouples to monitor local temperatures, and in situ Tantalum sources to monitor gain. The cables

inside the proton detector will be replaced with less fragile ones. The preamplifiers have been reworked for lower power consumption, thus lightening the heat load on the cooling system, and the circuit will optimized for the detectors replacing the PINs The shaper/ADC boards have been overhauled to include a hard threshold, improved shaping/attenuation, less cross-talk and gain fluctuation, and a redesigned ground plane to reduce noise.

Four fast fiber optic links have been built to fit directly onto each proton detector at the electronic feedthrough into the vacuum. Analog preamp signals and thermocouple voltages are converted to optical and received by the shaper boards at low voltage. Pulser signals are also input this way. The only HV connection via wire is the preamp power and detector bias. These modifications reduce the HV leakage current and the capacitance of the entire system, reducing the frequency of and damage from sparks. The shaper/ADC boards will no longer be susceptible to spark damage and will be much easier to access. A test chamber has been implemented with a viewing window for locating visible sparks and emission points during conditioning of the electrodes. A new cooling system will also be installed.

The data acquisition is being streamlined in software and hardware, and all problematic components replaced. The Kinetic Systems module in the data acquisition has been replaced with a BiRa 1711 VME board CAMAC Branch Highway Driver, which is significantly faster and should contribute significantly less to the deadtime. Rewiring the trigger to accept only the 135° coincidences will reduce the deadtime approximately by half. A Macintosh upgrade to a 266 MHz G3 PowerPC will improve the speed of the Macintosh software and allow the NuBus to be replaced with a faster PCI bus.

Improving the shielding wall between emiT and the experiment on the neighboring beamline may allow removal the fast neutron filters. This will increase the flux by 30% and prevent distortion of the beam by the filter crystal.

Appendix A

Fabrication of Beta Detectors

(Step 1) The 16 light-guide segments (each guide had two parts) had been cut to shape via numerically controlled ball-end milling and required extensive polishing before installation. This was accomplished in several steps, with care not to round out edges needing to make contact with other surfaces at glue joints, and care to maintain the cross-sectional area so as not to threaten the adiabaticity of the light path. Especially important was a lip on the inner piece of guide, which presses against the outer surface of the vacuum chamber, keeping the guided from being sucked in and defining the angle at which it meets the scintillator. If the guide were to tilt, it would stress the scintillator and glue joints. The steps for polishing were as follows.

(a) The surface roughness was removed by wet-sanding with 320 grit sandpaper. The polishing then continued with successively finer particles. (b-d) Sanding with 400, 600, 1000 grit papers. (e) Polishing with red jeweler's rouge on a flannel buffing wheel (avoiding heat, which crazes the lucite.) (f) Hand-polishing with aluminum oxide and distilled water.

After polishing, the outer guide sections were wrapped with aluminized mylar (aluminum side in) and black PVC low-temperature heat shrink tubing. The end faces of the guides were sanded to 600 grit roughness for strong glue joints.

(Step 2) The scintillator was delivered with the specified thickness and width and smooth surfaces. The ends were cut to length at Berkeley, using a special clamp, and slow milling with ample coolant. These precautions were taken to avoid stressing the scintillator during cutting, as it is well known that stress and heat both lead to crazing of the plastic. Crazing is the process by which the plastic develops many small cracks in the surface which extend into the volume, rendering it virtually non-transmissive. The scintillator was handled

with gloves and kept clean of dirt and contaminants to avoid scratching the delicate surface and introducing oils such as those from skin, which have also been shown to cause crazing. Any edges that became dirty were cleaned gently with Alconox detergent and distilled water, then rinsed with 190-proof ethanol. Before gluing, the scintillator was wrapped with Saran wrap and the ends with teflon sticky tape to protect it from handling and glue spills.

(Steps 3 and 4) After cleaning all the parts, the o-rings were coated lightly with Apiezon N vacuum grease before placement around the guide and between the compression plates. The guide was clamped into the position it would take under vacuum and the seals were checked using a helium leak-checker (an oil-free vacuum system).

(Step 5) A special clamp was made for the scintillator to hold it gently and allow us to accurately position it before gluing. The width of the clamp, which determined the scintillator distance from the vacuum backplate (and thus the beam), was within a few mils tolerance.

The assembly so far was then mounted on a stand that allowed us to always have the surface to be glued parallel to the floor. The was measured and mixed, then pumped in a vacuum chamber for one minute to liberate bubbles. We waited 12 hours between each plastic glue joint before rotating the apparatus, although the pieces remained clamped together for the full 24 hour required curing time. Each phototube to guide glue joint, whose compression was supplied by the weight of the tube, cured undisturbed for 24 hours.

(Step 6) Since one vacuum seal on each side had to be loosened to move parts in Step 5., those seals were rechecked after being retightened.

Steps 7, 8, and 9. After gluing the guides and phototubes all paths for light to enter the guide or vacuum chamber were sealed with black felt, more heat shrink, and black photographic masking tape. The region between the phototubes and bases was also taped to prevent light from entering the back of the tube, and to support the base.

Appendix B

Data Acquisition Details

B.1 Acquisition Code

At the start of a run, input parameters are read, the data file is opened,the run parameters are written to a header, and the acquisition code is downloaded to the VME CPU. There were three data taking modes: acquisition of proton singles, beta singles, or coincidence events. The process worked as follows.

(1) Initialization: Clear and initialize all VME and CAMAC modules. The CAMAC NIM OUT sends NIM-level pulses to clear flip/flops, and held a bit pattern that determined the type of trigger (Beta, Coincidence, Proton) accepted by the logic. The high voltage VME at this point receives the proton configuration file, which set the shaper/ADC boards mode, and individual thresholds and gains, including disabling inactive channels

(2) Event collection: Coincidence Mode: The KS is constantly polling the CAMAC crate for a Look-At-Me (LAM), set to be received in the NIM IN module, from the NIM trigger logic. Once this is received, the HV VME is read and cleared and the appropriate CAMAC modules are read and cleared. Some information is also read from the LV VME, but only some is reset. The data is written to a circular buffer in the VME CPU, which is periodically unloaded by the PowerPC. At the end of this cycle, the NIM OUT is written to, sending logic pulses that end the signals which have been inhibiting proton and beta particle triggers during the event collection. The Beta Singles Mode is identical except that the HV VME is ignored. In Proton Singles Mode, there is no polling of the CAMAC. Instead, the HV VME is polled to look for conversions of the shaper/ADC boards, which are read and cleared independently, and never inhibited externally.

(3) Monitor Event Collection: Periodically (at intervals initially of a set number of events and later at intervals of a set number of clock pulses), CAMAC polling is temporarily halted to collect data from the assortment of monitors connected to the system. These include readings of the VME ADC, which contains information on magnet currents, HV parameters, pressure, etc, and of the VME scaler, which has information on beam flux, livetime, and individual phototube trigger rates. This information is written to the circular buffer, tagged as a monitor event.

If a certain time passes in which no events are written to the buffer, step (1) is repeated. This cycle continues until a halt command it received from the Mac, corresponding either to the end of a timed run or a user stop, at which time the Mac code runs until the buffer is empty and it writes end-of-file.

B.2 Coincidence Logic

There are four channels of identical logic for each beta detector. Each incoming phototube pulse is duplicated and one channel of each enters a linear sum module. The summed pulse goes to a discriminator which is the trigger for that detector segment. If the summed pulse crosses the threshold, it opens a gate, which subsequently ignores any inputs for the duration of the gate, set at 7 μs, the length of a coincidence window. During this time the three analog pulses (side A, side B, and the sum) have been sent to a CAMAC charge-integrating ADC with an appropriate gate, and the pulses from separate discriminators on the A and B pulses have been sent to a TDC started by the segments trigger. The pulses were delayed 200 ns with passive delay to fit completely into the ADC gate, which was about 100 ns, opening about 10 ns before the pulse begins, and encompassing the full tail of all but the largest pulses, which are out of range anyway. The TDC inputs are always followed by a common stop pulse which assures that each channel will convert even if a given phototube does not fire. We found this was necessary to prevent a failure of the fast clear which we observed at a 0.1% rate without the common stop. Two microseconds after the end of the 7 μs coincidence window, the ADC and TDC are cleared unless a proton trigger pulse arrives during that time, and prevents the clearing pulse from being made. If that happens, the coincidence condition has been satisfied, and the entire discriminator module evaluating the sum pulses is inhibited until the computer has finished reading the event.

Each beta segment is independent, and each continues in its wait-then-clear cycle until a coincidence is made. In Beta Singles Mode, the modules never self-clear. They simply each convert when a pulse is received, then wait, inhibited, until the computer reads the data and releases the inhibit.

The proton segments do not have independently operating hardware in Coincidence Mode. When a PIN diode pulse crosses a VME threshold, the other channels on the board are inhibited internally within 40 ns. A TTL signal goes out the front end and starts a gate that is sent to the external inhibits of all the shaper/ADC boards. This logic cycle takes over a hundred nanoseconds, creating a small window for the possibility of two proton events in the same coincidence event. If the proton trigger arrives when no "beta gate" (the 7 μs pulse) is open, coincidence is not satisfied, and a signal is sent back to the HV crate to release the inhibit and fast clear all the boards.

The master trigger indicates that an event should be read and stored. This comes into the NIM IN module, which alerts the VME CPU. The proton triggers from the fast fiber optic board are OR'ed to make the PTrig, which starts the proton inhibit. In Coincidence Mode, the Ptrig is delayed 3 μs and makes 3 new signals to start of the TDC, prevent the fast clear of the beta signals, and open the coincidence AND gate.

The segments of beta electronics produce 7 μs pulses that are the inputs 0-3 of the NIM IN, and also go to the coincidence AND gate. These signals are also individually delayed to produce stops 1-4 of the slow TDC, providing a relative time of coincidence for each of the beta detectors relative to the starting proton signal. If there is a coincidence a pulse (the Master Trigger) is sent to the strobe of the NIM IN, which then registers which of the four beta detectors fired by converting inputs 0-3. The Master Trigger also starts Event Busy, which inhibits all beta detectors while the CPU reads the event. At the end of the read-clear sequence, the NIM OUT is commanded to send a pulse, EventDone, that ends EventBusy, releases the proton inhibit, and clears the Slow TDC and proton boards. If there is a proton signal but no coincidence, the proton inhibit is released, the proton boards and slow TDC cleared, and the system is ready for the next event.

The inverse of the proton inhibit enters an AND gate with a clock and the result is sent to the VME scaler. When compared with the clock alone, this gives a measure of the system livetime that accounts for both Proton Singles and computer read deadtime, but does not account for individual beta singles deadtimes.

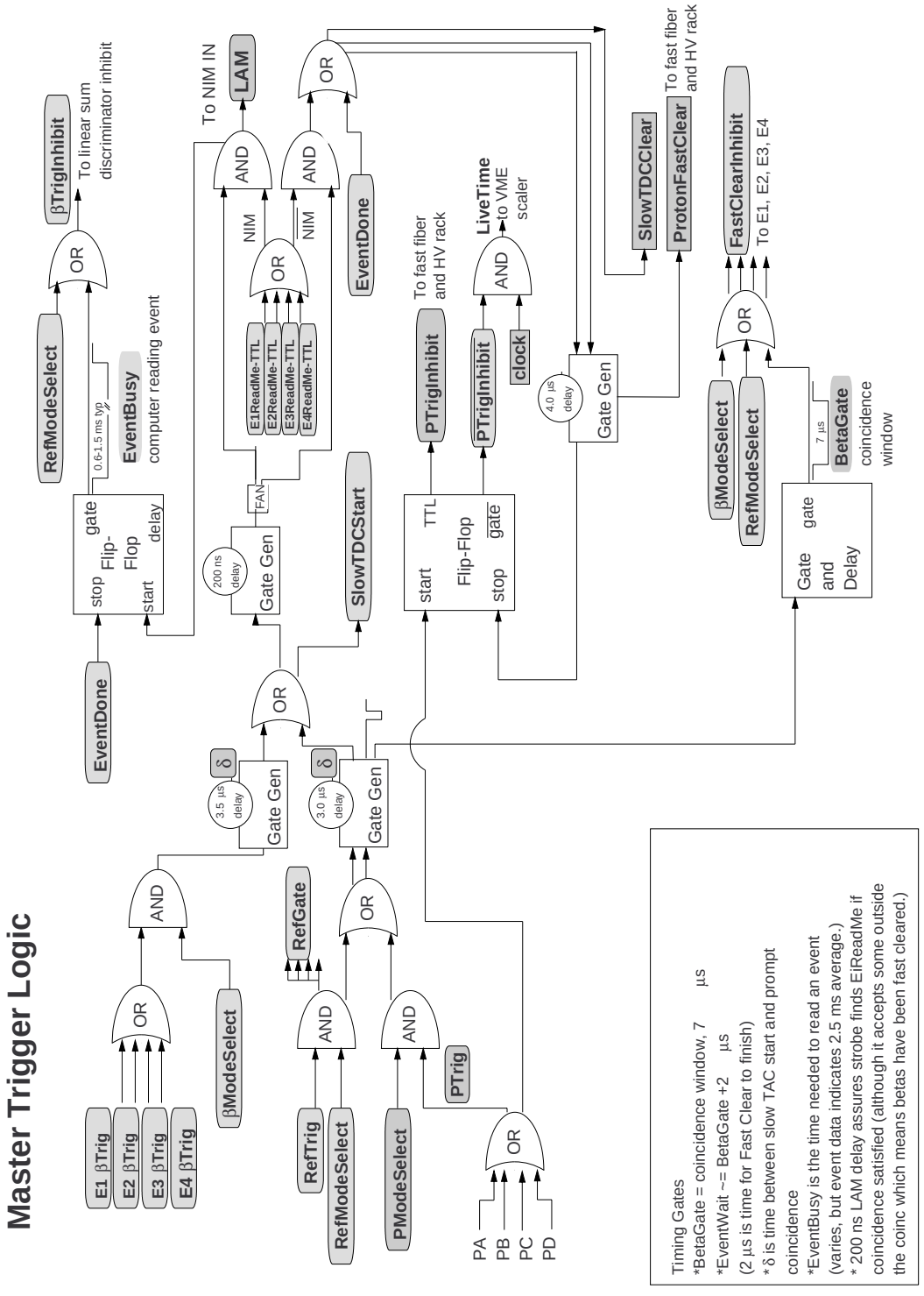

Figure B.1: Detailed DAQ schematics

β: E1

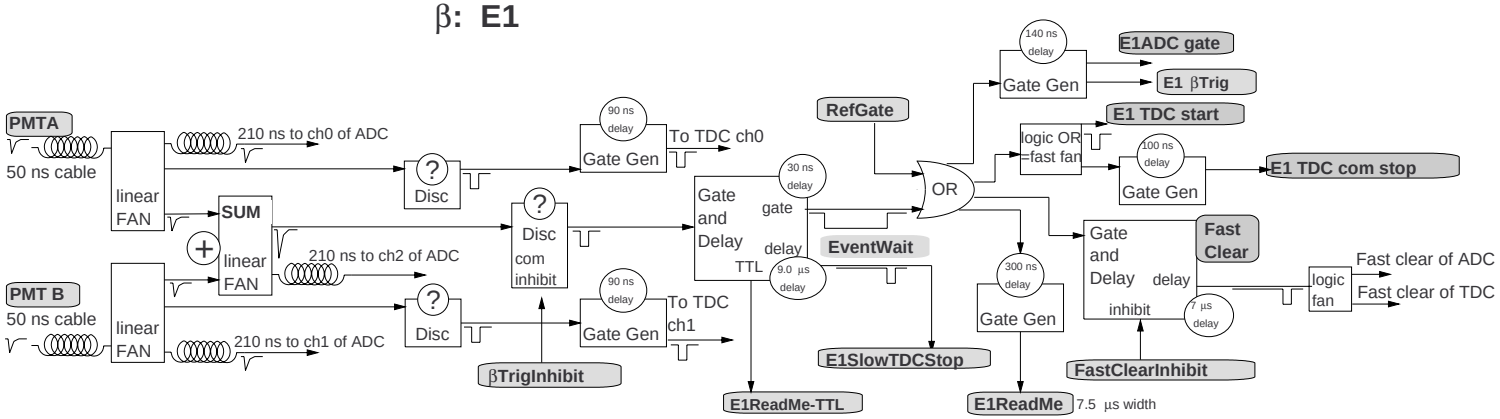

CAMAC for βE1:

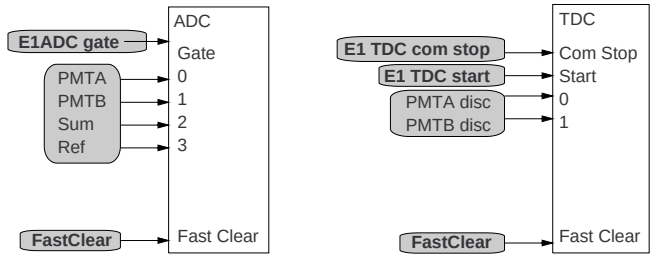

P: PA

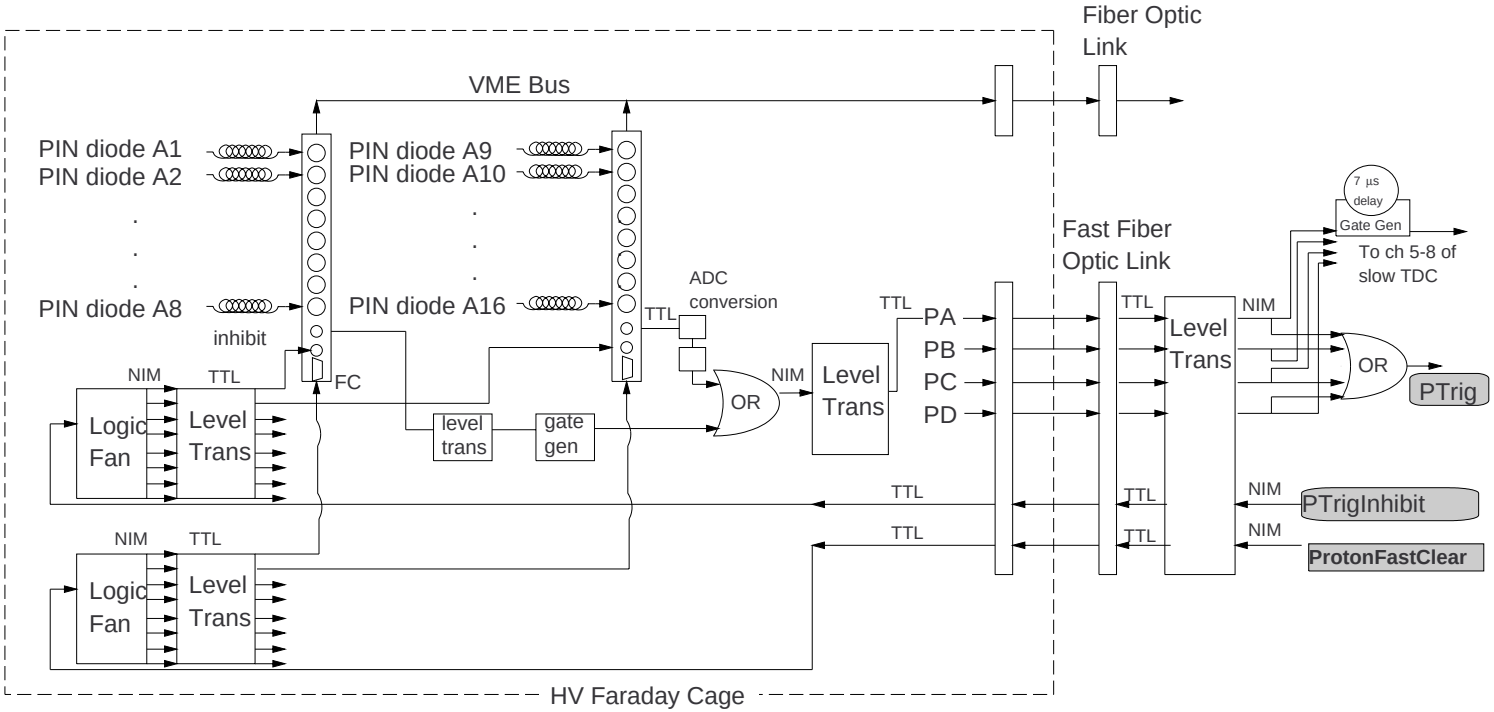
Fiber Optic
Link
VME Bus
PIN diode A1
PIN diode A2
PIN diode A8
PIN diode A9
PIN diode A10
PIN diode A16
inhibit
FC
ADC
conversion
TTL
NIM
Logic
Fan
Level
Trans
level
trans
gate
gen
OR
PA
PB
PC
PD
Fast Fiber
Optic Link
7 µs
delay
Gate Gen
To ch 5-8 of
slow TDC
PTrig
PTrigInhibit
ProtonFastClear
HV Faraday Cage

VME:

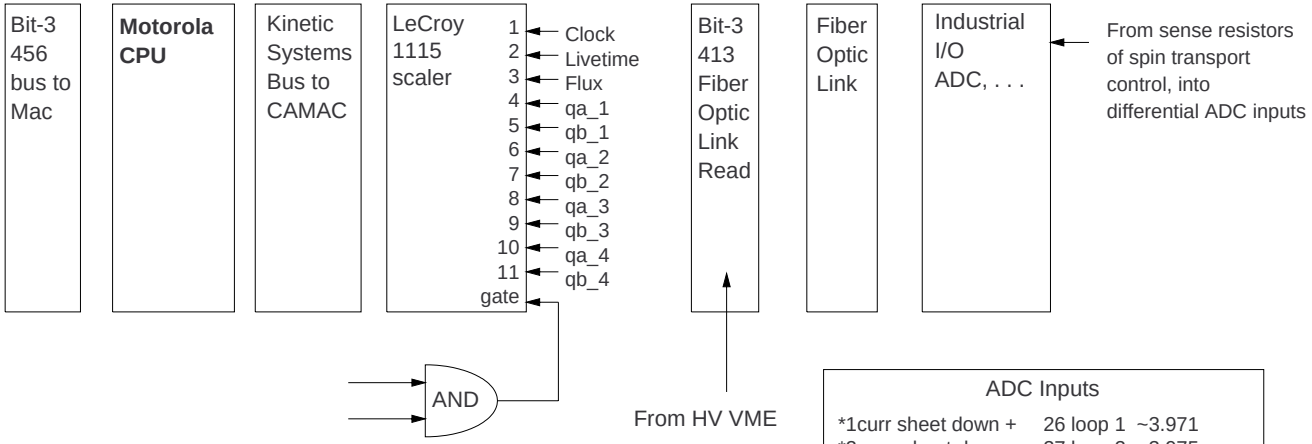

Scaler, I/O board, and internal scalers on shaper/ADCs read during monitor events (at timed intervals)
Clock = 10 kHz clock from CAMAC
Livetime = Clock*$\overline{\text{PTrigInhibit}}$
Flux = Fission chamber SCA output
qa_1, . . . = individual discrimator outputs
(uninhibited) for each phototube

ADC Inputs

*1curr sheet down +	26 loop 1 ~3.971
*2 curr sheet down -	27 loop 2 ~3.975
*3 curr sheet up +	28 loop 3 ~1.745
*4 curr sheet up -	29 loop 4 ~3.482
*5,6 flux-gate x	31 grad 2
*7,8 y	32 grad 1 ~1.15
*9,10 z	33 grad 4
11 sin 1 ~1.778V	34 grad 3
12 sin 2 ~.96	
13 sin 3 ~ .333	36 pressure
14 sin 4 ~ 1.142	*37 High voltage V
15 sin 5 ~ 1.846	*38 High voltage ground
16 sin 6 ~ 2.132	*39 High voltage current
17 shield I ~ 4.422	*40 High voltage ground
18 shield O ~ 3.476	
19 GF 1 ~1.804	
20 GF 2-7 ~1.606	
21 GF 8 ~ 2.536	
22 sol 1 ~2.429	
23 sol 2 ~3.808	* differential,
25 sol 4 ~ 1.541	otherwise single ended

Camac:

For Master Trigger:

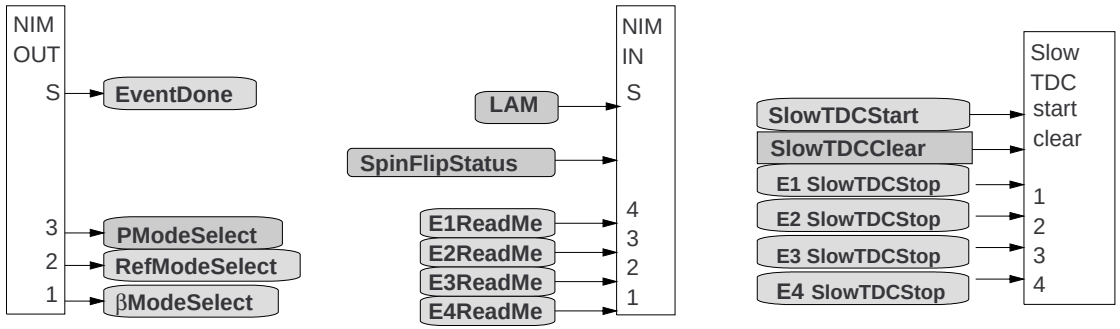

Spin Flipper Timing Control:

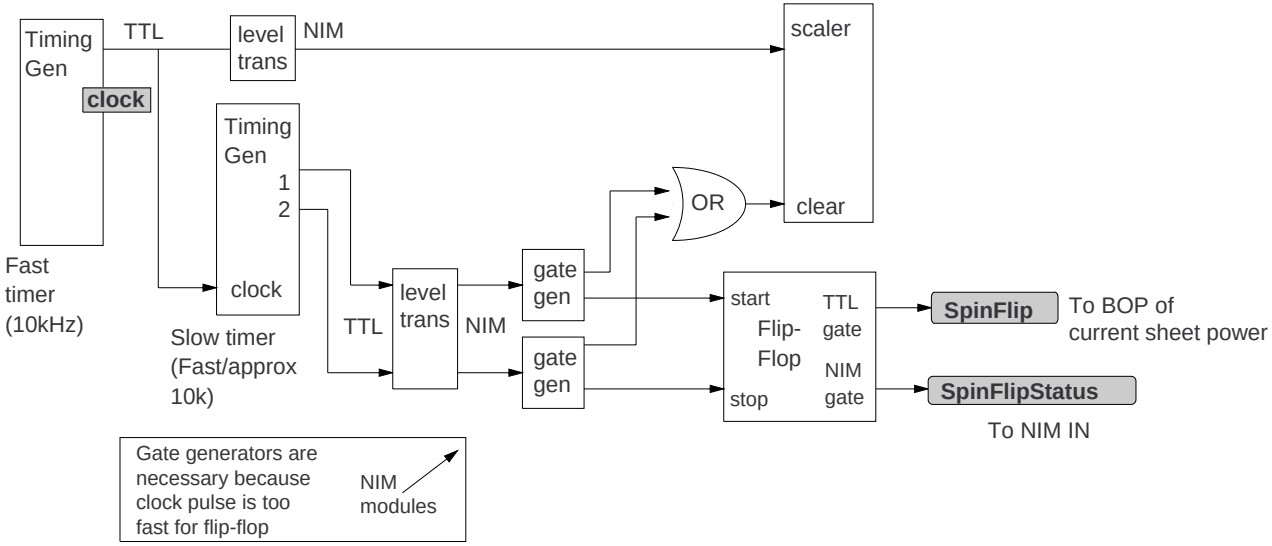

Timing

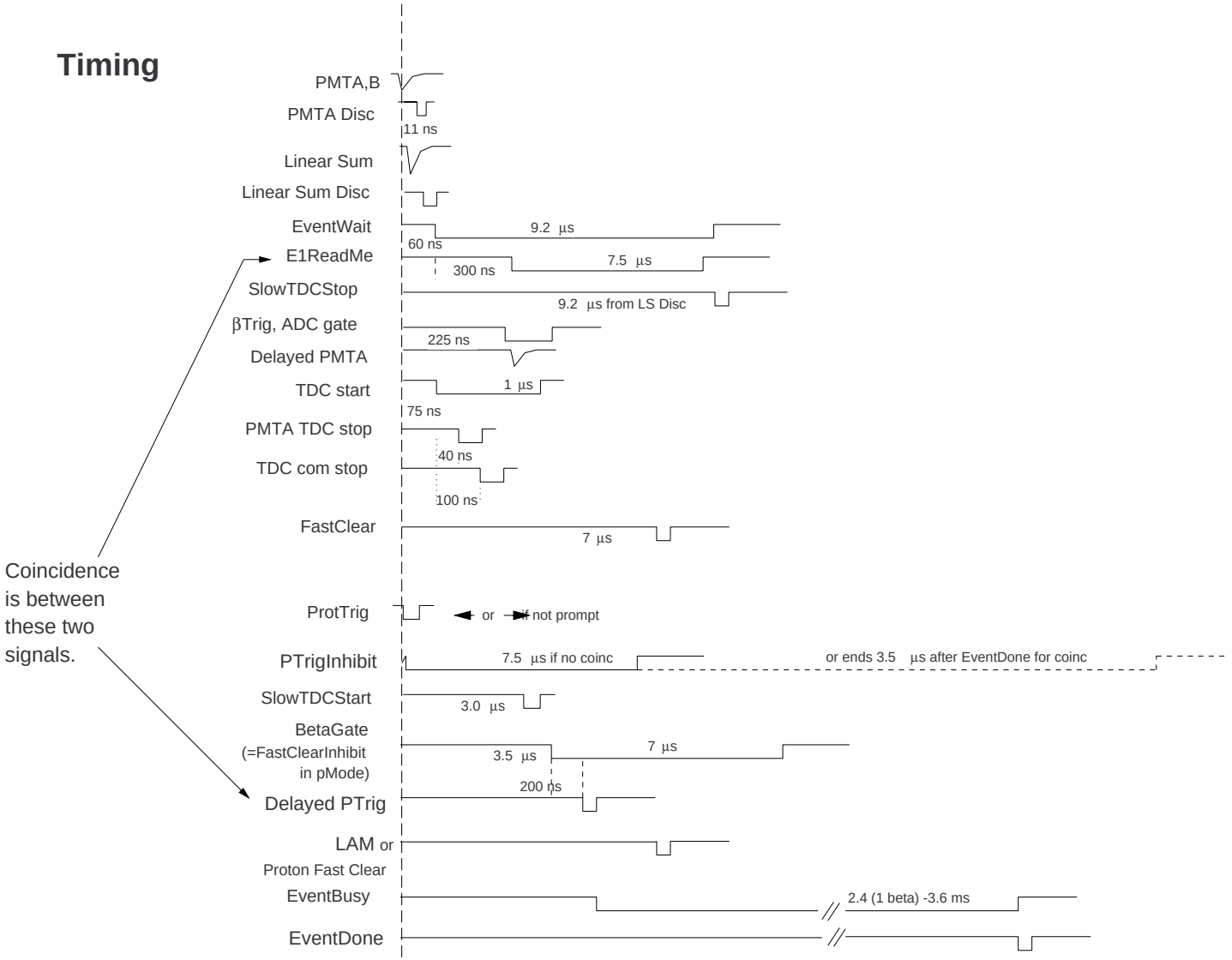
PMTA,B
PMTA Disc
11 ns
Linear Sum
Linear Sum Disc
EventWait
9.2 µs
60 ns
E1ReadMe
300 ns
7.5 µs
SlowTDCStop
9.2 µs from LS Disc
βTrig, ADC gate
225 ns
Delayed PMTA
TDC start
1 µs
75 ns
PMTA TDC stop
40 ns
TDC com stop
100 ns
FastClear
7 µs
Coincidence is between these two signals.
ProtTrig
or
if not prompt
PTrigInhibit
7.5 µs if no coinc
or ends 3.5 µs after EventDone for coinc
SlowTDCStart
3.0 µs
BetaGate
(=FastClearInhibit in pMode)
3.5 µs
7 µs
200 ns
Delayed PTrig
LAM or
Proton Fast Clear
EventBusy
2.4 (1 beta) -3.6 ms
EventDone

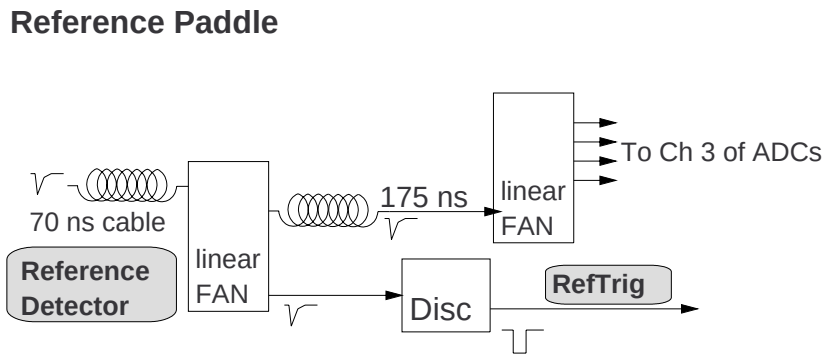

Figure B.2: The author and the DAQ hardware.

Type	Model(s)
	NIM
Linear (Analog) FANs	LRS 428F
Level Adaptors	LRS 688AL, PS 726
Level-Crossing Discriminators	LRS 623B
Gate and Delay	PS 794,LRS 222
Gate Generators	EGG GG8000
Logic FANs	LRS 429,429A, PS 744
AND/OR Logic	LRS 622, PS 755
	CAMAC
Charge-Integrating ADCs	LRS 2249W
TDCs	LRS 2228A (100 ns full scale), PS 7186 (mod. w/ 15 μs full scale)
Timing Generators	KS 3655
NIM In Register	BiRa 2351
NIM Out	BiRa 3251
Scaler	LRS 2551
Controller	KS 3922
	VME
CPU	Motorolla MVME 1475A-2
NuBus to VME	Bit-3 456
Fiber Optic Controllers	Bit-3 413
Scaler	LRS 1151N
I/O and ADC array	Acromag IP320, IP220
Bus Interface	KS 2917K

Table B.1: Modules used in the DAQ. LRS = Lecroy Research Systems, PS = Phillips Scientific, EGG = EG&G Ortec, LNBL = Lawrence Berkeley National Laboratory, KS = Kinetic Systems.

Appendix C

List of Files Rejected

File Name(s)	Number of Files	Reason for Rejection
s023r002	1	documentation missing
s029r006	1	beam off
s045r010	1	beam off
s072r001-s073r010	11	magnets off
s074r001-3	3	flip TDC error
s077r001-s080r006	13	flip bit error
s084r001-s085r001	6	proton trigger error
s087r001	1	TDC errors
s089r011	1	test of nearby magnet
s096r001	1	proton trigger error
s105r002	1	configuration file error
s108r001	1	trigger hardware error
s109r012	1	spin flipper failure
s110r002-3	2	spin flipper off
s113r004-5	2	TDC errors
s113r022	1	proton trigger error
Total	48	

Table C.1: Rejected data files.

Appendix D

Quantitative Analysis of ATP Systematic Error

D.1 Transverse Polarization

Consider a narrow beam (a "pencil" beam) of neutrons traveling along the detector axis with a polarization tilted transverse to the detector axis ($\xi = 90°$) as shown in figure D.1. Let the neutron spins point (when "up", or parallel to the guide field) in a direction making an angle ϕ from the center of a proton segment as shown. For simplicity, the beta detectors will be treated as small detectors at the same z-position as the PINs.

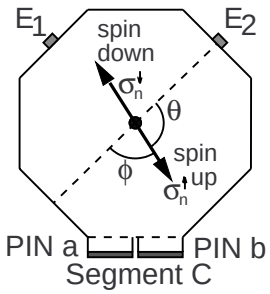

Figure D.1: When the guide field is tilted to be transverse to the beam axis, the direction of the polarization can be defined by an angle ϕ with respect to the line bisecting beta detector E4. (This is the $+x$-axis for emiT.)

The A and B correlations give a net negative $\hat{\sigma}_n \cdot \mathbf{p}_e$ correlation so that, if $D = 0$

$$N_{E_i,PIN_j} \propto 1 - \gamma P \cos\theta_{\sigma_n E_i}. \tag{D.1}$$

θ is the angle between the neutron spin and the momentum of an electron detected in E_i and depends on the spin state and on ϕ. γ depends on A and B and the solid angles involved in the beta-proton coincidence. $\theta_{\sigma_n E_1} = 270° - \phi$ and $90° - \phi$ for up and down spin, respectively, and $\theta_{\sigma_n E_2} = 180° - \phi$ and ϕ. The ratio of equation 5.22 would be

$$\begin{aligned}\frac{N^{\uparrow}_{E1,PINa} + XN^{\downarrow}_{E2,PINb}}{N^{\downarrow}_{E1,PINa} + XN^{\uparrow}_{E2,PINb}} &= \frac{1 - \gamma P\cos(270° - \phi) + 1 + \gamma P\cos(\phi)}{1 - \gamma P\cos(90° - \phi) + 1 + \gamma P\cos(180° - \phi)} \\ &= \frac{1 + (\gamma P/\sqrt{2})\sin(\phi - 45°)}{1 - (\gamma P/\sqrt{2})\sin(\phi - 45°)}\end{aligned} \tag{D.2}$$

This gives

$$D_C = -\frac{\gamma \sin(\phi - 45°)}{\sqrt{2}K_D} \tag{D.3}$$

for proton segment C, or

$$D_j = -\frac{\gamma \sin(\phi - \phi_j)}{\sqrt{2}K_D} \tag{D.4}$$

for proton segment j, with $\phi_A, \phi_B, \phi_C, \phi_D = 225°, 135°, 45°$, and $315°$. These coordinates are those used throughout to describe the apparatus. $\phi = 0$ corresponds to due west along a line from the center of the detector bisecting E4 (see figure 3.12). When the four segments' results are averaged the false D values cancel each other. In the test runs with tilted polarization, $\phi = \phi_D = 315°$, indicating values of zero for segments B and D.

In the description above the beam was taken to be narrow and centered on $x = 0, y = 0$. For a thick beam symmetric around the z-axis, γ must be replaced by γ', reflecting the average of the spin-beta correlation over the beam profile. However, the false D in opposing segments still cancel.

D.2 Beam Displacement

It is apparent above that the existence of a polarization tilt is not enough to give a false total D when the values for the four proton segments are combined. However, if there is also an asymmetry in the beam profile, the cancellation is jeopardized. Consider again the narrow beam and small beta detectors, now with $\phi = 135°$ and a beam displacement r that is perpendicular to the polarization (see figure D.2). If r is small compared to

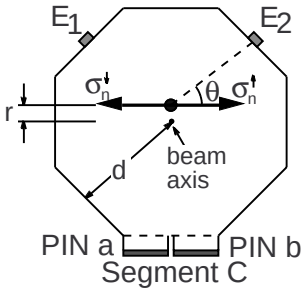

Figure D.2: If the beam is displaced the effect of a polarization tilt will differ in opposing proton segments.

the beam-detector distance d (a valid assumption for this experiment), $\cos\theta_{\sigma_n E_i}$ is now $\pm(1 + r/2d)/\sqrt{2}$ and we will find

$$D_C = \frac{-\gamma}{\sqrt{2}K_D}\left(1 + \frac{r}{2d}\right) \tag{D.5}$$

For proton segment A of the opposite side of the beam, $\cos\theta_{\sigma_n E_i} = \pm(1 - r/2d)/\sqrt{2}$ and $D_A = \gamma/\sqrt{2}K_D(1 - r/2d)$. The results for the opposing segments do not cancel, their average value being

$$\frac{1}{2}(D_A + D_C) = \frac{-\gamma}{2\sqrt{2}K_D}\left[(1 + r/2d) - (1 - r/2d)\right] = \frac{-\gamma}{4\sqrt{2}K_D}\frac{r}{d}. \tag{D.6}$$

This creates an offset in the final result.

Again, realistic beam width and beta detector area will modify the $\gamma/\sqrt{2}$ magnitude and the effect of r. With a general beam displacement $\mathbf{r}$, $-r/2d$ is replaced by $\mathbf{r}\cdot\mathbf{r}_1(\phi)/r_1^2$, where $\mathbf{r}_1(\phi)$ accounts for averaging the effect over the finite beam and detectors. The ϕ-dependence is indicative of the sensitivity of the effect to the relative orientation of $\mathbf{r}$ and $\mathbf{P}$. The effect is greatest when the beam displacement is perpendicular to the polarization.

With a polarization tilt of $\xi = 90^\circ$ (completely transverse polarization) and a beam asymmetry, the false result for D is given by

$$D(\xi = 90^\circ, \phi, \mathbf{r}) = \frac{1}{4}(D_A + D_B + D_C + D_D) \tag{D.7}$$

$$\frac{\gamma'}{4\sqrt{2}K_D}\left[\sin(\phi - 45^\circ)(1 + \frac{\mathbf{r}\cdot\mathbf{r}_1}{r_1^2}) - \cos(\phi - 45^\circ)(1 + \frac{\mathbf{r}\cdot\mathbf{r}_2}{r_2^2})\right.$$
$$\left. - \sin(\phi - 45^\circ)(1 - \frac{\mathbf{r}\cdot\mathbf{r}_1}{r_1^2}) + \cos(\phi - 45^\circ)(1 - \frac{\mathbf{r}\cdot\mathbf{r}_2}{r_2^2})\right]$$

$$= \frac{\gamma^{'}}{4\sqrt{2}K_D}\left[2\sin(\phi-45^\circ)\frac{\mathbf{r}\cdot\mathbf{r}_1}{r_1^2} - 2\cos(\phi-45^\circ)\frac{\mathbf{r}\cdot\mathbf{r}_2}{r_2^2}\right] \tag{D.8}$$

If the polarization is not tilted to be completely transverse to the beam, all the D values are scaled by $\sin\xi$, as if the polarization were a superposition of a fraction $\cos\xi$ of neutrons along $\hat{z}$ and a fraction $\sin\xi$ oriented transversely. This is easily seen in the small beta detector model since the average direction of the electron momentum is perpendicular to $\hat{z}$. Therefore, $\cos\theta_{\sigma_n E_i} = \hat{\sigma}_n \cdot \hat{p_e} = \sin\xi\hat{\sigma}_{n,t}\cdot\hat{p_e}$, where $\hat{\sigma}_{n,t}$ is the unit vector of the component of the spin in the transverse direction and depends on ϕ. Thus, the total false D-coefficient due to transverse polarization with a beam displacement is

$$D(\xi,\phi,\mathbf{r}) = \frac{\sin\xi\gamma^{'}}{4\sqrt{2}K_D}\left(2\sin(\phi-45^\circ)\frac{\mathbf{r}\cdot\mathbf{r}_1}{r_1^2} - 2\cos(\phi-45^\circ)\frac{\mathbf{r}\cdot\mathbf{r}_2}{r_2^2}\right). \tag{D.9}$$

This functional form was verified using Monte Carlo. Holding ϕ and $\mathbf{r}$ constant, D_{total} and the D_i were seen to have the predicted $\sin\xi$ dependence. At differing values of ξ and ϕ, $(D_A - D_C)/(D_D - D_B) = \tan(\phi - 45^\circ)$ was observed. Figure D.3 shows a comparison of data from the ATP runs with the results of a Monte Carlo simulation with the beam geometry and polarization parameters from that run.

D.3 Estimation of ATP Error

The data show a definite effect due to a polarization tilt. Applying the formalism derived above to the data indicates the size of the final offset. The first step is to determine the direction ϕ of the polarization tilt in the data by calculating $\tan(\phi - 45^\circ) = (D_A - D_C)/(D_D - D_B)$. Combining the small- and large-angle results,

$$\phi = 19^\circ \pm 21^\circ. \tag{D.10}$$

The tilt angle for the data can by found by comparing the data with the ATP runs, which had the large, known tilt.

$$\frac{\sin\xi_{data}}{\sin 90^\circ} = \frac{(D_A - D_C)_{ATP}\sin(\phi_{ATP} - 45^\circ)}{(D_A - D_C)_{ATP}\sin(\phi_{data} - 45^\circ)} \tag{D.11}$$

Combining the large- and small-angle data, this ratio is found to be 0.01, implying $\xi = 10$ mrad, or 0.57 degrees.

The magnitude $\gamma^{'}/\sqrt{2}K_D$ is measured to the best precision with the ATP data.

$$\frac{\gamma^{'}}{\sqrt{2}K_D} = \frac{D_C - D_A}{2} = 1.26 \pm 0.03, 1.03 \pm 0.02 \tag{D.12}$$

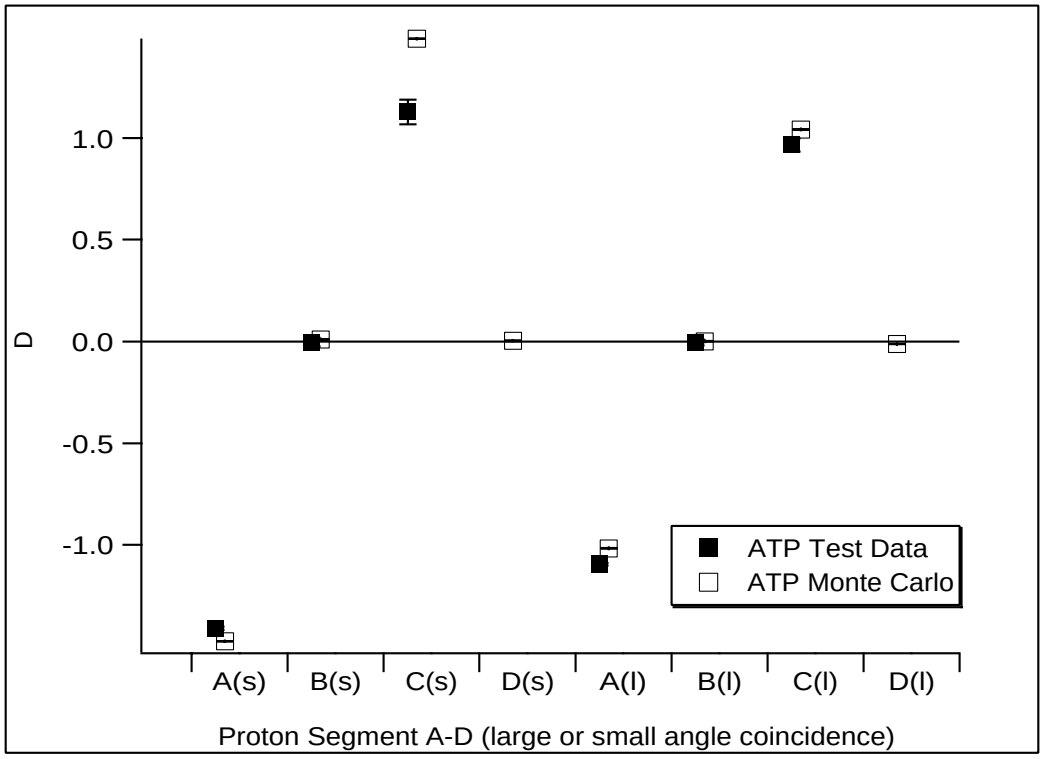

Figure D.3: During the ATP test runs with a 90° polarization tilt, the false D in each proton segment are clearly visible. Proton segment D was not operational.) Also shown are the Monte Carlo predictions for these values. The final combined D for the data in the ATP runs is $-7.0 \pm 1.2 \times 10^{-2}$

for small- and large-angles, respectively. This gives

$$\gamma^{'} = 0.55 \pm 0.02, 0.61 \pm 0.02. \tag{D.13}$$

The size of the displacement effect for these runs can also be calculated.

$$\frac{\mathbf{r}\cdot\mathbf{r}_1}{r_1^2} = \frac{(D_A + D_C)}{D_A - D_C} = 0.11 \pm 0.03, 0.06 \pm 0.02 \tag{D.14}$$

The effect of the beam displacement in the real data cannot be measured as precisely as the other quantities. A calculation like the one above gives

$$\frac{\mathbf{r}\cdot\mathbf{r}_1}{r_1^2} = \frac{(D_A + D_C)}{D_A - D_C} = -0.22 \pm 0.75, -0.17 \pm 0.40 \tag{D.15}$$

$$\frac{\mathbf{r}\cdot\mathbf{r}_2}{r_2^2} = \frac{(D_D + D_B)}{D_D - D_B} = 0.03 \pm 0.61, 0.16 \pm 0.19. \tag{D.16}$$

These measurements are not very useful for limiting the size of the systematic effect because the statistics are so poor. However, the estimation of these quantities can be approached instead by comparing beam conditions in the two run configurations. Beam scans in both runs show displacements in x and y of always less than 1 mm. The systematic effect depends more strongly on beam asymmetries perpendicular to the polarization tilt direction, and comparison of the measurements shows a perpendicular component 1.3 times larger in the ATP run. The data run has no measured beam displacement component parallel to the polarization. Since these measurements were not made all along the beam in the decay region but only at the upstream end, it is dangerous to use this information to estimate the systematic offset. A conservative estimate of the beam asymmetry effect in the data assumes it could be as large as that in the ATP runs. If we call this fractional effect f_r (as measured in equation D.14) and substitute it for both $\mathbf{r}\cdot\mathbf{r}_1/r_1^2$ and $\mathbf{r}\cdot\mathbf{r}_2/r_2^2$, the total false D in the data is given by

$$\begin{aligned} |D_{offset,total}| \leq \frac{\sin\xi\gamma^{'}}{4K_D}[&\sin(\phi - 45^\circ)(1+f_r) - \cos(\phi - 45^\circ)(1+f_r) \\ &- \sin(\phi - 45^\circ)(1-f_r) + \cos(\phi - 45^\circ)(1-f_r)] \\ = (\frac{\sin\xi}{2})(\frac{\gamma^{'}}{\sqrt{2}K_D})(f_r)&|\sin(\phi - 45^\circ) + \cos(\phi - 45^\circ)| \end{aligned} \tag{D.17}$$

$$D_{ATP} \leq (\frac{0.01}{2})\frac{1}{2}[(1.26)(0.11) + (1.03)(0.06)]|-0.4 - 0.90| \leq 6.7 \times 10^{-4} \tag{D.18}$$

In the above estimation of the error, it is assumed that the polarization tilt does not vary in this data set. This is the same question as that described earlier concerning the

question of the stability of the D_i over time. The stability of the D_i over time indicates that the polarization tilt is also stable throughout the data set.

The larger-than-expected magnitude of $\sin\xi$ calculated for the data is not perfectly understood. When a field measurement was done in December 1996, the field tilt was seen to point slightly down and eastward, varying from 0.5 mrad at the center of the detector and rising to 3 mrad at $z = \pm 40$ cm. However, these measurements were done without the detector in place, and it is possible that when the detector was in place, the detector frame sagged somewhat, allowing greater effective field tilt and beam displacement. After lowering the detector chamber onto the frame, the chamber was bolted on the downstream end to a gate valve, which was connected to the downstream vacuum chamber, supported on a separate frame. On the upstream end, the chamber was connected to the second-to-last collimator with a flexible bellows. This asymmetry in hardness of connection, as well as uneven weight, may have caused the sagging to have an associated tilt. An sag of several millimeters more on the upstream end would have caused an effective tilt of the magnitude and direction indicated by the data. Regardless, the ability to use the data to estimate systematics is not limited by the beam and field measurements.

Bibliography

[1] T. D. Lee and C. N. Yang. *Physical Review* 104, 1956, 254-8

[2] C. S. Wu, E. Ambler, R. W. Hayward, D. D. Hoppes, and R. P. Hudson. *Physical Review* 105, 1957, 1413-15

[3] G. Luders. *Annals of Physics* 2, 1957, 1-15

[4] J. H. Christenson, J. W. Cronin, V. L. Fitch, and R. Turlay. *Physical Review Letters* 13(4), 1964,138-40

[5] M. Kobayashi and T. Maskawa. *Progress in Theoretical Physics* 49(2),1973, 652-7

[6] P. Gu et al. *Physical Review Letters* 76(23), 1996, 4312-15

[7] J. K. Elwood, M. V. Wise, and M. J. Savage. *Physical Review D* 52(9), 1995, 5095-105

[8] R. Adler et al. *Nuclear Physics B*, Proceedings Supplements 59, 1997, 182-91

[9] H. L. Harney, A. Hupper, and A. Richter. *Nuclear Physics A* 518(1-2), 1990, 35-57

[10] C. G. Callan, Jr., R. F. Dashen, and D. J. Gross. *Physics Letters B* 63(3), 1976, 334-40

[11] I. S. Altarev et al. *Physics Letters B* 276(1-2), 1992, 242-6

[12] K. F. Smith, et al. *Physics Letters B* 234(1-2) 1990, 191-6

[13] J. D. Jackson, S. B. Treiman and H. W.Wyld. *Physical Review* 106(1), 1957, 514-21

[14] E. Christova, and M. Fabbrichesi. *Physics Letters B* 315(1-2), 1993, 113-18

[15] G. Barenboim, J. Bernabeu, J. Prades, and M. Raidal. *Physical Review D* 55(7), 1997, 4213-21

[16] A. S. Joshipura. *Physical Review D* 43(1), 1991, R25-28

[17] K. Akama, K. Katsuura,and H. Terazawa. *Physical Review D* 56(), 1997, R2490-4

[18] L. Ryder. *Contemporary Physics* 35(3), 1994, 151-63

[19] A. D.Sakharov. *JETP Letters* 6, 1967, 24

[20] B. R. Holstein. **Weak Interactions in Nuclei**, Princeton University Press, New Jersey, 1989

[21] D. H. Wilkinson. *Nuclear Physics A* 377, 1982, 474

[22] R. M. Barnett et al. *Physical Review D* 54(1),1996 and 1997 off-year partial update for the 1998 edition available on the Particle Data Group WWW pages (URL: http://pdg.lbl.gov/).

[23] J. Reich, presented at WEIN symposium, Santa Fe, NM, June 1998

[24] A. L. Hallin, F. B. Calaprice, D. W. MacArthur, L. E. Piilonen, M. B. Schneider, and D. F. Schreiber. *Physical Review Letters* 52(5), 1984, 337-40

[25] H. Wenninger, J. Stiewe, and H. Luetz. *Nuclear Physics* A109, 1968, 561

[26] A. S. Carnoy, J. Deutsch, and P. Quin. *Nuclear Physics A* 568(2), 1994, 265-70

[27] F. Glück, I. Joó, J. Last. *Nuclear Physics A* 593, 1995, 125-150

[28] J. D. Jackson, S. B. Treiman, and H. W. Wyld, Jr. *Nuclear Physics* 4, 1957, 206

[29] C. G. Callan and S. B. Treiman. *Physical Review*162(5), 1967, 1494-7

[30] R. I. Steinberg, P. Liaud, B. Vignon, and V. W. Hughes. *Physical Review Letters* 33(1), 1974, 41-4

[31] B. G. Erozolimskii, Yu. A. Mostovoi, V. P. Fedunin, A. L. Frank, and O. V. Khakhan. *Soviet Journal of Nuclear Physics* 28(1), 1978, 98-104

[32] A. V. Vorobiov, B. G. Erozolimskii, I. A. Kuznetzov, and Yu. A.Mostovoii. *Nuclear Instruments and Methods in Physics Research A* 284, 1989, 127-9

[33] F. P. Calaprice, E. G. Commins, H. M. Gibbs, G. L. Wick, and Dobson. *Physical Review* 184(4), 1969, 1117-29

[34] J. Sromicki et al. *Physical Review C* 53(2), 1996, 932-955

[35] J. Mortara. Ph.D. thesis, 1998

[36] P. Herczeg, and I. B. Khriplovich *Physical Review D* 56(1), 1997, 80-89

[37] P. Herczeg, in **Symmetries and Fundamental Interactions in Nuclei**, W. Haxton and E. Henley, eds, World Scientific, 1995, 89

[38] J. P. Jacobs, W. M. Klipstein, S. K. Lamoreaux, B. R. Heckel, and E. N. Fortson. *Physical Review A*

[39] P. Herczeg, to appear in *Proceedings of the Sixth International Symposium of Particles, Strings, and Cosmology* (PASCOS-98)

[40] E. G. Wasserman. Ph.D. thesis, 1994

[41] H. J. Prask, J. M. Rowe, J. J. Rush, and I. G. Schroder. *Journal of Research of the National Institute of Standards and Technology* 98(1), 1993, 1-13

[42] J. Byrne. **Neutrons, Nuclei, and Matter**, Institute of Physics Publishing, Bristol, 1994

[43] O. Schaerpf. *Physica B* 156-157, 1989, 631-46

[44] B. K. Fujikawa. Collaboration report, Oct 10, 1994

[45] S. F. Mughabghab, R. R. Kinsey, and C. L. Dunford. *Neutron Cross Sections, Volume I, Neutron Resonance Parameters and Thermal Beam Cross Sections*, Academic Press, 1981

[46] Bicron Corporation, Newbury, OH

[47] K. Ackerstaff, et al. (EDDA Collaboration) *Nuclear Instruments and Methods in Physics Research A*, 335, 1993, 113-120, and references therein.

[48] General Purpose Interface Bus defined by IEEE Standards 488-1978, 488.1-1987, and 488.2-1987

[49] Introductions to NIM, CAMAC, and VME and specifications for LRS modules can be found in the *LeCroy 1997 Research Instrumentation Products Catalogue*, LRS, Chestnut Ridge, NY, http://www.lecroy.com

[50] A. García. Collaboration report, Jan 16, 1995

[51] F. W. Wietfeldt. Collaboration report, May 5, 1995